

---

# Stable Broadband Finite Element Parasitic Extraction and Sensitivity Analysis

---

Zur Erlangung des akademischen Grades Doktor-Ingenieur (Dr.-Ing.)  
Genehmigte Dissertation von Jonathan Stysch aus Filderstadt  
Tag der Einreichung: 01.02.2022, Tag der Prüfung: 13.05.2022

1. Gutachten: Prof. Dr.-Ing. Herbert De Gersem
2. Gutachten: Prof. Dr. rer. nat. Markus Clemens  
Darmstadt, Technische Universität Darmstadt



TECHNISCHE  
UNIVERSITÄT  
DARMSTADT

Electrical Engineering  
and Information  
Technology Department  
Institute for Accelerator  
Science and  
Electromagnetic Fields

# Stable Broadband Finite Element Parasitic Extraction and Sensitivity Analysis

Accepted doctoral thesis by Jonathan Stysch

Date of submission: 01.02.2022

Date of thesis defense: 13.05.2022

Darmstadt, Technische Universität Darmstadt

Bitte zitieren Sie dieses Dokument als:

URN: urn:nbn:de:tuda-tuprints-215616

URL: <http://tuprints.ulb.tu-darmstadt.de/21561>

Jahr der Veröffentlichung auf TUPrints: 2022

Dieses Dokument wird bereitgestellt von tuprints,  
E-Publishing-Service der TU Darmstadt

<http://tuprints.ulb.tu-darmstadt.de>

[tuprints@ulb.tu-darmstadt.de](mailto:tuprints@ulb.tu-darmstadt.de)

Die Veröffentlichung steht unter folgender Creative Commons Lizenz:

Namensnennung 4.0 International

<https://creativecommons.org/licenses/by/4.0/>

This work is licensed under a Creative Commons License:

Attribution 4.0 International

<https://creativecommons.org/licenses/by/4.0/>

---

## Erklärungen laut Promotionsordnung

### § 8 Abs. 1 lit. c PromO

Ich versichere hiermit, dass die elektronische Version meiner Dissertation mit der schriftlichen Version übereinstimmt.

### § 8 Abs. 1 lit. d PromO

Ich versichere hiermit, dass zu einem vorherigen Zeitpunkt noch keine Promotion versucht wurde. In diesem Fall sind nähere Angaben über Zeitpunkt, Hochschule, Dissertationsthema und Ergebnis dieses Versuchs mitzuteilen.

### § 9 Abs. 1 PromO

Ich versichere hiermit, dass die vorliegende Dissertation selbstständig und nur unter Verwendung der angegebenen Quellen verfasst wurde.

### § 9 Abs. 2 PromO

Die Arbeit hat bisher noch nicht zu Prüfungszwecken gedient.

Darmstadt, 01.02.2022

---

J. Stysch



---

## Abstract

---

Parasitic extraction is a powerful tool in the design process of electronic components, specifically as part of workflows that check electromagnetic compatibility. It enables to capture parasitic effects in field simulation and to embed them as lumped parameters in subsequent circuit simulations together with the functional elements of the design. This thesis develops a broadband parasitic extraction method capable of the automatic treatment of multi-port models of arbitrary conductor geometry without requiring any significant manual user interaction. It applies the finite element method to the differential form of Maxwell's equations, which makes it more flexible than established integral equation approaches with respect to spatial discretization and the handling of inhomogeneous material parameters. The method is capable of both the extraction of the impedance matrix using a full-wave system as a universal description of a model's parasitics, and the extraction of individual resistances, inductances and capacitances with quasistatic approximations. The inherent low-frequency instability of finite element solutions of Maxwell's equations is successfully alleviated by applying a state-of-the-art discretization scheme, that is based on a decomposition of the Sobolev space of curl-conforming functions. Beyond the mere assessment of a design, sensitivity analysis provides the basis for shape optimization. The stable parasitic extraction is used to improve an existing sensitivity analysis method with respect to efficiency, robustness and applicability. Furthermore, a low-frequency stable approach to include the extracted frequency-dependent parasitics in transient circuit simulations utilizing the vector fitting method is investigated. The parasitic extraction method is verified with both analytical results, and measurement results of a common-mode choke.



---

## Zusammenfassung

---

Parasitär-Extraktion ist ein leistungsstarkes Werkzeug im Entwicklungsprozess elektrischer Komponenten, insbesondere als Teil von Arbeitsabläufen, die die elektromagnetische Verträglichkeit überprüfen. Durch sie können parasitäre Effekte in elektromagnetischen Simulationen erfasst werden, um diese dann in Netzwerksimulationen mit den funktionalen Netzwerkelementen einzubinden. Diese Dissertation entwickelt eine Breitband-Parasitär-Extraktionsmethode, die in der Lage ist, Mehr-Tor-Modelle mit beliebige Leitergeometrien ohne größere Nutzer-Interaktion automatisch zu behandeln. Sie wendet die Finite-Elemente-Methode auf die differentielle Form der Maxwellgleichungen an, wodurch sie im Hinblick auf die räumliche Diskretisierung und die Behandlung inhomogener Materialparameter flexibler ist als etablierte Integralgleichungsmethoden. Die Methode ist fähig sowohl die Impedanzmatrix mit einem ungenäherten System als eine universale Beschreibung der parasitären Effekte, als auch individuelle Widerstände, Induktivitäten und Kapazitäten mit quasistatischen Systemen zu extrahieren. Die inhärente Niederfrequenzinstabilität von Finite-Elemente-Lösungen der Maxwellgleichungen wird erfolgreich beseitigt durch die Anwendung eines modernen Diskretisierungsansatzes, der auf einer Zerlegung des Sobolev-Raums rotationskonformer Funktionen basiert. Über die bloße Beurteilung eines Komponentenentwurfs hinaus schaffen Sensitivitätsanalysen die Grundlage für Formoptimierungen. Die stabile Parasitär-Extraktionsmethode wird daher benutzt, um einen existierenden Sensitivitätsanalyse-Ansatz mit Hinblick auf Effizienz, Robustheit und Anwendbarkeit zu verbessern. Des Weiteren wird ein niederfrequenzstabiler Ansatz die extrahierten frequenzabhängigen parasitären Elemente in transienten Netzwerksimulationen zu berücksichtigen diskutiert, der die Vektor-Fitting-Methode verwendet. Die Parasitär-Extraktionsmethode wird sowohl mit analytischen Ergebnissen verifiziert, als auch mit den Messergebnissen einer Gleichakttdrossel.



---

# Contents

---

<b>1. Introduction</b>	<b>1</b>
1.1. Motivation . . . . .	1
1.2. Overview . . . . .	2
1.3. Outline . . . . .	4
<b>2. Maxwell's Equations</b>	<b>7</b>
2.1. Time Domain . . . . .	7
2.2. Frequency Domain . . . . .	9
2.3. Interface and Boundary Conditions . . . . .	10
2.4. Potential Formulation . . . . .	12
2.5. Static and Quasistatic Approximations . . . . .	14
<b>3. Finite Element Method</b>	<b>17</b>
3.1. Basic Concepts . . . . .	17
3.2. Conforming Finite Elements . . . . .	19
3.2.1. $H^1$ -conforming elements . . . . .	20
3.2.2. $H(\text{curl})$ -conforming elements . . . . .	20
3.2.3. De Rham complex . . . . .	22
<b>4. Electrical Networks</b>	<b>25</b>
4.1. Basic Passive Network Elements . . . . .	25
4.1.1. Resistance computation . . . . .	27
4.1.2. Inductance computation . . . . .	28
4.1.3. Capacitance computation . . . . .	32
4.1.4. Impedance computation . . . . .	34
4.2. Graph Theory . . . . .	36
4.2.1. Basic concepts . . . . .	36
4.2.2. Electrical networks as graphs . . . . .	38
<b>5. Finite Element Parasitic Extraction Method</b>	<b>41</b>
5.1. General Method . . . . .	41
5.1.1. Device model, boundary conditions, and extraction topology . . . . .	41
5.1.2. Formulation of the fundamental differential equations . . . . .	43

5.1.3.	Modeling the connecting source current density . . . . .	45
5.1.4.	Compensating the inductive influence of the source current density . . . . .	46
5.2.	Quasistatic Approximations . . . . .	49
5.2.1.	Magnetoquasistatic approximation . . . . .	50
5.2.2.	Darwin approximation . . . . .	50
5.3.	Perfect Electric Conductor Case . . . . .	51
5.3.1.	Magnetostatic computation of the external inductance . . . . .	52
5.3.2.	Darwin approximation in the PEC case . . . . .	53
5.4.	Numerical Results . . . . .	54
5.4.1.	Verification with analytical results . . . . .	54
5.4.2.	Loop model at high frequencies . . . . .	60
<b>6.</b>	<b>Low-Frequency Stable Finite Element Discretization</b>	<b>63</b>
6.1.	Introduction . . . . .	63
6.2.	Stabilization of the Electric Field Formulation . . . . .	65
6.2.1.	Stabilizing the System Matrix . . . . .	67
6.2.2.	Stabilizing the Right-Hand Side . . . . .	69
6.3.	Stable Computation of the Compensated Scalar Potential . . . . .	72
6.3.1.	Stabilizing the Right-Hand Side . . . . .	73
6.3.2.	Stabilizing the Lorenz-gauged system matrix for magnetic boundaries	73
6.4.	Quasistatic Approximations . . . . .	75
6.4.1.	MQS system . . . . .	75
6.4.2.	Darwin system . . . . .	76
6.5.	Perfect Electric Conductor Case . . . . .	77
6.6.	Constructing the Finite-Dimensional Sobolev Spaces . . . . .	79
6.6.1.	Tree-cotree splitting . . . . .	79
6.6.2.	Gradient-space splitting . . . . .	80
6.7.	Numerical Results . . . . .	81
<b>7.</b>	<b>Frequency-Dependent Parasitics for Transient Network Simulations</b>	<b>87</b>
7.1.	Vector Fitting and Equivalent Circuit Creation . . . . .	88
7.2.	Stable Impedance-Based Equivalent Circuit Creation . . . . .	90
7.3.	Numerical Results . . . . .	92
<b>8.</b>	<b>Sensitivity Analysis</b>	<b>97</b>
8.1.	Introduction . . . . .	97
8.2.	Finite Element Discretization . . . . .	98
8.2.1.	Magnetostatic and magnetoquasistatic systems . . . . .	98
8.2.2.	Electrostatic system and capacitive sensitivities . . . . .	100
8.3.	Computation of Resistive and Inductive Sensitivities . . . . .	101
8.3.1.	Adjoint sensitivity computation . . . . .	101



8.3.2. Magnetoquasistatic sensitivity computation . . . . .	102
8.3.3. Magnetostatic computation of inductive sensitivities . . . . .	104
8.4. Numerical Results . . . . .	105
8.4.1. Choke with magnetic core . . . . .	105
8.4.2. Performance comparison . . . . .	107
<b>9. Industrial Application: Common Mode Choke</b>	<b>111</b>
9.1. Verification with Measurement Results . . . . .	111
9.2. Vector Fitting Results . . . . .	115
<b>10. Conclusions</b>	<b>119</b>
10.1. Summary . . . . .	119
10.2. Outlook . . . . .	120
<b>A. Appendix</b>	<b>123</b>
A.1. Asymptotic and Absorbing Boundary Conditions . . . . .	123
A.1.1. Asymptotic boundary conditions . . . . .	124
A.1.2. Absorbing boundary conditions . . . . .	125
A.2. Computation of Non-Static Capacitances . . . . .	127
<b>Bibliography</b>	<b>131</b>
<b>List of Acronyms and Abbreviations</b>	<b>139</b>
<b>Acknowledgments</b>	<b>141</b>
<b>Curriculum Vitae</b>	<b>143</b>



---

# 1. Introduction

---

## 1.1. Motivation

In recent decades, the demand for electronic devices has strongly increased. This trend is not restricted to a higher demand for consumer electronics. Also automotive machines, that are primarily mechanic, require an increasing number of electronic systems, ranging from sensors to infotainment systems to power electronics of electric drives. This higher demand requires shorter development cycles, thereby limiting the time engineers can spend on the development of a single device. In addition, there is an associated demand for ever smaller device dimensions, higher levels of integration, and increased clock speeds. This trend complicates the device development, especially with regards to electromagnetic compatibility (EMC).

The use of numerical simulation techniques is crucial for mastering these engineering challenges. Simulations facilitate the detection of design flaws during the early stages of the design process, before prototyping. Moreover, some quantities of interest that are difficult or impossible to measure for highly integrated devices are accessible in simulation. Beyond the mere assessment of a design, topology and shape optimization methods can be used to find optimized designs that lead to a better performance or reduced cost of the device.

The design process of an electrical component typically yields an electrical network of its functional elements, as well as a CAD model of the design that includes the interconnect between the functional elements. The influence of the interconnect on the device's functionality can be considered in network simulations through *parasitic extraction*. This is the process of assigning passive network elements like resistances, inductances and capacitances to the structures of the CAD model by using simulations of Maxwell's equations. The process is called parasitic extraction since the network elements extracted from the CAD model usually (although not always) have a detrimental effect of the device's performance and are hence labeled *parasitic*.

Fig. 1.1 illustrates such a simulation workflow. After the parasitic extraction, a joint network simulation of both functional and parasitic elements is used to assess the design, e.g., by checking whether specific EMC requirements are met. If the assessment uncovers issues that require treatment, optimization methods based on a sensitivity analysis of relevant quantities of interest (QoIs) can facilitate a re-design.

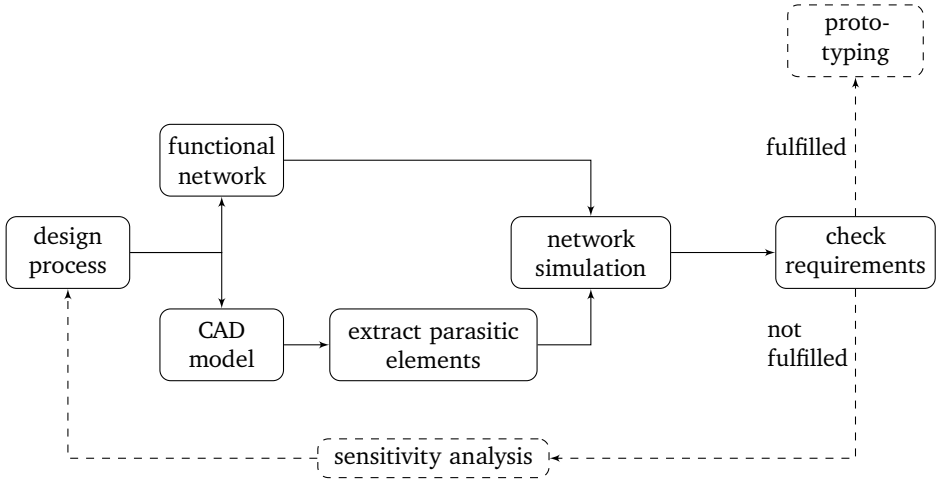


Figure 1.1.: Simulation workflow supporting the design process of an electrical component.

## 1.2. Overview

An early and influential parasitic extraction approach is Ruehli’s partial element equivalent circuit (PEEC) method [Rue74]. It uses a combined boundary and volume element discretization scheme to express the model’s electromagnetic properties as an equivalent circuit. The extracted parasitic network elements, however, are not associated with individual structures of the model but only with the boundary and volume elements used in its discretization. The equivalent circuit thus contains a very large number of elements. This can not only critically impact the computation time of subsequent transient circuit simulations; it also significantly hinders the root-cause analysis of observed issues due to the large number of parameters in the equivalent circuit.

Two important methods, that can to some extent be considered derivatives of PEEC, enable the extraction of single parasitic elements directly associated with entire structures of a model: The capacitance extraction method FastCap [nabors\_fastcap:\_1991] using boundary elements, and the inductance and resistance extraction method FastHenry [kamon\_fasthenry:\_1994] using volume elements. The former method utilizes the electrostatic (ES) approximation and the latter one the magnetoquasistatic (MQS) approximation. This separation of electric and magnetic effects is only fully valid at low frequencies. In [Kam+98] a derived approach is developed that considers some of the interactions between electric and magnetic effects by using Darwin’s approximation.

---

The aforementioned methods are all based on Maxwell's equations in integral form and use Green's functions in the solution process. This severely complicates the treatment of materials with spatially inhomogeneous electric permittivities or magnetic permeabilities. In their standard form, both PEEC and FastHenry require cuboid volume elements, which can be impractical in representing the complex geometries encountered in industrial applications. Generalizing these methods with less restrictive volume elements can be cumbersome [Rue+03].

These disadvantages are avoided by approaches based on the finite element method (FEM), which allows for a highly flexible spatial discretization by using unstructured meshes, and an inherent treatment of inhomogeneous material parameters. In [CF89] the FEM is utilized in a parasitic extraction method for two-dimensional problems (wires obeying a translational symmetry), that uses both MQS and ES equations. A method for three-dimensional problems is provided in [SS01; HSS03], where the FEM is applied to static approximations of Maxwell's equations to extract parasitic resistances, capacitances and inductances.

In a series of publications [Tra+12; Tra+13a; Tra+13b; Tra14; HP15] Traub et al. develop a finite element (FE) inductance and capacitance extraction method intended primarily for EMC applications. Similar to [Kam+98] it uses Darwin's approximation to capture some of the resonant behavior that is observed at higher frequencies where magnetic and electric effects are no longer decoupled. Ohmic losses are neglected by Traub et al. as they are of only minor importance in EMC problems. The authors consider two different extraction approaches:

1. Computing the impedance directly for a given current excitation. This approach is predominately used for inductance extraction [Tra+12; Tra+13a]. A special source current density and a related compensation term allow the authors to remove the unwanted inductive influence of the current source on the results, thereby enabling an accurate computation of partial inductances of individual conductor segments.
2. Computing the eigenmodes of the system in order to determine the parasitic lumped elements by matching the resonant behavior of 3D simulation and equivalent circuit [Tra+13b; Tra14; HP15]. This approach is mainly used to compute equivalent capacitances that are inaccessible in ES simulations. However, its relatively indirect way of determining parasitic elements fails to produce accurate equivalent circuits reliably (cf. Section A.2).

The direct inductance computation approach of Traub et al. provides, together with static resistance and capacitance extraction techniques, the basis for a sensitivity analysis method developed by Schuhmacher et al. in [Sch+18a; Sch+18b; Sch18]. The method computes the sensitivities of a QoI to changes of the design's geometry by using the parasitic elements to express the QoI. In [Ben+19] Schuhmacher et al.'s sensitivity analysis is applied in the

---

optimization of a pressure sensor, attesting to the merit of both this method and Traub et al.'s underlying parasitic extraction.

In spite of the demonstrable usefulness of these parasitic extraction and sensitivity analysis methods, they are still plagued by a number of issues:

1. They lack a rigorous theoretical treatment, and do not correctly consider inhomogeneous material parameters.
2. They do not consider losses of any kind, except in a separate static ohmic resistance extraction. The deficit includes losses occurring in the magnetic materials of chokes.
3. The used inductance extraction method requires the impedance to be computed at several frequency points using Darwin's approximation, recovering the inductance in a subsequent least-squares fit. In addition to being unnecessarily complicated and inefficient, the approach also lacks robustness due to the instability that FE solutions of Darwin's approximation exhibit at low frequencies.

The first objective of this thesis is to resolve these issues, thereby creating efficient and robust quasistatic parasitic extraction and sensitivity analysis methods. To this end, a rigorous theoretical treatment is developed for the used impedance computation method. A coherent derivation of the special current excitation, including its crucial inductive compensation term, facilitates the correct consideration of inhomogeneous materials. An efficient MQS-based inductance computation method that can include ohmic and other losses enables the frequency-dependent extraction of parasitic inductances and resistances and associated sensitivity analysis. This extends the applicability of the methods also to some problems in the design of power electronics.

The second objective is to develop a general parasitic extraction method that is not limited to the quasistatic regime. This is realized with an impedance computation method that uses Maxwell's equations without approximation. A central difficulty is the low-frequency (LF) instability inherent to FE solutions of Maxwell's equations. The issue is resolved by adapting the elegant LF-stable discretization scheme of Eller et al. [Ell+17] to the impedance computation method.

### 1.3. Outline

The thesis is outlined as follows. Chapter 2 establishes a theoretical foundation by reviewing Maxwell's equations. The transition from time to frequency domain, interface and boundary conditions, and the  $A\text{-}\phi$  potential formulation are discussed. A summary of static and quasistatic approximations relevant in the course of the work concludes the chapter.

The FEM is reviewed in Chapter 3. In focus are the different continuity properties of  $H^1$ -conforming and  $H(\text{curl})$ -conforming elements, as well as the relationship between the

---

Sobolev spaces of these elements in the De Rham complex. This provides a foundation for the LF stable FE discretization of Chapter 6.

The first section of Chapter 4 examines the connection of electromagnetic field theory and electrical networks. Computation methods for passive network parameters are developed. This includes the capacitance computation of [Sty+22] and a generalization of the impedance computation of [SKD22a], which forms the basis for the general parasitic extraction method of Chapter 5. The second section of Chapter 4 discusses graph theory and its application to electrical networks, focusing on the relationship between descriptions with branch variables and nodal variables.

Chapter 5 derives the general parasitic extraction method central to this thesis. It expands on [SKD22a], most notably by also considering absorbing and asymptotic boundary conditions. Full-wave and Darwin approximation systems are derived, that are suitable to capture the full parasitic response in a nodal impedance matrix. An MQS approach enables a direct resistance and inductance extraction. The special case of perfect electric conductors (PECs) is considered as a useful simplification, the most important consequence of which is an efficient frequency-independent computation method for the external inductance matrix. First numerical results are compared to analytical and numerical reference values to verify the method.

The LF-stable FE discretization of the parasitic extraction method is developed in Chapter 6, which is an expansion of the work presented in [SKD22c]. The computation of the electric field is stabilized using Eller et al.'s approach [Ell+17]. The approach is generalized for absorbing and asymptotic boundary conditions. In addition to the full-wave system, it is also applied to the quasistatic systems and to the PEC case. Numerical results demonstrate the unrestricted stability of the discretization scheme.

Chapter 7 shows how frequency-dependent parasitics can be included in transient network simulations via the vector fitting method [GS99], specifically by using the synthesis of equivalent circuits of the nodal admittance matrix described in [Gus02]. Stability issues that occur at low frequencies if the original data is in the form of a nodal impedance matrix are demonstrated. An LF stable alternative approach, also presented in [SKD22c], is developed based on a combination of MQS and ES simulation results.

Chapter 8 improves upon the sensitivity analysis method of Schumacher et al. [Sch+18a] by using the direct resistance and inductance extraction methods of Chapter 5. The chapter is strongly based on [Sty+22]. In addition to providing an improved efficiency, robustness, and accuracy of the frequency-independent inductance computation method, a novel MQS-based approach allows to consider resistive and inductive sensitivities and their frequency dependence. Numerical results illustrate these advancements.

The industrial example of a common-mode choke with a strongly dispersive magnetic core is considered in Chapter 9. A comparison of measurement and simulation results provides an additional verification of the parasitic extraction method of Chapter 5. The LF stable equivalent circuit synthesis approach of Chapter 7 is applied to the extracted parasitics.

---

Some of the results presented in the chapter appear in [SKD22a; SKD22b]. Chapter 10 concludes the main part of the thesis with a summary and an outlook.

Finally, Appendix A discusses two supplementary topics: Section A.1 details how asymptotic and absorbing boundary conditions can be applied to the developed parasitic extraction method, expanding on the theoretical treatment provided in [Din21]. Section A.2 shows how the capacitance extraction method of [HP15] can be improved by abandoning its eigenmode-based approach.

---

## 2. Maxwell's Equations

---

### 2.1. Time Domain

Maxwell's equations [Max65] constitute, together with the Lorentz force law, the fundamental equations of classical electrodynamics. They are a set of partial differential equations (PDEs) that relate five vector fields  $\mathbb{R} \times \mathbb{R}^3 \rightarrow \mathbb{R}^3$  on time  $t \in \mathbb{R}$  and position  $\mathbf{r} \in \mathbb{R}^3$ , namely the electric field strength  $\mathcal{E}$ , magnetic flux density  $\mathcal{B}$ , electric flux density  $\mathcal{D}$ , magnetic field strength  $\mathcal{H}$ , and electric current density  $\mathcal{J}$ , and one scalar field, the electric charge density  $\varrho : \mathbb{R} \times \mathbb{R}^3 \rightarrow \mathbb{R}$ . They read in differential form [Jac99]

$$\operatorname{curl} \mathcal{H} = \frac{\partial \mathcal{D}}{\partial t} + \mathcal{J}, \quad (2.1a)$$

$$\operatorname{curl} \mathcal{E} = -\frac{\partial \mathcal{B}}{\partial t}, \quad (2.1b)$$

$$\operatorname{div} \mathcal{D} = \varrho, \quad (2.1c)$$

$$\operatorname{div} \mathcal{B} = 0. \quad (2.1d)$$

The individual equations (2.1a)-(2.1d) are called the Ampère-Maxwell law, Faraday's law, Gauss's law, and Gauss's law for magnetism, respectively. The continuity equation

$$\frac{\partial \varrho}{\partial t} + \operatorname{div} \mathcal{J} = 0 \quad (2.2)$$

is implicit in (2.1a) and (2.1c).

It is often instructive to consider Maxwell's equations in integral form, which is much closer to the equations actually given by Maxwell in [Max65] than the differential form (2.1). The integral forms of the Ampère-Maxwell law (2.1a) and Faraday's law (2.1b) can be derived by integrating over an open oriented surface  $\Sigma$  in  $\mathbb{R}^3$  with boundary  $\partial\Sigma$  and applying Stokes' theorem

$$\int_{\Sigma} \operatorname{curl} \mathbf{f} \cdot \hat{\mathbf{n}} \, dS = \oint_{\partial\Sigma} \mathbf{f} \cdot d\mathbf{l} \quad \text{for all smooth } \mathbf{f} : \mathbb{R}^3 \rightarrow \mathbb{C}^3 \quad (2.3)$$

to the left-hand sides of the equations. Here,  $\hat{\mathbf{n}}$  denotes the outer normal unit vector on  $\Sigma$  and  $d\mathbf{l}$  is the line element along  $\partial\Sigma$ . Integral forms of the remaining two Maxwell equations

can be found by integrating (2.1c) and (2.1d) over a region  $\Omega \subset \mathbb{R}^3$  with boundary  $\partial\Omega$  and applying the divergence theorem

$$\int_{\Omega} \operatorname{div} \mathbf{f} \, dV = \oint_{\partial\Omega} \mathbf{f} \cdot \hat{\mathbf{n}} \, dS \quad \text{for all smooth } \mathbf{f} : \mathbb{R}^3 \rightarrow \mathbb{C}^3 \quad (2.4)$$

to the left-hand sides. Thus, the integral-form Maxwell equations are

$$\oint_{\partial\Omega} \mathbf{H} \cdot d\mathbf{l} = \int_{\Sigma} \frac{\partial \mathbf{D}}{\partial t} \cdot \hat{\mathbf{n}} \, dS + \int_{\Sigma} \mathcal{J} \cdot \hat{\mathbf{n}} \, dS, \quad (2.5a)$$

$$\oint_{\partial\Omega} \mathbf{E} \cdot d\mathbf{l} = - \int_{\Sigma} \frac{\partial \mathbf{B}}{\partial t} \cdot \hat{\mathbf{n}} \, dS, \quad (2.5b)$$

$$\oint_{\partial\Omega} \mathbf{D} \cdot \hat{\mathbf{n}} \, dS = \int_{\Omega} \rho \, dV, \quad (2.5c)$$

$$\oint_{\partial\Omega} \mathbf{B} \cdot \hat{\mathbf{n}} \, dS = 0. \quad (2.5d)$$

The properties of electric and magnetic materials are considered in the magnetic field strength  $\mathbf{H}$  and electric flux density  $\mathbf{D}$ . In order to solve Maxwell's equations,  $\mathbf{H}$  and  $\mathbf{D}$  have to be expressed as a function of  $\mathbf{B}$  and  $\mathbf{E}$  through constitutive relations that can in general be non-linear and exhibit hysteresis (i.e., depend on past values of  $\mathbf{B}$  and  $\mathbf{E}$ ). In the context of the frequency domain methods discussed in this work, only linear constitutive relations of the following form are considered [Jac99]

$$\mathbf{B} = \mu_t * \mathbf{H}, \quad (2.6a)$$

$$\mathbf{D} = \varepsilon_t * \mathbf{E}. \quad (2.6b)$$

Here, the star operator denotes the convolution

$$(f * g)(t) = \int_{-\infty}^{\infty} f(\tau)g(t - \tau) \, d\tau, \quad (2.7)$$

and  $\mu_t$  and  $\varepsilon_t$  are the time-domain magnetic permeability and electric permittivity, respectively. In the presence of conducting materials, a form of Ohm's law must be provided that relates the source current density  $\mathcal{J}$  to  $\mathbf{E}$  (and in the most general case also  $\mathbf{B}$ ). In this work, the form

$$\mathcal{J} = \sigma_t * \mathbf{E} + \mathcal{J}_s \quad (2.8)$$

is chosen, with  $\sigma_t$  being the time-domain conductivity and  $\mathcal{J}_s$  denoting a source current density that does not couple to  $\mathbf{E}$  directly. In the general case also allowing for anisotropic materials, the material parameters  $\mu_t$ ,  $\varepsilon_t$ , and  $\sigma_t$  are second-order tensor fields. For isotropic materials a description with scalar fields suffices.

## 2.2. Frequency Domain

In the case of linear constitutive equations (2.6) and a linear Ohm's law (2.8) considered in this work, Maxwell's equations (2.1) are linear PDEs. This property allows their transformation to frequency domain using the Fourier transform

$$(\mathcal{F}(f))(\omega) = \int_{-\infty}^{\infty} f(t)e^{-j\omega t} dt, \quad (2.9)$$

with  $\mathcal{F}(f)$  being the Fourier transform of the function  $f$ ,  $j$  denoting the imaginary unit and  $\omega$  the angular frequency. If both  $f$  and its time derivative are integrable, the Fourier transform of the derivative is given by

$$\mathcal{F}\left(\frac{\partial f}{\partial t}\right) = j\omega\mathcal{F}(f), \quad (2.10)$$

i.e., in frequency domain, time differentiations correspond to simple multiplications with the factor  $j\omega$ . Thus, the frequency-domain Maxwell equations are PDEs only of the three spatial dimensions. They read

$$\text{curl } \mathbf{H} = j\omega\mathbf{D} + \mathbf{J}, \quad (2.11a)$$

$$\text{curl } \mathbf{E} = -j\omega\mathbf{B}, \quad (2.11b)$$

$$\text{div } \mathbf{D} = \rho, \quad (2.11c)$$

$$\text{div } \mathbf{B} = 0. \quad (2.11d)$$

with  $\mathbf{D}$ ,  $\mathbf{B}$ ,  $\mathbf{E}$ ,  $\mathbf{H}$ ,  $\mathbf{J}$ , and  $\rho$ , denoting the complex-valued Fourier transforms of the quantities of the time-domain Maxwell equations (2.1). Transforming the continuity equation to frequency domain gives

$$j\omega\rho + \text{div } \mathbf{J} = 0. \quad (2.12)$$

Moreover, the convolution (2.7) becomes a mere multiplication in frequency domain due to the convolution theorem

$$\mathcal{F}(f * g) = \mathcal{F}(f)\mathcal{F}(g). \quad (2.13)$$

The frequency-domain constitutive relations are therefore given by

$$\mathbf{B} = \mu\mathbf{H} \equiv \mu_0\mu_r\mathbf{H}, \quad (2.14a)$$

$$\mathbf{D} = \varepsilon\mathbf{E} \equiv \varepsilon_0\varepsilon_r\mathbf{E}. \quad (2.14b)$$

with the magnetic permeability  $\mu = \mathcal{F}(\mu_t)$  and electric permittivity  $\varepsilon = \mathcal{F}(\varepsilon_t)$ . They can also be expressed as products of the dimensionless scalar or tensor fields  $\mu_r$  and  $\varepsilon_r$ , and constants  $\mu_0$  and  $\varepsilon_0$ , which are named relative permeability, relative permittivity, vacuum

permeability, and vacuum permittivity, respectively. The two constants  $\mu_0$  and  $\varepsilon_0$  relate to the speed of light in vacuum  $c$  with

$$c^2 = \frac{1}{\mu_0 \varepsilon_0}. \quad (2.15)$$

To express  $\mathbf{H}$  in terms of  $\mathbf{B}$ , the magnetic reluctivity  $\nu = \mu^{-1}$  and relative reluctivity  $\nu_r = \mu_r^{-1}$  can be used. Ohm's law (2.8) becomes in frequency domain

$$\mathbf{J} = \sigma \mathbf{E} + \mathbf{J}_s \equiv \mathbf{J}_c + \mathbf{J}_s, \quad (2.16)$$

with the electric conductivity  $\sigma = \mathcal{F}(\sigma_t)$ , and the frequency-domain source current density  $\mathbf{J}_s$  and conduction current density  $\mathbf{J}_c$ .

The fields of the frequency-domain Maxwell equations (2.11) can, instead of denoting the Fourier transforms of arbitrary time-domain functions, also simply stand for the phasors of sinusoidal functions of a single angular frequency  $\omega$ . E.g., the phasor  $\mathbf{E}$  determines the time-domain electric field

$$\mathcal{E}(t, \mathbf{r}) = \text{Re} \left( \mathbf{E}(\mathbf{r}) e^{j\omega t} \right). \quad (2.17)$$

This is the perspective most useful in the context of the theory of time-harmonic electrical networks discussed in Chapter 4, and also provides the basis of the general parasitic extraction method introduced in Chapter 5.

In the following, the discussion of electrodynamic quantities and equations is restricted to frequency domain.

### 2.3. Interface and Boundary Conditions

Interface conditions describe the fields' continuity at the interface of two media and are derived using the integral form of Maxwell's equations (2.5). Fig. 2.1 shows two interfacing media, with the permittivity  $\varepsilon$ , permeability  $\mu$  and conductivity  $\sigma$  taking the values  $\varepsilon_1, \mu_1$ , and  $\sigma_1$  in the first medium and  $\varepsilon_2, \mu_2$ , and  $\sigma_2$  in the second medium, respectively. The unit normal of the interface from medium 1 to medium 2 is denoted by  $\hat{\mathbf{n}}_{12}$ . The interface conditions can be found by choosing the integration surface  $\Sigma$  of (2.5a) and (2.5b) and integration region  $\Omega$  of (2.5c) and (2.5d) as depicted in the figure such that half of both  $\Sigma$  and  $\Omega$  lies in each of the media. Letting the height parameter  $h$  approach zero causes the surface area of  $\Sigma$  and volume of  $\Omega$  to vanish. After a transition to frequency domain, the equations (2.5) thereby lead to the following interface conditions [Jac99, Section I.5]

$$\hat{\mathbf{n}}_{12} \times (\mathbf{E}_2 - \mathbf{E}_1) = 0, \quad (2.18a)$$

$$\hat{\mathbf{n}}_{12} \times (\mathbf{H}_2 - \mathbf{H}_1) = \mathbf{K}, \quad (2.18b)$$

$$\hat{\mathbf{n}}_{12} \cdot (\mathbf{D}_2 - \mathbf{D}_1) = \varsigma, \quad (2.18c)$$

$$\hat{\mathbf{n}}_{12} \cdot (\mathbf{B}_2 - \mathbf{B}_1) = 0. \quad (2.18d)$$

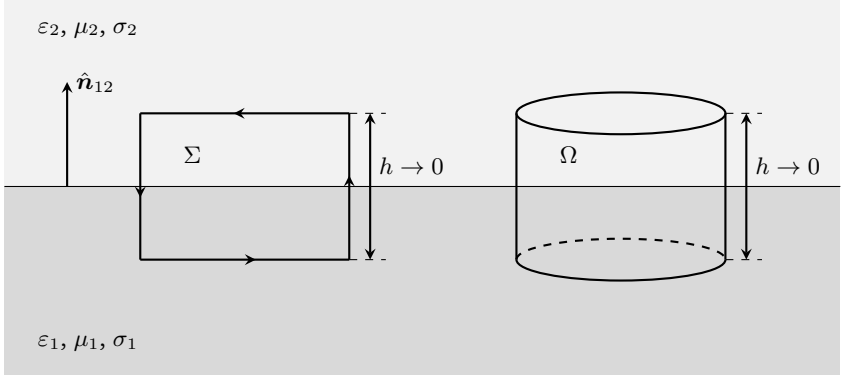


Figure 2.1.: Choice of integration surface  $\Sigma$  and region  $\Omega$  that yields the interface conditions for the fields of Maxwell's equations (2.5).

The different indices denote the values of the fields on the two sides of the boundary,  $\mathbf{K}$  is a potentially present idealized surface current density parallel to the surface and  $\varsigma$  is an idealized surface charge density. This result highlights an important difference between the field strengths  $\mathbf{E}$  and  $\mathbf{H}$ , and the flux densities  $\mathbf{D}$  and  $\mathbf{B}$ : In the absence of idealized surface current densities  $\mathbf{K}$  and charge densities  $\varsigma$ , the field strengths must possess a continuous tangential component over material boundaries whereas for the flux densities the normal component must be continuous.

In order to solve the frequency-domain Maxwell equations (2.11) in a computational domain  $\Omega \subseteq \mathbb{R}^3$ , they have to be considered in a boundary value problem (BVP) by supplementing them with boundary conditions on  $\partial\Omega$ . The simplest boundary conditions for electromagnetic problems are the electric boundary condition (EBC) and magnetic boundary condition (MBC), which demand that the tangential components of electric field strength  $\mathbf{E}$  and magnetic field strength  $\mathbf{H}$  vanish at the boundary  $\partial\Omega$  of the computational domain. They can be derived either by assuming an electric or magnetic symmetry (cf. [STH87]), or by requiring the electric or magnetic field strength to vanish outside the computational domain and using the interface conditions (2.18a) and (2.18b), respectively. The case of a vanishing electric field corresponds to assuming a perfect electric conductor outside the boundary. The EBC and MBC read

$$\hat{\mathbf{n}} \times \mathbf{E} = 0 \quad \text{on } \Gamma_{\text{el}}, \quad (2.19)$$

$$\hat{\mathbf{n}} \times \mathbf{H} = 0 \quad \text{on } \Gamma_{\text{mag}}. \quad (2.20)$$

Here,  $\Gamma_{\text{el}} \subseteq \partial\Omega$  and  $\Gamma_{\text{mag}} \subseteq \partial\Omega$  denote the parts of the boundary  $\partial\Omega$  on which the EBC and MBC are assumed, respectively, and  $\hat{\mathbf{n}}$  is again the normal on  $\partial\Omega$ . Whereas for  $\mathbf{H}$  the

MBC (2.20) is a homogeneous Dirichlet boundary condition, it becomes a homogeneous Neumann boundary condition for  $\mathbf{E}$  at frequencies  $\omega \neq 0$  through Faraday's law (2.11b) and the constitutive relation (2.14a),

$$\hat{\mathbf{n}} \times \nu \operatorname{curl} \mathbf{E} = 0 \quad \text{on } \Gamma_{\text{mag}}. \quad (2.21)$$

A second corollary of (2.20) is found by applying the divergence operator to the equation and using the vector calculus identity

$$\operatorname{div}(\mathbf{a} \times \mathbf{F}) = -\mathbf{a} \cdot \operatorname{curl} \mathbf{F} \quad \text{for all } \mathbf{a} \in \mathbb{R}^3 \text{ and smooth } \mathbf{F} : \mathbb{R}^3 \rightarrow \mathbb{C}^3. \quad (2.22)$$

With the Ampère-Maxwell law (2.11a) and constitutive relation (2.14b), and if  $\mathbf{J} \cdot \hat{\mathbf{n}} = 0$  on  $\Gamma_{\text{mag}}$  and  $\omega \neq 0$ , this yields

$$\hat{\mathbf{n}} \cdot \varepsilon \mathbf{E} = 0 \quad \text{on } \Gamma_{\text{mag}}. \quad (2.23)$$

## 2.4. Potential Formulation

For both the analytical and numerical solution of Maxwell's equations it is often convenient to transform the original set of four first-order PDEs (2.11) to a smaller number of second-order PDEs. One way to achieve this is by introducing the magnetic vector potential (MVP)  $\mathbf{A}$  and electric scalar potential (ESP)  $\phi$ , that fulfill Gauss's law for magnetism (2.11d) and Faraday's law (2.11b) implicitly through their defining equations. The former law states that  $\mathbf{B}$  is divergence-free or *solenoidal*. It can therefore be expressed as the curl of a vector potential  $\mathbf{A}$

$$\mathbf{B} = \operatorname{curl} \mathbf{A}, \quad (2.24)$$

with  $\mathbf{A}$  fulfilling (2.11d) by definition (as  $\operatorname{div} \operatorname{curl} \mathbf{A} = 0$  for any sufficiently differentiable vector field  $\mathbf{A}$ ). Expressing  $\mathbf{B}$  with (2.24) in Faraday's law (2.11b) yields

$$\operatorname{curl}(\mathbf{E} + j\omega \mathbf{A}) = 0. \quad (2.25)$$

Since any curl-free or *irrotational* field can be expressed as the gradient of a scalar potential  $\phi$ , the electric field becomes

$$\mathbf{E} = -\operatorname{grad} \phi - j\omega \mathbf{A}. \quad (2.26)$$

Expressing the Ampère-Maxwell law (2.11a) and Gauss's law (2.11c) with the potentials (and using the constitutive relations (2.14)) yields

$$\operatorname{curl}(\nu \operatorname{curl} \mathbf{A}) + j\omega \varepsilon \operatorname{grad} \phi - \omega^2 \varepsilon \mathbf{A} = \mathbf{J}, \quad (2.27a)$$

$$-\operatorname{div}(\varepsilon \operatorname{grad} \phi) - j\omega \operatorname{div}(\varepsilon \mathbf{A}) = \rho. \quad (2.27b)$$

This introduction of the potentials contains a certain freedom of choice: For an arbitrary scalar field  $\psi$  also the potentials

$$\mathbf{A}' = \mathbf{A} + \text{grad } \psi, \quad (2.28a)$$

$$\phi' = \phi - j\omega\psi \quad (2.28b)$$

fulfill (2.27) and yield the same physical fields  $\mathbf{E}$  and  $\mathbf{B}$ . This so-called gauge invariance can be resolved by supplementing a gauge condition that eliminates the arbitrariness in the equations. Some numerical solution techniques, especially those relying on direct linear equation solvers, require the enforcement of a gauge condition. More fundamentally, however, gauge conditions are often already used in the formulation of the PDEs to decouple the two equations (2.27a) and (2.27b).

For considerations involving only homogeneous isotropic materials (i.e.,  $\varepsilon$ ,  $\mu$ , and  $\sigma$  are scalars rather than scalar or tensor fields), the two most widely used gauge conditions are the Coulomb gauge,

$$\text{div } \mathbf{A} = 0, \quad (2.29)$$

which simply sets the irrotational part of the MVP to zero, and the Lorenz gauge

$$\text{div } \mathbf{A} + \frac{j\omega}{c_m^2} \phi = 0. \quad (2.30)$$

Here,  $c_m = 1/\sqrt{\varepsilon\mu}$  denotes the speed of light in a medium (in vacuum  $c_m = c$ ). The Coulomb gauge only eliminates the MVP  $\mathbf{A}$  from Gauss's law (2.27b), such that the ESP  $\phi$  can be calculated in a first step with (2.27b), which can then be used in a second step to calculate  $\mathbf{A}$  with (2.27a). The Lorenz gauge, however, renders both equations of (2.27) fully independent, which yields

$$\Delta \mathbf{A} + \frac{\omega^2}{c_m^2} \mathbf{A} = -\mu \mathbf{J}, \quad (2.31a)$$

$$\Delta \phi + \frac{\omega^2}{c_m^2} \phi = -\frac{\rho}{\varepsilon}. \quad (2.31b)$$

The Laplace operator  $\Delta$  is defined here for scalar fields  $f : \mathbb{R}^n \rightarrow \mathbb{C}$  and vector fields  $\mathbf{f} : \mathbb{R}^3 \rightarrow \mathbb{C}^3$  as

$$\Delta f := \text{div grad } f, \quad (2.32a)$$

$$\Delta \mathbf{f} := \text{grad div } \mathbf{f} - \text{curl curl } \mathbf{f}. \quad (2.32b)$$

The form of (2.31) enables the use of Green's functions to connect the potentials directly to source current densities and source charge densities by integration. This forms the basis of integral methods such as PEEC [Rue74] and the boundary element method [BTW84].

If there are inhomogeneous or anisotropic materials to be considered, it is warranted to use the generalized Coulomb and Lorenz gauges [Nis57],

$$\operatorname{div}(\varepsilon_r \mathbf{A}) = 0, \quad (2.33)$$

$$\operatorname{div}(\varepsilon_r \mathbf{A}) + \frac{j\omega}{c^2} \phi = 0. \quad (2.34)$$

These gauges facilitate a decoupling of (2.27a) and (2.27b) also in the presence of an inhomogeneous permittivity  $\varepsilon$ .

## 2.5. Static and Quasistatic Approximations

Static and quasistatic approximations to Maxwell's equations are widely used to facilitate or simplify both analytic and numerical solutions. In the context of parasitic extraction, they can be applied to isolate or preclude resistive, inductive or capacitive effects (cf. Section 5.2). All of these approximations arise by fully or partly neglecting the coupling of electric and magnetic fields in Maxwell's equations. The absence of any static or quasistatic approximation is therefore sometimes referred to as the *full wave* case, as only a full coupling of electric and magnetic fields results in the PDEs supporting wave solutions. In time domain the approximations amount to neglecting some or all time derivatives in Maxwell's equations, which translates to the neglect of terms proportional to the angular frequency  $\omega$  or its square in frequency domain. In the following, an overview of different approximations to the frequency-domain Maxwell equations (2.11) is given.

The **electro- and magnetostatic approximations** assume all fields in Maxwell's equations to be approximately stationary (i.e., constant in time). Hence, they neglect all frequency dependent terms in (2.11), which leads to a full decoupling of electric and magnetic effects. The continuity equation (2.12) degenerates to

$$\operatorname{div} \mathbf{J} = 0, \quad (2.35)$$

i.e., only divergence-free current densities are allowed. Furthermore, no coupling of  $\mathbf{J}$  to  $\mathbf{E}$  via Ohm's law (2.16) is permitted, thereby precluding resistive effects. In electrostatics only capacitive effects remain whereas magnetostatics is concerned exclusively with inductive effects. Faraday's law (2.11b) demands in absence of the  $j\omega \mathbf{B}$  term that the electric field  $\mathbf{E}$  is irrotational. Therefore it can be expressed with only the ESP  $\phi$ , and Gauss's law (2.11c) becomes the electrostatic (ES) PDE

$$-\operatorname{div}(\varepsilon \operatorname{grad} \phi) = \rho. \quad (2.36)$$

Without the displacement current  $j\omega \mathbf{D}$ , the Ampère-Maxwell law (2.11a) turns it into Ampère's law, which yields for the MVP  $\mathbf{A}$  the magnetostatic (MS) PDE

$$\operatorname{curl}(\nu \operatorname{curl} \mathbf{A}) = \mathbf{J}. \quad (2.37)$$

The **electroquasistatic (EQS) approximation** neglects only the  $j\omega\mathbf{B}$  term in Faraday's law (2.11b). The continuity equation (2.12) and Ohm's law (2.16) stay valid, and both capacitive and resistive effects are considered in a PDE for the ESP  $\phi$ :

$$-\operatorname{div}((\sigma + j\omega\varepsilon)\operatorname{grad}\phi) = -\operatorname{div}\mathbf{J}_s. \quad (2.38)$$

The **magnetoquasistatic (MQS) approximation**, also referred to as eddy current approximation, neglects only the displacement current  $j\omega\mathbf{D}$  in the Ampère-Maxwell law. As in the magnetostatic approximation, only divergence-free current densities are permitted due to the degenerated continuity equation (2.35). However, resistive effects are included with Ohm's law (2.16). This allows for eddy currents in conductors and hence considers the skin and proximity effects [Jac99, Section 5.18]. As the PDEs of the MQS approximation simplify to the magnetostatic PDE (2.37) in the absence of a conduction current  $\mathbf{J}_c = \sigma\mathbf{E}$ , they are stated here with Ohm's law already applied. In potential formulation they read

$$\operatorname{curl}(\nu\operatorname{curl}\mathbf{A}) + \sigma(\operatorname{grad}\phi + j\omega\mathbf{A}) = \mathbf{J}_s, \quad (2.39a)$$

$$\operatorname{div}(\sigma(\operatorname{grad}\phi + j\omega\mathbf{A})) = \operatorname{div}\mathbf{J}_s. \quad (2.39b)$$

The first equation already contains (2.39b) as its divergence. The scalar equation (2.39b) is provided to obtain matching numbers of equations and undetermined fields.

The **Darwin approximation** [Lar07; DR92], sometimes referred to as full quasistatics or electromagnetoquasistatic approximation, considers resistive, inductive, and capacitive effects while only precluding wave effects. The approximation is typically made by expressing Maxwell's equations with an MVP  $\mathbf{A}$  and ESP  $\phi$ , thereby neglecting the second-order time derivatives in the equations or, in frequency domain (2.27), the terms quadratic in  $\omega$ , as those are the terms causing retardation and wave effects. The approximation is most commonly discussed in literature for homogeneous isotropic materials, and usually in the Coulomb gauge (2.29). In this case, the expression of  $\mathbf{E}$  with the potentials (2.26) amounts to a Helmholtz decomposition, splitting the electric field into an irrotational and a solenoidal part, and Darwin approximation neglects precisely the solenoidal contribution to the displacement current, i.e., the  $\omega^2$  term in (2.27a). In Lorenz gauge (2.30) (with homogeneous isotropic materials) no Helmholtz decomposition of  $\mathbf{E}$  takes place, and the approximation is made by neglecting the  $\omega^2$  terms in both (2.31a) and (2.31b). This latter approach is equivalent to the way retardation is neglected in the PEEC method [Rue74]. In general, applying Darwin's approximation to the Ampère-Maxwell law (2.11a) yields the Ampère-Darwin equation

$$\operatorname{curl}(\nu\operatorname{curl}\mathbf{A}) + j\omega\varepsilon\operatorname{grad}\phi = \mathbf{J}. \quad (2.40)$$



---

## 3. Finite Element Method

---

### 3.1. Basic Concepts

The finite element method (FEM) [Cia78; BS08] is a numerical solution method for PDEs. It considers the differential equations in weak form, which in the linear case considered in this work amounts to solving the variational problem

$$\text{find } u \in X : \quad a(u, v) = f(v) \quad \forall v \in X. \quad (3.1)$$

Here,  $u$  denotes the solution,  $X$  is its function space,  $a$  is a sesquilinear form,  $f$  is a linear form, and  $v$  is a test function. The function space  $X$  must be a Sobolev space, i.e., a space of functions that are finite with respect to some norm and whose derivatives appearing in the weak-form differential equations are finite as well. The variational problem can be discretized in a very straightforward fashion through Galerkin projection, in which the Sobolev space  $X$  is replaced with a finite-dimensional subspace  $X_h \subset X$ . The case considered here, in which  $X_h$  is a subset of  $X$ , is referred to as  $X$ -conforming (cf. Section 3.2). The discretized variational problem hence reads

$$\text{find } u_h \in X_h : \quad a(u_h, v) = f(v) \quad \forall v \in X_h, \quad (3.2)$$

with  $u_h$  being an approximation to the solution  $u$  of the continuous problem. Subtracting the discretized problem (3.2) from the continuous one (3.1) for those test functions  $v \in X_h$  shows the Galerkin orthogonality of the error  $\epsilon := u - u_h$ ,

$$a(\epsilon, v) = a(u, v) - a(u_h, v) = f(v) - f(v) = 0 \quad \forall v \in X_h, \quad (3.3)$$

i.e., the property that the error is orthogonal to all functions in  $X_h$ . Thus  $u_h$  is the optimal approximation possible with functions of  $X_h$ . The choice of the finite-dimensional subspace  $X_h$  is therefore of paramount importance to obtain a good approximation  $u_h$ .

In the FEM this choice is determined by the finite elements. In the classical definition of Ciarlet [Cia78; Mon03] a finite element in a computational domain  $\Omega \subset \mathbb{R}^n$  is a triple  $(K, P, \Sigma)$  where

- $K$  is a closed, non-empty subdomain of  $\Omega$  with a Lipschitz-continuous boundary (e.g., a tetrahedron, hexahedron or prism),

- $P_K$  is a space of functions on  $K$  (usually polynomials).
- $\Sigma_K$  is a finite set of linear functionals on  $P$ , which are referred to as the degrees of freedom (DoFs). These functionals must be unisolvent in the sense that specifying a value for each of the DoFs in  $\Sigma_K$  uniquely determines a function in  $P_K$ .

In a less formal sense, the term finite element is also often applied directly to the subdomain  $K$  (even by Ciarlet [Cia78]). For a set  $\Sigma_K$  of  $n_K$  DoFs  $l_i^K$  the unisolvence requirement is usually fulfilled by defining a set  $\{\varphi_j^K\}_{j=1}^{n_K}$  of  $n_K$  basis functions  $\varphi_j^K$  with

$$\varphi_j^K \in P_K \quad \text{and} \quad l_i^K(\varphi_j) = \delta_{i,j} := \begin{cases} 1 & \text{if } i = j, \\ 0 & \text{otherwise.} \end{cases} \quad (3.4)$$

Thus any function  $f \in P_K$  can be expressed as

$$f = \sum_{j=1}^{n_K} l_j^K(f) \varphi_j^K. \quad (3.5)$$

To construct the finite-dimensional subspace  $X_h \subset X$ , the computational domain  $\Omega$  is partitioned into a finite set  $\mathcal{T}_h$  of such subdomains  $K$  with disjoint interiors,

$$\mathcal{T}_h = \{K\} \quad \text{with} \quad \cup_{K \in \mathcal{T}_h} K = \Omega. \quad (3.6)$$

The set  $\mathcal{T}_h$  is referred to as triangulation or mesh of the domain and its elements  $K$  are the cells of the mesh. The vertices, edges and faces of the polyhedral cells are thus called the nodes, edges, and faces of the mesh, respectively. A basis for the global space  $X_h$  can be constructed from the basis functions of the local spaces  $P_K$  by identifying the local DoFs  $l_i^K \in \Sigma_K$  with global DoFs  $l_i \in \Sigma$  through the mappings  $m_K : \Sigma_K \rightarrow \Sigma$ . These mappings must identify some of the local DoFs of each pair of touching cells with each other such that the continuity requirements of the function space  $X$  are fulfilled: Typically, the local DoFs and basis functions are in some sense associated with the nodes, edges, faces or volume of the cell  $K$  (examples are provided with the discussion of the Sobolev spaces  $H^1$  and  $H(\text{curl})$  in the following section). The mappings then identify those local basis functions with each other that belong to a node, edge or face shared between different cells of the mesh. Hence, each global DoF  $l_i$  is identified with only a small number of local DoFs; the global basis function  $\varphi_i \in X_h$  corresponding to  $l_i$  has support only on the cells associated with these local DoFs and is zero everywhere else. Following this procedure, any global function  $f \in X_h$  can, analogously to the local case (3.5), be uniquely determined with its DoFs,

$$f = \sum_{j=1}^n l_j(f) \varphi_j, \quad (3.7)$$

with  $n$  being the dimension of  $X_h$ . In each of the mesh cells,  $\varphi_i$  is equal to its local counterpart. Integrals containing a global basis function  $\varphi_i$  can therefore be expressed as a sum of integrals over the cells  $K$  of the local basis functions  $\varphi_i^K$  associated with  $\varphi_i$ .

To mesh a domain  $\Omega$  with one kind of element (e.g., tetrahedra), only a single reference finite element  $(\hat{K}, \hat{P}, \hat{\Sigma})$  has to be defined. Any point  $\mathbf{x} \in K$  ( $K \in \mathcal{T}_h$ ) can then be associated with a point  $\hat{\mathbf{x}} \in \hat{K}$  via an invertible mapping  $F_K : \hat{K} \rightarrow K$ , such that  $F_K(\hat{K}) = K$ . In the case of tetrahedra with straight edges relevant for this work the mappings  $F_K$  are affine,

$$F_K(\hat{\mathbf{x}}) = \mathbf{B}_K \hat{\mathbf{x}} + \mathbf{b}_K, \quad (3.8)$$

i.e., they can be expressed with an invertible matrix  $\mathbf{B}_K$  and a vector  $\mathbf{b}_K$ . See [Mon03, Section 5.3] for a discussion on how the mappings  $F_K$  are used to express integrals over  $K$  containing local basis functions  $\varphi_i^K \in P_K$  with integrals over the reference cell  $\hat{K}$  containing the reference basis functions  $\hat{\varphi} \in \hat{P}$ .

## 3.2. Conforming Finite Elements

As discussed in the previous section, the quality of a Galerkin approximation  $u_h \in X_h$  to the actual solution  $u \in X$  of a variational problem is determined by the choice of the finite-dimensional subspace  $X_h \subset X$ . In the FEM, this choice depends obviously on the resolution and quality of the chosen mesh  $\mathcal{T}_h$  of the domain  $\Omega$ . More fundamentally, however, it depends on the basis functions of the local function spaces  $P_K$  which imply the solution's continuity properties across cells. A set  $\{(K, P, \Sigma)\}$  of finite elements that constructs a global subspace  $X_h \subset X$  is called  $X$ -conforming. This label can also be applied to the reference element  $(\hat{K}, \hat{P}, \hat{\Sigma})$  of the set.

The FEM was first developed for a class of problems in structural mechanics where all components of the the solution are continuous [Bat14] and thus lie in the Sobolev space  $H^1$ . In electrodynamics the FEM was first applied to 2D problems, that share this continuity [Bos98]. In the general 3D case, however, the fields of Maxwell's equations (2.11) obey less strict continuity relations, as discussed in Section 2.3. A pivotal moment for computational electromagnetism was therefore the introduction of Nédélec's sets of finite elements [Néd80], one of which conforms to the Sobolev space  $H(\text{curl})$  (the space of  $\mathbf{E}$  and  $\mathbf{H}$  in Maxwell's equations) and the other to  $H(\text{div})$  (the space of  $\mathbf{B}$  and  $\mathbf{D}$ ). The following two subsections introduce the Sobolev spaces  $H^1$  (used in 3D-electrodynamics for scalar potentials) and  $H(\text{curl})$ , as well as their associated finite elements on tetrahedra. In addition to facilitating field computations in the presence of inhomogeneous materials, the use of these  $H(\text{curl})$ -conforming elements also resolves the issue of spurious gradient field components in the eigenmodes of cavities [Bos98, Section 9.3.3]. This result is best understood with the de Rham complex, that relates the Sobolev spaces  $H^1$ ,  $H(\text{curl})$ , and  $H(\text{div})$  to each other and is the subject of Subsection 3.2.3.

### 3.2.1. $H^1$ -conforming elements

Scalar fields onto which the gradient operator is applied in a PDE in weak form must lie in the Sobolev space  $H^1(\Omega)$ . It is defined as

$$H^1(\Omega) \equiv H(\text{grad}, \Omega) := \{\psi \in L^2(\Omega) : \text{grad } \psi \in L^2(\Omega)\}, \quad (3.9)$$

where  $L^2(\Omega)$  is the space of square-integrable functions on  $\Omega$ ,

$$L^2(\Omega) := \{\psi : \int_{\Omega} |\psi|^2 dV < \infty\}. \quad (3.10)$$

Differential operators on square-integrable functions like the gradient in (3.9) are to be understood in the weak or distributional sense (cf. [Mon03, Section 3.2]), such that they can also be applied to functions that are differentiable only almost everywhere in  $\Omega$  in the strong sense (i.e., in the context of the FEM, everywhere except on the boundaries of the mesh cells). Due to the finite gradient of  $H^1$  functions implied by (3.9), elements that conform to  $H^1$  express scalar fields that are continuous across the boundaries of the mesh cells. For a reference tetrahedron as depicted in Fig. 3.1a, a set of  $H^1$ -conforming basis functions of the lowest order  $p = 1$ , i.e., a set of linear polynomials, is found with the barycentric coordinate functions  $\hat{\psi}_i$  corresponding to the nodes  $\hat{\mathbf{a}}_i$ ,

$$\hat{\psi}_1 = 1 - x - y - z, \quad \hat{\psi}_2 = x, \quad \hat{\psi}_3 = y, \quad \hat{\psi}_4 = z. \quad (3.11)$$

The associated DoFs  $\hat{l}_i$  applied to a function  $\hat{f} : \hat{K} \rightarrow \mathbb{C}$  just yield the value  $\hat{f}(\hat{\mathbf{a}}_i)$  of the function at the corresponding node  $\hat{\mathbf{a}}_i$ . Due to the lowest-order basis functions being associated with the nodes of the mesh,  $H^1$ -conforming elements are also referred to as *node elements*. Basis functions of a higher polynomial order  $p > 1$  enable a better-than-linear approximation of functions inside the mesh cells. They can be constructed directly from the  $p = 1$  functions [Ing06], e.g., for  $p = 2$  as the set  $\{\psi_i \hat{\psi}_j\}_{i < j}$ . These basis functions are thus associated not with single nodes but rather edges, faces, or cells of the mesh, being constructed with two, three, or four first-order basis functions, respectively.

### 3.2.2. $H(\text{curl})$ -conforming elements

Vector fields onto which the curl operator is applied in a weak-form PDE must lie in the Sobolev space

$$H(\text{curl}, \Omega) := \{\mathbf{v} \in L^2(\Omega)^3 : \text{curl } \mathbf{v} \in L^2(\Omega)^3\}. \quad (3.12)$$

This space is larger than and in fact contains  $H^1(\Omega)^3$ , which is the space of 3D vector fields with continuous components. For any partitioning (3.6) of the domain  $\Omega$  into a finite set of subdomains  $K$ , functions in  $H(\text{curl}, \Omega)$  require only tangential continuity across boundaries  $\partial K$  of the cells, i.e., the normal component may be discontinuous. In the context

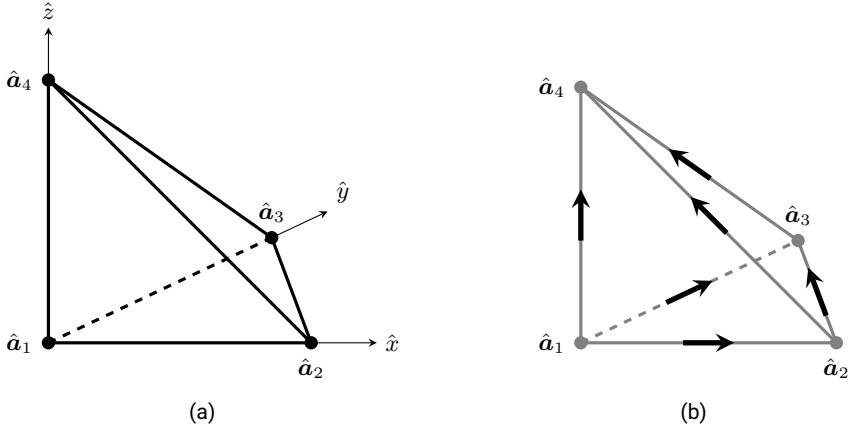


Figure 3.1.: (a) Reference tetrahedron with nodes  $\hat{\mathbf{a}}_1 = (0, 0, 0)^\top$ ,  $\hat{\mathbf{a}}_2 = (1, 0, 0)^\top$ ,  $\hat{\mathbf{a}}_3 = (0, 1, 0)^\top$ , and  $\hat{\mathbf{a}}_4 = (0, 0, 1)^\top$ . (b)  $H(\text{curl})$ -conforming basis functions of order  $p = 1$  on the reference tetrahedron symbolized by arrows on their associated edges.

of computational electromagnetics, the interface conditions (2.18a) and (2.18b) of the electric and magnetic field strengths can thus be fulfilled by the meshing the computational domain  $\Omega$  such that the boundaries between different media coincide with the boundaries of the mesh cells, and using  $H(\text{curl})$ -conforming basis functions to approximate  $\mathbf{E}$  and  $\mathbf{H}$ . The  $H(\text{curl})$ -conforming finite elements introduced by Nédélec [Néd80] are called *edge elements* since their lowest-order  $p = 1$  basis functions are associated with the edges of the mesh. For tetrahedral meshes, the  $p = 1$  basis function  $\hat{\mathbf{e}}_{ij}$  associated with the edge joining the nodes  $i$  and  $j$  can be expressed with the  $H^1$ -conforming nodal basis functions  $\hat{\psi}_i$  of (3.11) as

$$\hat{\mathbf{e}}_{ij} = \hat{\psi}_i \text{grad } \hat{\psi}_j - \hat{\psi}_j \text{grad } \hat{\psi}_i. \quad (3.13)$$

Fig. 3.1b illustrates all six of these first order basis functions on the reference tetrahedron. A basis for  $H(\text{curl})$ -conforming elements that includes higher order polynomials can be constructed in different ways. A standard way for order  $p \leq 2$  is given in [Mon03, Subsection 5.2.2]. In this work, however, the hierarchical basis functions of [Ing06] are used, as they facilitate an easy removal of the gradient fields contained in the function space of the elements, which is needed for the low-frequency stable discretization discussed in Chapter 6.

### 3.2.3. De Rham complex

In order to discuss some fundamental relationships between the differential operators grad, curl, and div, and their associated Sobolev spaces  $H^1(\Omega)$ ,  $H(\text{curl}, \Omega)$ , and  $H(\text{div}, \Omega)$ , the space  $H(\text{div}, \Omega)$  remains to be defined,

$$H(\text{div}, \Omega) := \{\mathbf{v} \in L^2(\Omega)^3 : \text{div } \mathbf{v} \in L^2(\Omega)\}. \quad (3.14)$$

Analogously to the tangential continuity of fields from  $H(\text{curl}, \Omega)$  across the boundaries of subdomains within  $\Omega$ , fields that lie in  $H(\text{div}, \Omega)$  must have a continuous normal component across these boundaries. This property agrees with the interface conditions (2.18a) and (2.18b) of the electric and magnetic flux densities  $\mathbf{D}$  and  $\mathbf{B}$ .

For any  $\psi \in H^1(\Omega)$  it holds that  $\text{grad } \psi \in H(\text{curl}, \Omega)$ , since  $\text{curl } \text{grad } \psi = 0 \in L^2(\Omega)^3$ . Analogously for any  $\mathbf{v} \in H(\text{curl}, \Omega)$  it follows that  $\text{curl } \mathbf{v} \in H(\text{div}, \Omega)$ , since  $\text{div } \text{curl } \mathbf{v} = 0 \in L^2(\Omega)$ . These properties also translate to the finite-dimensional subspaces of conforming finite elements: Let  $P_h \subset H^1(\Omega)$  be a global function space constructed with the  $H^1$ -conforming elements of Subsection 3.2.1,  $Q_h \subset H(\text{curl}, \Omega)$  be a global function space constructed with the  $H(\text{curl})$ -conforming elements of the previous subsection, and  $R_h \subset H(\text{div}, \Omega)$  be a global function space constructed with the  $H(\text{div})$ -conforming elements of [Néd80]. Then, the relationships between the infinite-dimensional Sobolev spaces and their finite-dimensional subspaces are captured in the de Rham complex [Mon03, Section 5.7]:

$$\begin{array}{ccccccc} H^1(\Omega) & \xrightarrow{\text{grad}} & H(\text{curl}, \Omega) & \xrightarrow{\text{curl}} & H(\text{div}, \Omega) & \xrightarrow{\text{div}} & L^2(\Omega) \\ \cup & & \cup & & \cup & & \cup \\ P_h & \xrightarrow{\text{grad}} & Q_h & \xrightarrow{\text{curl}} & R_h & \xrightarrow{\text{div}} & S_h \end{array} \quad (3.15)$$

Here,  $S_h \subset L^2(\Omega)$  denotes a space constructed with discontinuous finite elements. For contractible domains  $\Omega$ , the meaning of (3.15) is that the range of one operator coincides with the kernel of the next operator in the sequence, e.g.,  $\text{ran}(\text{grad}) = \ker(\text{curl})$ . The sequence holds both when applying the operators to their respective infinitely-dimensional spaces of the first row and when restricting them to the FE spaces of the second row. For the first level of the sequence this means

$$\text{grad } P_h \subset Q_h \quad \text{and} \quad \mathbf{v} \in \text{grad } P_h \Leftrightarrow \text{curl } \mathbf{v} = 0. \quad (3.16)$$

This property facilitates the low-frequency stabilization discussed in Chapter 6.

In the case that perfect electric conductors are used, the domain of the differential equation (5.26a) determining  $\mathbf{E}$  is only the non-conducting subdomain  $\Omega_0 = \Omega \setminus \Omega_c$ , which includes cavities and is thus not contractible. However, cavities included in the domain only affect the second level of the de Rham complex, causing the kernel of the divergence to contain an additional component aside from the range of curl [Bos88]. Therefore, (3.16) still holds in this case.

---

The de Rham complex (3.15) also clarifies why even in the case of homogeneous materials, e.g., in the cavity eigenmode computation mentioned in the introduction of this section, where the electric field  $\mathbf{E}$  is continuous,  $H(\text{curl})$ -conforming elements are superior to fully continuous elements conforming to  $(H^1)^3$ : The space  $Q_h$  constructed with  $H(\text{curl})$ -conforming basis functions also contains gradient fields and due to (3.3) the error must be orthogonal to these gradient fields. Expressing each of the components of a field with  $H^1$ -conforming elements, however, does not construct a space that explicitly contains gradients [Bos98, Section 6.3], and thus an FE approximation using such elements typically contains spurious gradient components.



---

## 4. Electrical Networks

---

While in the context of electrical engineering a description of electrical devices with Maxwell's equations is generally possible and for some questions unavoidable, it also has severe drawbacks:

- After discretization, the number of DoFs of field models is often in the millions. This makes some (especially transient) simulations prohibitively expensive.
- A high number of DoFs complicates the root cause analysis of potential issues, especially regarding EMC.
- The fact that different components of a device are often developed by different companies creates the need for independent mathematical descriptions of the single components, that can later be coupled in a joint simulation. Field models are generally impractical in this context.

Engineers typically avoid these drawbacks by using electrical circuits or networks [Van74; AS09] to describe devices and components. This replaces the PDEs of field theory with algebraic equations in the direct current (DC) and time-harmonic alternating current (AC) cases, and with ordinary differential equations in the transient case, and limits the DoFs to potentials on the nodes of the networks and currents through their branches.

As discussed in Chapter 1, the approach of parasitic extraction is to supplement available models of the functional elements of a circuit with the parasitic elements of the interconnects, the latter being determined in field simulations. However, accurately modeling the electromagnetic interactions both within and in-between electrical components with the reduced complexity of electrical networks can be a difficult task. The following section therefore establishes the connection between the electromagnetic fields and the basic passive network parameters resistance, inductance, capacitance, and the general impedance, and points out the limitations of a description with these quantities. Thereafter, Section 4.2 provides a graph-theoretical discussion of electrical networks.

### 4.1. Basic Passive Network Elements

Resistors, inductors, and capacitors are the most basic passive elements (i.e., elements that do not supply energy to the system) of electrical networks. They possess two terminals and

are defined by their corresponding parameters resistance  $R$ , inductance  $L$ , and capacitance  $C$ , which relate the current  $i$  through the element with the voltage  $v$  across it [Van74, Section 5.3]. Their respective  $i$ - $v$  relationships read in time domain:

$$\text{Resistor: } v = Ri. \quad \text{Inductor: } v = L \frac{di}{dt}. \quad \text{Capacitor: } i = C \frac{dv}{dt}. \quad (4.1)$$

Whereas resistances and capacitances are not allowed to couple to the parameters of other elements, a coupling between inductors is permitted through the mutual inductances  $L_{ij}$  discussed in Subsection 4.1.2. In (4.1) the parameters  $R$ ,  $L$ , and  $C$  are assumed to be constants in time and thus also in frequency in the time-harmonic case, which enables simple and efficient transient simulations. A transition to frequency domain, however, allows to consider the more general case that the parameters can be frequency dependent. Applying the Fourier transform (2.9) to (4.1) yields:

$$\text{Resistor: } V = RI. \quad \text{Inductor: } V = j\omega LI. \quad \text{Capacitor: } I = j\omega CV. \quad (4.2)$$

The Fourier transforms  $I$  and  $V$  of the current  $i$  and voltage  $v$  can also be understood as the phasors of time-harmonic currents and voltages, i.e.,

$$i(t) = \text{Re} \left( I e^{j\omega t} \right), \quad v(t) = \text{Re} \left( V e^{j\omega t} \right). \quad (4.3)$$

While frequency-dependent resistances, inductances, and capacitances do not complicate AC network simulations, their use in transient simulations would require the selection of an operating frequency if convolutions are to be avoided (cf. Chapter 7).

In the time-harmonic case, a network element can in general be described by a complex-valued impedance  $Z$  relating the phasors  $V$  and  $I$  with

$$V = ZI. \quad (4.4)$$

The impedances corresponding to the basic network elements of (4.2) are simply:

$$\text{Resistor: } Z_R = R. \quad \text{Inductor: } Z_L = j\omega L. \quad \text{Capacitor: } Z_C = \frac{1}{j\omega C}. \quad (4.5)$$

The following subsections discuss how the network parameters  $R$ ,  $L$ ,  $C$ , and  $Z$  can be assigned to structures consisting of conducting materials, dielectrics, and magnetic materials.

### 4.1.1. Resistance computation

The resistance  $R$  quantifies the power  $P$  that is dissipated if a current flows through the resistor. An expression for the time-averaged power  $\bar{P}$  that is lost in a network element with impedance  $Z$  is given by [FLS11, Section 22.5]

$$\bar{P} = \frac{1}{T} \int_0^T \operatorname{Re} \left( Z I e^{j\omega t} \right) \cdot \operatorname{Re} \left( I e^{j\omega t} \right) dt = \frac{1}{2} \operatorname{Re}(Z) |I|^2. \quad (4.6)$$

This means that  $\bar{P}$  only depends on the real part of the impedance, which can be identified as the resistance,

$$Z \equiv R + jX \quad \text{with } R, X \in \mathbb{R}. \quad (4.7)$$

The imaginary part  $X = \operatorname{Im}(Z)$  is named reactance. A network element with impedance  $Z$  is thus equivalent to a classical resistor obeying  $V = RI$  and an element with purely imaginary impedance (like an inductor or capacitor) in a series connection.

Subsection 4.1.4 provides a general method to compute the impedance  $Z$  and thus also the resistance  $R = \operatorname{Re}(Z)$ , that takes into account all kinds of dissipation, including ohmic and radiation losses, and losses in magnetic materials with complex permeability  $\mu$ . One useful special case, however, is that in which only ohmic losses are considered. There, all power dissipation is caused by the current density  $\mathcal{J}$  (in time domain) moving its charges against the electric field  $\mathcal{E}$ , which in network theory corresponds to the current's charges crossing the potential difference that is the voltage  $v$ . Equating the dissipated power of field description and network theory yields for the DC case

$$P = \int_{\Omega_c} \mathcal{E} \cdot \mathcal{J} dV = vi = Ri^2, \quad (4.8)$$

where  $\Omega_c$  is the space occupied by the resistor. This relationship can be generalized for the AC case by considering the time-average  $\bar{P}$  of the power over one time period  $T = 2\pi/\omega$

$$\bar{P} := \frac{1}{T} \int_0^T P dt = \frac{1}{T} \int_0^T \int_{\Omega_c} \operatorname{Re} \left( \mathbf{E} e^{j\omega t} \right) \cdot \operatorname{Re} \left( \mathbf{J} e^{j\omega t} \right) dV dt = \frac{1}{2} \int_{\Omega_c} |\mathbf{E}| |\mathbf{J}| \cos(\Delta\alpha) dV. \quad (4.9)$$

Here,  $\Delta\alpha$  denotes the phase difference between  $\mathcal{E}$  and  $\mathcal{J}$ , which is zero if the current density is a conduction current density (i.e.,  $\mathbf{J} = \sigma \mathbf{E}$ ) in  $\Omega_c$ . Then, the resistance is given by

$$R = \frac{1}{|I|^2} \int_{\Omega_c} \sigma |\mathbf{E}|^2 dV. \quad (4.10)$$

---

## 4.1.2. Inductance computation

### Loop inductance

The integral form of Faraday's law (2.5b) demands that charge carriers in a loop subject to a time-varying magnetic field experience an electromotive force equal to the negative time derivative of the total magnetic flux  $\Psi$  through the loop. In frequency domain this can be expressed by

$$\oint_l \mathbf{E} \cdot d\mathbf{l} = -j\omega \int_{S_l} \mathbf{B} \cdot \hat{\mathbf{n}} dS =: -j\omega\Psi. \quad (4.11)$$

Here, the loop  $l$  encloses the surface  $S_l$ . Assuming a negligible displacement current,  $j\omega\mathbf{D} \approx 0$  (i.e., the MQS approximation of Section 2.5), the magnetic field  $\mathbf{H}$  caused by a current  $I$  flowing through a conductor is independent of frequency and proportional to the current due to (2.5a),

$$\oint_{\partial\Sigma} \mathbf{H} \cdot d\mathbf{l} = \int_{S_J} \mathbf{J} \cdot \hat{\mathbf{n}} dS \equiv I. \quad (4.12)$$

Here,  $\partial\Sigma$  is an arbitrary loop around the conductor and  $S_J \subset \Sigma$  is the conductor's cross section, where  $\mathbf{J} \neq 0$ . This close relationship of  $I$  and  $\mathbf{H}$  translates directly to the magnetic flux  $\Psi$  in (4.11): For a set of  $N$  loops,  $N^2$  inductances  $L_{ij}$  are defined as the ratios

$$L_{ij} := \frac{\Psi_{ij}}{I_j} = \frac{1}{I_j} \int_{S_i} \mathbf{B}_{ij} \cdot \hat{\mathbf{n}} dS, \quad (4.13)$$

where  $I_j$  is the current in loop  $j$  and  $\Psi_{ij}$  is the magnetic flux through loop  $i = \partial S_i$  caused by  $I_j$  [RAJ16, Chapter 5]. Those inductances with  $i = j$  relating the current in and magnetic flux through the same loop are referred to as self-inductances whereas the inductances with  $i \neq j$  describing the coupling between loops are called mutual inductances.

The relationship of the inductance of (4.13) defined as the ratio of  $\Psi$  and  $I$  with the circuit inductance  $L$  of (4.2) becomes clear with Fig. 4.1, where the loop  $l$  of (4.11) is divided into a path  $c$  along a one dimensional conductor and a return path  $r$ , which meet at the terminals  $T_a$  and  $T_b$ . The return path stands in for a current source or voltmeter. The voltage  $V$  that must be applied at the terminals to transport charges along  $r$  must be the negative of that part of the line integral in (4.2) that goes along  $r$  [JB68, Section 14.6], i.e.,

$$V := - \int_r \mathbf{E} \cdot d\mathbf{l} = \int_c \mathbf{E} \cdot d\mathbf{l} + j\omega\Psi = RI + j\omega LI. \quad (4.14)$$

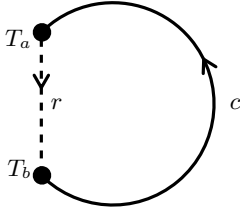


Figure 4.1.: [SKD22a] Loop consisting of a conducting wire  $c$  with terminals  $T_a$  and  $T_b$ , and a return path  $r$ . Based on an image from [JB68].

## Partial inductance

The inductance defined in (4.13) is a property of the current loop as a whole and therefore referred to as *loop inductance*. For the extraction of parasitic elements the concept of loop inductance is not useful: As only the interconnects are considered, the current paths through the DUT are undetermined during the extraction. The generalized concept of *partial inductance* [**paul\_inductance: 2010**; Rue72] utilizes the MVP  $\mathbf{A}$  to assign an inductance value to conductor segments. Let the loop  $l$  be composed of  $N$  segments  $l_i$ . Its loop inductance  $L_l$  defined in (4.13) can be split into a sum of partial inductances  $L_{p,i}$  by expressing the magnetic flux density with (2.24) as  $\mathbf{B} = \text{curl } \mathbf{A}$  and applying Stokes' theorem (2.3),

$$L_l = \frac{1}{I} \int_{S_l} \mathbf{B} \cdot \hat{\mathbf{n}} \, dS = \frac{1}{I} \oint_l \mathbf{A} \cdot d\mathbf{l} = \sum_{i=1}^N \frac{1}{I} \int_{l_i} \mathbf{A} \cdot d\mathbf{l} =: \sum_{i=1}^N L_{p,i}. \quad (4.15)$$

Each partial inductance  $L_{p,i}$  occurring in this equation still does not depend on only a single segment of the loop. The MVP  $\mathbf{A}$  in each of the line integrals is caused by the current in all segments. Expressing  $\mathbf{A}$  as a sum of contributions  $\mathbf{A}_j$  caused by the current in a single line segment  $j$  allows to formulate a general definition for partial inductances analogously to (4.13),

$$L_{p,ij} := \frac{1}{I_j} \int_{l_i} \mathbf{A}_j \cdot d\mathbf{l}. \quad (4.16)$$

With this definition, the line segments do not have to be part of the same loop (or any loop). The inductances of (4.16) are referred to as partial self-inductances if  $i = j$ , and as mutual partial inductances otherwise [**paul\_inductance: 2010**]. In the following, the partial inductances  $L_{p,i} = \sum_{j=1}^N L_{p,ij}$  occurring in (4.15) are referred to as total partial inductance of line segment  $l_i$ .

In contrast to physical quantities like  $\mathbf{E}$  and  $\mathbf{B}$ , partial inductances depend in principle on the gauge condition chosen for the MVP  $\mathbf{A}$ . The results presented Fig. 5.7, however, demonstrate that the Coulomb gauge (2.33) and Lorenz gauge (2.34) relevant in this work yield the same values.

## Inductance of three-dimensional conductors

Equation (4.14) is strictly applicable only for one-dimensional conductors, in which charges can only move along one path  $l$ . In the general three-dimensional case, the paths of the charges are determined by the current density  $\mathbf{J}$ , which is frequency dependent due to the skin effect. Generalizing the case of a homogeneous current density discussed in [RAJ16] for arbitrary current densities, a weighted average of (4.14) is found by integrating over the current cross section  $S_J$ ,

$$\begin{aligned} V &:= -\frac{1}{I} \int_{S_J} |\mathbf{J}| \int_r \mathbf{E} \cdot d\mathbf{l} dS_J = \frac{1}{I} \int_{S_J} |\mathbf{J}| \left( \int_c \mathbf{E} \cdot d\mathbf{l} + j\omega \int_{S_l} \mathbf{B} \cdot \hat{\mathbf{n}} dS_l \right) dS_J \\ &= (R + j\omega L)I. \end{aligned} \quad (4.17)$$

Here,  $d\mathbf{l}$  is parallel to  $\mathbf{J}$  for all points in the cross section  $S_J$ , and  $S_l$  is the surface that is enclosed by following  $\mathbf{J}$  starting at one point in  $S_J$ .

While the weighted average approach of (4.17) provides the basis for the general impedance computation method introduced in Section 4.1.4, for analytic considerations the alternative perspective of understanding the inductance as the sum of an external and internal inductance is useful [**paul\_inductance; 2010**]. Due to (4.12), the magnetic field outside the conductor depends only on the total current  $I$  in the conductor but not on its distribution. The external inductance  $L_{\text{ext}}$  is thus the frequency-independent part of  $L$  associated with the magnetic flux  $\Phi$  strictly outside the conductor, and can be computed by choosing the loop  $i$  in (4.13) (or, for partial inductances, the path  $l_i$  in (4.16)) such that it lies on the boundary of the conductor. The partial external inductance of a straight wire segment of length  $l$  with circular cross section of radius  $r$  is given in [**paul\_inductance; 2010**] as

$$L_{\text{ext}} = \frac{\mu_0 l}{2\pi} \left( \operatorname{arsinh} \left( \frac{l}{r} \right) - \sqrt{1 + \left( \frac{r}{l} \right)^2} + \frac{r}{l} \right). \quad (4.18)$$

The internal inductance  $L_{\text{int}}$  is most easily defined by equating the time average of the magnetic energy stored in the space  $\Omega_c$  occupied by the conductor with the time average of the energy stored by an inductance in circuit theory [RWV94]. As the skin effect forces the magnetic field out of the interior of the conductor for increasing frequencies, the internal inductance vanishes accordingly at high frequencies. The complex Poynting theorem [RWV94, Section 3.13] allows in the MQS approximation to compute the internal impedance  $Z_{\text{int}} = R + j\omega L_{\text{int}}$ , where  $R$  is equal to the ohmic resistance (4.10) of  $\Omega_c$ . For the same cylindrical wire segment as considered in (4.18) the internal impedance reads [RWV94, Section 4.5]

$$Z_{\text{int}} = R + j\omega L_{\text{int}} = \frac{j l}{2\pi r} \sqrt{\frac{\omega\mu}{\sigma}} \left( \frac{\operatorname{Ber}(q) + j\operatorname{Bei}(q)}{\operatorname{Ber}'(q) + j\operatorname{Bei}'(q)} \right). \quad (4.19)$$

Here,  $q = r\sqrt{\omega\mu\sigma}$ , and  $\text{Ber}$ ,  $\text{Bei}$ ,  $\text{Ber}'$ , and  $\text{Bei}'$  denote the real and imaginary Kelvin functions and their derivatives, respectively. The total MQS impedance of a straight round wire is thus given with (4.19) and (4.18) as

$$Z = Z_{\text{int}} + j\omega L_{\text{ext}}, \quad (4.20)$$

and provides a reference to verify the numerical impedance computation method developed in Chapter 5.

Fig. 4.2a displays both the total inductance  $L \equiv L_{\text{ext}} + L_{\text{int}} \equiv L_{\text{ext}} + \text{Im}(Z_{\text{int}})/\omega$  and the external inductance  $L_{\text{ext}}$  of a cylindrical wire segment of length  $l = 50$  mm and radius  $r = 1$  mm in the frequency interval  $100 \text{ Hz} \leq f \leq 1 \text{ GHz}$  of the ordinary frequency  $f = \omega/2\pi$ . The contribution of the internal impedance  $L_{\text{int}}$  to  $L$  is small even at low frequencies ( $\approx 6.5\%$  at  $f = 100$  Hz). This indicates that for some applications the external inductance can be useful as an  $f$ -independent approximation of  $L$ . For bulkier conductors, however, this approximation can be insufficient. Fig. 4.2b, shows the ratio of internal and total inductance for a round wire with radius  $r = 1$  mm and variable length  $l$ ,  $1 \text{ mm} \leq l \leq 1 \text{ m}$ , at the DC point  $f = 0$ . At  $l = 1$  mm the internal inductance accounts for 35% of the total inductance.

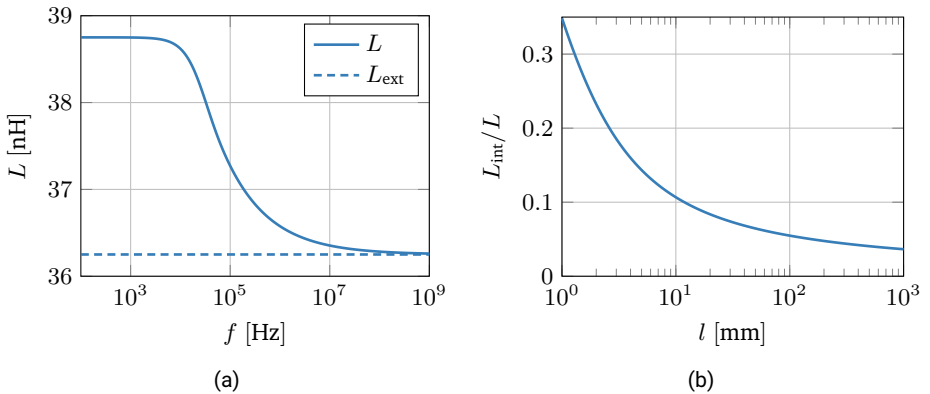


Figure 4.2.: (a) Frequency dependence of total inductance  $L$  and external inductance  $L_{\text{ext}}$  of cylindrical wire segment with length  $l = 50$  mm and radius  $r = 1$  mm. (b) Ratio of internal and total inductance of the same wire but with variable length  $l$  at  $f = 0$ .

### 4.1.3. Capacitance computation

The following capacitance computation method for multi-conductor systems is developed in [Sty+22] and summarized in [SKD22b].

In the ES and EQS approximations discussed in Section (2.5) the right-hand side of Faraday's law (2.11b) vanishes. Thus, the curl of  $\mathbf{E}$  is zero in this case and the electric field can be expressed with the scalar potential as  $\mathbf{E} = -\text{grad } \phi$ . A single charge  $q$  at position  $\mathbf{x}$  can then be understood to hold the potential energy  $W = q\phi(\mathbf{x})$ ; the energy of a charge density  $\rho$  in the domain  $\Omega$  is given by [Jac99, Section 1.11]

$$\begin{aligned} W_E &= \frac{1}{2} \int_{\Omega} \phi \rho \, dV = -\frac{1}{2} \int_{\Omega} \phi \, \text{div}(\varepsilon \, \text{grad } \phi) \, dV \\ &= \frac{1}{2} \int_{\Omega} \varepsilon \, \text{grad } \phi \cdot \text{grad } \phi \, dV - \frac{1}{2} \int_{\partial\Omega} (\varepsilon \, \text{grad } \phi \cdot \hat{\mathbf{n}}) \phi \, dS. \end{aligned} \quad (4.21)$$

Here, the second equality uses Gauss's law (2.11c) and the third equality is obtained through integration by parts. The boundary integral vanishes if  $\partial\Omega$  is charge free or at zero potential, i.e., assuming the MBC (2.23) or EBC (2.19) on  $\partial\Omega$ , respectively. For the capacitance computation method proposed here, the former condition is used. The charges are distributed on a set of  $N$  conductors, that occupy the regions  $\Omega_{c,i}$  with  $\cup_{i=1}^N \Omega_{c,i} \equiv \Omega_c$ . If the system is in a stationary state, the energy is minimized in the conductors by the potential assuming one constant value  $\varphi_i$  per conductor. The energy can then be expressed with only the potential values  $\varphi_i$  and total charge  $q_i$  on the individual conductors

$$W_E = \frac{1}{2} \sum_{i=1}^N \varphi_i \int_{\Omega_{c,i}} \rho \, dV = \frac{1}{2} \sum_{i=1}^N \varphi_i q_i =: \frac{1}{2} \boldsymbol{\varphi} \cdot \mathbf{q}. \quad (4.22)$$

For a given vector of conductor potentials  $\boldsymbol{\varphi}$ , the scalar potential  $\phi$  can be determined in the whole domain  $\Omega$  by solving the electrostatic PDE (2.36) in the non-conducting domain  $\Omega_0 = \Omega \setminus \Omega_c$  in the BVP

$$-\text{div}(\varepsilon \, \text{grad } \phi) = 0 \quad \text{in } \Omega_0, \quad (4.23a)$$

$$\phi = \varphi_i \quad \text{on } \partial\Omega_{c,i}, \quad (4.23b)$$

$$\hat{\mathbf{n}} \cdot \text{grad } \phi = 0 \quad \text{on } \partial\Omega. \quad (4.23c)$$

The solution  $\phi$  does not only give the energy  $W_E$  through (4.21); the fact that the charge density  $\rho$  and thus also the vector of charges  $\mathbf{q}$  are given by  $\phi$  through (2.36) means that  $\mathbf{q}$  depends linearly on the vector of potentials  $\boldsymbol{\varphi}$ , that determines  $\phi$ , i.e.,

$$\mathbf{q} = \mathbf{C}_N \boldsymbol{\varphi}. \quad (4.24)$$

The matrix  $\mathbf{C}_N$  connecting the potential and charge vectors is the capacitance matrix. Its subscript  $N$  indicates that it is a nodal matrix in the graph-theoretical terminology of Section 4.2, understanding each conductor as a node in the network. The graph-theoretical analysis reveals with (4.52b) that between all conductor pairs  $i$  and  $j$  there exists a mutual capacitance  $C_{ij} = -[\mathbf{C}_N]_{ij}$  such that the potential difference  $V_{ij}$  between the two nodes is related to the current  $I_{ij}$  through the branch from  $i$  to  $j$  by

$$I_{ij} = j\omega C_{ij} V_{ij}. \quad (4.25)$$

This means that the relationship (4.24) derived from ES field theory directly corresponds to the circuit relation of (4.2).

The nodal capacitance matrix  $\mathbf{C}_N$  can be computed in the following way: Inserting (4.24) into (4.22) gives

$$W_E = \frac{1}{2} \boldsymbol{\varphi}^T \mathbf{C}_N \boldsymbol{\varphi}. \quad (4.26)$$

This relationship allows to determine the elements of  $\mathbf{C}_N$  by solving the BVP (4.23)  $N$  times, each time setting the potential on one conductor  $i$  to a finite value  $\varphi_0$  and to zero on all other conductors. Denoting the  $N$  solutions by  $\phi_i$  and their corresponding energies by  $W_{E,i}$ , the main-diagonal elements of  $\mathbf{C}_N$  are simply

$$[\mathbf{C}_N]_{ii} = \frac{2W_{E,i}}{\varphi_0^2}. \quad (4.27)$$

Exploiting the linearity of the BVP (4.23), the linear combinations  $\phi_{ij} := \phi_i - \phi_j$  describe the situation that the potential assumes the value  $\varphi_0$  on conductor  $i$  and  $-\varphi_0$  on conductor  $j$ . The off-diagonal elements of  $\mathbf{C}_N$  can thus be computed with the main-diagonal elements and the energies  $W_{E,ij}$  corresponding to  $\phi_{ij}$ ,

$$[\mathbf{C}_N]_{ij} = \frac{W_{E,ij}}{\varphi_0^2} - \frac{1}{2}([\mathbf{C}_N]_{ii} + [\mathbf{C}_N]_{jj}). \quad (4.28)$$

In the case considered here where the outer boundary  $\partial\Omega$  remains charge free and the self-capacitances of the conductors therefore vanish, the desired end result of the extraction is the set of the mutual capacitances

$$C_{ij} \equiv -[\mathbf{C}_N]_{ij} \quad \text{for } i \neq j. \quad (4.29)$$

In the context of parasitic extraction it is typically not possible to treat each conductor as a single node in the electrical network. A complementary resistance or inductance extraction requires two or more nodes per conductor, such that a resistance or inductance between different terminals on the conductor can be defined. In this case, it is necessary to divide the conductors into parts closest to each terminal and treat each segment as a separate conductor in the capacitance extraction. After the extraction, mutual capacitances between two segments of the same conductor are simply disregarded.

#### 4.1.4. Impedance computation

The central objective of this work is to provide a general parasitic extraction method that can capture the parasitic behavior of an interconnect at all frequencies. The discussion on resistance and inductance computation revealed that the resistance  $R$  is in general only the real part of an impedance  $Z$ , and for an impedance computed in the MQS approximation the inductance is just  $L = \text{Im}(Z)/\omega$ . However, since the impedance can describe an arbitrary voltage-current relation in frequency domain, it is suitable to fully characterize the parasitics of a DUT, also considering interactions between inductive and capacitive effects if Darwin's approximation (2.40) is used for its computation, and even considering wave effects if no approximation is applied to Maxwell's equations. The formulation of the BVPs necessary for a general impedance computation are the subject of Chapter 5; the purpose of the discussion here is to show that the impedance can be calculated from the ESP  $\phi$  at arbitrary frequencies where the electric field  $\mathbf{E}$  contains with (2.26) a second component due to the MVP  $\mathbf{A}$ . The following is an expansion of the treatment of one-dimensional conductors developed in [SKD22a].

As discussed in the context of (4.14), in field theory voltage is a path-dependent quantity describing the work per charge necessary to transport charges between two points along a given path. The voltage of electrical networks, however, is path independent at all frequencies, which enables the consideration of individual components without selecting a current path. It is possible to reconcile these two voltage concepts by using the concept of partial inductance introduced in Section 4.1.2. The voltage between the terminals of the one-dimensional loop of Fig. 4.1 is given in (4.14). The inductance  $L$  of the loop can now be split into the total partial inductances of the two paths  $c$  and  $r$ ,

$$L = \frac{1}{I} \oint_l \mathbf{A} \cdot d\mathbf{l} = \frac{1}{I} \int_c \mathbf{A} \cdot d\mathbf{l} + \frac{1}{I} \int_r \mathbf{A} \cdot d\mathbf{l} =: L_c + L_r. \quad (4.30)$$

Subtracting the inductive contribution of the return path  $r$  from (4.14) allows to define a reduced voltage  $V_r$  that contains only the resistive and reactive response along the path  $c$

$$V_r := V - j\omega L_r = \int_c \mathbf{E} \cdot d\mathbf{l} + j\omega \int_c \mathbf{A} \cdot d\mathbf{l}. \quad (4.31)$$

Expressing  $\mathbf{E}$  with the potentials as (2.26),  $V_r$  simplifies to

$$V_r = - \int_c \text{grad } \phi \cdot d\mathbf{l} = \phi(T_b) - \phi(T_a). \quad (4.32)$$

Hence, eliminating the inductive contribution of the return path renders the voltage path independent. In a network simulation, the self-inductance of this return path can be re-introduced into the system as a part of the impedance of the component connected to the terminals  $T_b$  and  $T_a$ , for which  $r$  functions as a place holder.

The voltage definition of (4.31) can not only consider resistive and inductive effects: It still retains its validity if the path  $c$  crosses a capacitor, in which case the capacitive reactance is part of the path integral over  $\mathbf{E}$ . A generalization of the voltage definition of (4.31) to the case of 3D conductors analogously to the voltage (4.17) in inductance computation also remains possible. A generalized current density  $\mathbf{J}_g$  can be defined as the sum of current density  $\mathbf{J}$  and displacement current,

$$\mathbf{J}_g := \mathbf{J} + j\omega\mathbf{D} \equiv \mathbf{J}_s + \sigma\mathbf{E} + j\omega\mathbf{D}. \quad (4.33)$$

Applying the divergence operator to the Ampère-Maxwell law (2.11a) yields  $\text{div } \mathbf{J}_g = 0$ . Therefore, the field lines of  $\mathbf{J}_g$  are closed (and can cross non-conducting regions). Replacing the current density  $\mathbf{J}$  in the voltage definition (4.17), that is a weighted average over the space occupied by  $\mathbf{J}$ , with the generalized current density  $\mathbf{J}_g$  therefore generalizes the 3D voltage definition beyond the MQS approximation, in which  $\mathbf{J}$  must be divergence free. Applying this weighted average to the reduced voltage  $V_r$  of (4.32) and demanding that on the terminals the current is supplied only by the source current density  $\mathbf{J}_s$  yields

$$V_r = \frac{1}{I} \int_{T_b} |\mathbf{J}_s| \phi \, dS - \frac{1}{I} \int_{T_a} |\mathbf{J}_s| \phi \, dS. \quad (4.34)$$

In the case that  $\mathbf{J}_s$  is homogeneously distributed on the terminals used in Chapter 5, the equation simplifies to

$$V_r = \frac{1}{A(T_b)} \int_{T_b} \phi \, dS - \frac{1}{A(T_a)} \int_{T_a} \phi \, dS, \quad (4.35)$$

where  $A(T_a)$  and  $A(T_b)$  denote the surface areas of the two terminal surfaces.

With the voltage  $V_r$  of (4.35) the impedance between the two terminals  $T_a$  and  $T_b$  is, in accordance with (4.4), simply  $Z = V_r/I$ . In the general case, however, there may be several conductors in the DUT that may each host multiple terminals (usually the terminals are defined by where functional components of the device would be connected to the interconnect). For inductance calculation, the terminals are then considered in pairs, which are the *ports* of the system. How these ports should be chosen is discussed in the context of Fig. 5.1. For a system of  $N$  ports, the impedance is a  $N \times N$  matrix  $\mathbf{Z}$ , that can be determined by calculating the ESP  $\phi$   $N$  times, each time with a current  $I_0$  being provided by a source current density  $\mathbf{J}_s$  between the terminals of one of the ports. The element  $[\mathbf{Z}]_{ij}$  of the inductance matrix is then given by

$$[\mathbf{Z}]_{ij} = \frac{V_{r,ij}}{I_0} \equiv \frac{1}{I_0 A(T_{i,2})} \int_{T_{i,2}} \phi_j \, dS - \frac{1}{I_0 A(T_{i,1})} \int_{T_{i,1}} \phi_j \, dS, \quad (4.36)$$

where  $V_{r,ij}$  denotes the voltage that is measured with (4.35) at port  $i$  for a current excitation at port  $j$ . Hence,  $\phi_j$  is the ESP resulting for this current excitation and  $T_{i,1}$  and  $T_{i,2}$  are the two terminal surfaces of port  $i$ .

---

## 4.2. Graph Theory

A formal description of electrical networks is possible with the language of graph theory. Subsection 4.2.1 introduces fundamental concepts of graph theory, that are beyond electrical networks also important in Subsection 6.6.1 for a tree-cotree splitting of the FE mesh. The ensuing discussion of electrical networks in Subsection 4.2.2 allows to understand which sets of ports must be considered in the parasitic extraction of Chapter 5 to characterize an interconnect as an electrical network, and provides the basis for the description of frequency-dependent parasitic elements with standard frequency-independent elements via vector fitting as discussed in Chapter 7.

### 4.2.1. Basic concepts

A graph  $G(N, E)$  consists of a set of vertices  $N = \{n_1, n_2, \dots\}$  and set of edges  $E = \{e_1, e_2, \dots\}$  [Deo74]. Each edge  $e_k$  is identified with a pair of vertices  $(n_i, n_j)$ . These pairs are ordered for *directed graphs* and unordered otherwise. For directed graphs the first vertex of such a pair is the initial vertex of the corresponding edge, from which the edge originates whereas the second one is the edge's terminal vertex. In the description of electrical networks, vertices are referred to as *nodes* and edges as *branches*. The following discussion is restricted to the directed graphs that do not contain self-loops, i.e., the two nodes of an edge cannot be the same.

A walk or chain is a tuple of signed edges  $(\pm e_i, \pm e_k, \pm e_j)$  such that the second vertex of element  $i$  of the walk coincides with the first vertex of element  $i + 1$  (if both elements exist). A minus sign in the tuple indicates that the vertex order of the corresponding edge is reversed. The vertices of a walk's edges constitute the walk's vertex sequence, in which the coinciding vertices of adjacent edges appear only once. A graph  $G$  is connected if for each pair of vertices in  $G$  there exists a path connecting them. A walk is referred to as closed if its first and last vertex coincide. A closed walk in whose vertex sequence no vertex except first and last appears more than once is called a loop or cycle.

A tree is a connected graph that does not contain loops. A graph  $g$  is a subgraph of  $G$  if its vertex and edge sets are subsets of the vertex and edge sets of  $G$  (and the edges in  $g$  and  $G$  are identified with the same vertices). A subgraph of  $G$  that is a tree and contains all vertices of  $G$  is called a spanning tree of  $G$ . Those edges of  $G$  that are not part of the spanning tree  $T$  constitute the cotree of  $T$ . Fig. 4.3 provides an example for a directed graph with a spanning tree and its cotree. If  $G$  has  $n$  vertices and  $e$  edges, any spanning tree  $T$  contains  $n - 1$  edges and its cotree  $e - n + 1$  edges [Deo74, Theorem 3-12]. Adding any single edge of the cotree to the spanning tree closes one loop in the graph, e.g., in Fig. 4.3 the cotree edge  $e_5$  closes the loop  $l_1 = (e_2, e_8, -e_5)$ . These loops created with the cotree edges are the *fundamental loops* of the graph. All other loops in the graph can be expressed as linear combinations of the fundamental loops.

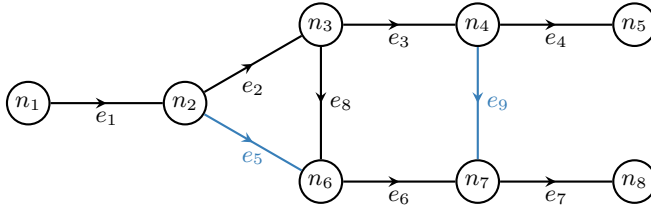


Figure 4.3.: Directed graph with spanning tree (black) and cotree (blue edges).

Graphs can be documented in matrix form with their incidence matrix  $\mathbf{A}$ , which is indispensable for many computations. The rows of  $\mathbf{A}$  correspond to the vertices of the graph and the columns to its edges such that for a directed graph the elements of  $\mathbf{A}$  are defined as

$$[\mathbf{A}]_{ij} = \begin{cases} 1 & \text{if } n_i \text{ is the initial vertex of edge } e_j, \\ -1 & \text{if } n_i \text{ is the terminal vertex of edge } e_j, \\ 0 & \text{otherwise.} \end{cases} \quad (4.37)$$

Since any edge has exactly one initial and terminal vertex, the sum of the row vectors of an incidence matrix is the zero vector. This means that the row vectors are linearly dependent. If the network is a connected graph, this redundancy of information in  $\mathbf{A}$  can be eliminated by deleting one of its rows. The resulting matrix is called a reduced incidence matrix  $\mathbf{A}_r$ . The vertex corresponding to the deleted row is thereby defined as the reference vertex of  $\mathbf{A}_r$ .

The loops of a graph can be organized in the loop matrix  $\mathbf{B}$ . The rows of  $\mathbf{B}$  correspond to the loops and the columns to their edges. Assigning an arbitrary orientation to each loop, the elements of  $\mathbf{B}$  are defined for a directed graph as

$$[\mathbf{B}]_{ij} = \begin{cases} 1 & \text{if loop } l_i \text{ includes edge } e_j \text{ and their orientations coincide,} \\ -1 & \text{if loop } l_i \text{ includes edge } e_j \text{ and their orientations differ,} \\ 0 & \text{otherwise.} \end{cases} \quad (4.38)$$

The row vectors of  $\mathbf{B}$  are linearly dependent if the graph contains more loops than only the fundamental ones. This redundancy can be eliminated by deleting all rows corresponding to non-fundamental loops from  $\mathbf{B}$ , which leaves the fundamental loop matrix  $\mathbf{B}_f$ . The matrix product of loop matrix and transposed incidence matrix is zero

$$\mathbf{B}\mathbf{A}^T = \mathbf{A}\mathbf{B}^T = 0. \quad (4.39)$$

This statement also holds for the fundamental loop matrix  $\mathbf{B}_f$  and reduced incidence matrix  $\mathbf{A}_r$ .

### 4.2.2. Electrical networks as graphs

Electrical networks can be understood as directed graphs whose vertices and edges are called nodes and branches, respectively. Every branch  $e_j$  has two variables assigned to it, a branch voltage  $V_j$  across  $e_j$  and a branch current  $I_j$  through  $e_j$  [Deo74, Chapter 13]. These variables can be related with transfer functions like the impedance matrix  $\mathbf{Z}$  as

$$\mathbf{Z}\mathbf{I} = \mathbf{V}, \quad (4.40)$$

or admittance matrix  $\mathbf{Y} = \mathbf{Z}^{-1}$  as

$$\mathbf{Y}\mathbf{V} = \mathbf{I}, \quad (4.41)$$

where  $\mathbf{V}$  and  $\mathbf{I}$  are the vectors of branch voltages and currents, respectively. The currents  $\mathbf{I}$  obey Kirchhoff's current law, which states that the sum of currents leaving any node must be zero. With the incidence matrix  $\mathbf{A}$  of the network, this law is expressed as

$$\mathbf{A}\mathbf{I} = 0. \quad (4.42)$$

The voltages follow Kirchhoff's voltage law, which demands that the sum of voltages around any loop of the network is zero. With the loop matrix  $\mathbf{B}$ , it reads

$$\mathbf{B}\mathbf{V} = 0. \quad (4.43)$$

The elements of  $\mathbf{V}$  are not linearly independent when related with (4.43); the same is true for  $\mathbf{I}$  and (4.42). It is necessary to reduce  $\mathbf{V}$  and  $\mathbf{I}$  to a set of independent variables both for network simulation, where the network variables  $\mathbf{V}$  and  $\mathbf{I}$  are to be determined for a number of energy sources, and for the computation of transfer functions like  $\mathbf{Z}$  and  $\mathbf{Y}$  in the context of parasitic extraction. This is possible with the nodal approach: The branch voltages can be expressed with a vector of potentials  $\mathbf{V}_N$  on the nodes, using a reduced incidence matrix  $\mathbf{A}_r$ ,

$$\mathbf{V} = \mathbf{A}_r^T \mathbf{V}_N. \quad (4.44)$$

The elements of  $\mathbf{V}_N$  are referred to as node voltages and can be understood as potential differences to the reference node of  $\mathbf{A}_r$ , that is at zero potential. Expressing  $\mathbf{V}$  with (4.44) automatically fulfills Kirchhoff's voltage law (4.43) due to (4.39). Assuming all energy sources are or have been converted to current sources, a node current vector  $\mathbf{I}_N$  can be defined whose  $i$ th element is equal to the sum of currents entering from the sources into node  $n_i$ . With  $\mathbf{I}_N$  and the reduced incidence matrix  $\mathbf{A}_r$ , the linearly independent equations in (4.42) can be expressed as [Deo74]

$$\mathbf{A}_r \mathbf{I} = \mathbf{I}_N. \quad (4.45)$$

Multiplying the admittance equation (4.41) with  $\mathbf{A}_r$ , and using (4.44) and (4.45) to express the branch voltages and currents with their node counterparts gives an equation relating the independent system variables:

$$\mathbf{A}_r \mathbf{Y} \mathbf{A}_r^T \mathbf{V}_N = \mathbf{I}_N \quad \Leftrightarrow \quad \mathbf{Y}_N \mathbf{V}_N = \mathbf{I}_N. \quad (4.46)$$

Here,

$$\mathbf{Y}_N := \mathbf{A}_r \mathbf{Y} \mathbf{A}_r^\top \quad (4.47)$$

is the nodal admittance matrix. Its inverse  $\mathbf{Z}_N = \mathbf{Y}_N^{-1}$  is called nodal impedance matrix. Multiplying (4.40) with  $\mathbf{A}_r^\top$  and using nodal voltages (4.44) and currents (4.45) shows that the branch impedance matrix  $\mathbf{Z}$  of a network can be recovered from  $\mathbf{Z}_N$  with

$$\mathbf{Z} = \mathbf{A}_r^\top \mathbf{Z}_N \mathbf{A}_r. \quad (4.48)$$

In the nodal approach the system can be fully characterized by providing one of the matrices  $\mathbf{Y}_N$  or  $\mathbf{Z}_N$  relating the independent network parameters. There are two possible approaches to obtain the nodal matrices, both of which are used in this work:

1. Extract one of the nodal matrices directly. This can be done for the nodal impedance matrix  $\mathbf{Z}_N$  as described in Section 5.1, which can subsequently be converted into  $\mathbf{Y}_N$  if necessary.
2. Use (4.47) to compute  $\mathbf{Y}_N$  from a branch admittance matrix  $\mathbf{Y}$ . Here  $\mathbf{Y}$  can be constructed from individual scalar admittances of the individual branches or from decoupled admittance matrices describing different subnetworks. This construction approach is significant especially for Chapter 7, and is therefore discussed in the following.

If a electrical network consists of a number  $m \leq e$  of decoupled subnetworks ( $e$  being the number of branches of the network), such that the off-diagonal elements of the branch admittance matrix  $\mathbf{Y}$  belonging to different subnetworks are zero, then  $\mathbf{Y}$  has a block diagonal structure, i.e., it is a direct sum  $\mathbf{Y} = \sum_{i=1}^m \mathbf{Y}_i$ . In this case the nodal admittance matrix (4.47) can be expressed as a sum over the branch admittance matrices  $\mathbf{Y}_i$  of the subnetworks,

$$\mathbf{Y}_N = \sum_{i=1}^m \mathbf{A}_{r,i} \mathbf{Y}_i \mathbf{A}_{r,i}^\top. \quad (4.49)$$

Here  $\mathbf{A}_{r,i}$  denotes the reduced incidence matrix of the  $i$ th subnetwork, which consists of those columns of  $\mathbf{A}_r$  associated with the subnetwork's branches. This split in decoupled subnetworks allows the separate extraction of on the one hand resistive and inductive parasitics with the MQS system of Section 5.2.1 and on the other hand ES parasitic capacitances as described in Subsection 4.1.3. As the MQS approximation precludes capacitive effects and the ES approximation precludes inductive effects and ohmic losses, the branch admittance matrices of these extractions are decoupled and can be considered in the sum

$$\mathbf{Y}_N = \mathbf{A}_{RL} \mathbf{Y}_{RL} \mathbf{A}_{RL}^\top + \mathbf{A}_C \mathbf{Y}_C \mathbf{A}_C^\top, \quad (4.50)$$

where the subscripts  $RL$  and  $C$  denote the matrices of the MQS and ES extractions, respectively. The capacitive branch admittance matrix  $\mathbf{Y}_C$  is simply

$$\mathbf{Y}_C = j\omega\mathbf{C}, \quad (4.51)$$

with  $\mathbf{C}$  being a diagonal matrix of the mutual capacitances  $C_{ij}$  of (4.29).

A second important result can be obtained from (4.49) by assuming that all branches in the network are decoupled (i.e.,  $m = e$ ). In this case, the elements of  $\mathbf{Y}_N$  define scalar branch admittances  $y_i$  between node  $n_i$  and the reference node of  $\mathbf{A}_r$ , and  $y_{ij}$  between the nodes  $n_i$  and  $n_j$  with

$$y_i = \sum_{j=1}^e [\mathbf{Y}_N]_{ij}, \quad (4.52a)$$

$$y_{ij} = -[\mathbf{Y}_N]_{ij} \quad \text{for } i \neq j. \quad (4.52b)$$

The identities of (4.52) show that any nodal admittance matrix can be expressed as a set of decoupled branch admittances. This result also holds for the nodal capacitance matrix  $\mathbf{C}_N$  of Subsection 4.1.3 (in (4.24)  $\boldsymbol{\varphi} \equiv \mathbf{V}_N$  and  $\mathbf{q} \equiv \mathbf{I}_N/j\omega$ ). It is therefore used to relate  $\mathbf{C}_N$  to the mutual capacitances  $C_{ij}$  (cf. [RAJ16, Section 4.2]). Moreover, (4.52) facilitates the expression of pole-residue forms of  $\mathbf{Y}_N$  with frequency-independent network elements, which forms the basis of the consideration of frequency-dependent parasitics in transient network simulations as discussed in Chapter 7.

---

## 5. Finite Element Parasitic Extraction Method

---

This central chapter develops a universal parasitic extraction method based on Maxwell's equations in differential form (2.11). It is thus fit for an implementation with the FEM, whose advantages over integral methods with respect to inhomogeneous materials and flexibility of the spatial discretization have been discussed in Chapter 1. While this chapter derives the method and verifies it with first numerical results, the actual FE discretization is discussed separately in Chapter 6, which treats the mandatory low-frequency stabilization that the method requires. The current chapter is an expansion of the discussion presented in [SKD22a], and goes beyond this original publication with the incorporation of absorbing and asymptotic boundary conditions (ABCs).

The extraction method computes the impedance matrix  $\mathbf{Z}$  as a universal container of parasitic effects, using the impedance computation developed in Subsection 4.1.4. For the general method based on Maxwell's equations without approximation discussed in the following section, as well as for the Darwin approximation treated in Subsection 5.2.2, the nodal impedance matrix  $\mathbf{Z}_N$  is computed, fully characterizing the resistive, inductive, and capacitive parasitics of the DUT. In contrast, the MQS approach of Subsection 5.2.1 directly computes the resistance and inductance matrices  $\mathbf{R}$  and  $\mathbf{L}$  from a branch impedance matrix  $\mathbf{Z}$ , neglecting capacitive effects.

### 5.1. General Method

#### 5.1.1. Device model, boundary conditions, and extraction topology

Before the parasitic extraction method is developed in the following subsections, its two required inputs, the DUT model (including boundary conditions) and the extraction topology, are briefly discussed.

The CAD model of the DUT must provide the electric conductivity  $\sigma$ , as well as the electric permittivity  $\varepsilon$  and magnetic permeability  $\mu$  in the computational domain  $\Omega$ . The FEM requires a spatial discretization of not only the structures of the DUT but also the free space surrounding it (vacuum or air, i.e., regions where  $\sigma = 0$ ,  $\varepsilon \approx \varepsilon_0$ , and  $\mu \approx \mu_0$ .) Therefore,  $\Omega$  must be finite and its boundary  $\partial\Omega$  at a finite distance to the DUT.

In order to transform the electromagnetic PDEs into solvable BVPs, boundary conditions (BCs) must be selected for  $\partial\Omega$ . The two simplest forms of BCs are homogeneous Dirichlet

and Neumann BCs, which in the case of the electric field  $\mathbf{E}$  are given with the EBC (2.19) and MBC (2.21), respectively. Whereas electric boundaries can be used to model a device above a conducting ground plane or inside a conducting casing, for most applications the DUT is to be considered in free space. In this standard case, applying EBCs or MBCs at a finite distance leads to an unwanted influence of the boundary in the field solutions. While this influence can be minimized in the quasistatic approximations by increasing the distance between DUT and boundary, in the full-wave case this strategy cannot be successful since wave solutions are reflected at the boundary independently of its distance from the DUT [SKD22a]. Moreover, moving the boundary further away also increases the number of mesh cells necessary and hence also the computational cost.

A relatively simple approach improving upon the electric and magnetic boundary conditions is to approximate the field that would occur at the position of the finite boundary if the domain were infinite, and use this approximation to provide a BC. In the MQS approximation such a BC is given with the asymptotic BC [Bra+91], whereas for the case of Maxwell's equations without approximation a special absorbing BC is used that can be understood as a combination of the asymptotic BC and the lowest order of the classical absorbing BC of [Pet88]. The derivation and discussion of these ABCs in the context of the presented parasitic extraction method is deferred to Section A.1 of the appendix in order to not interrupt the derivation of the method itself. There, the choice of the ABC approach over potentially more powerful alternatives is motivated and its limitations are examined. For the derivation of the parasitic extraction method it is assumed that the boundary of the computational domain is the unity

$$\partial\Omega = \Gamma_{\text{el}} \cup \Gamma_{\text{mag}} \cup \Gamma_{\text{a}}, \quad (5.1)$$

where  $\Gamma_{\text{el}}$  denotes an electric boundary on which the EBC is applied,  $\Gamma_{\text{mag}}$  a magnetic boundary on which the MBC holds, and  $\Gamma_{\text{a}}$  a boundary on which the absorbing BC is required for PDEs that support wave solutions and the asymptotic BC otherwise. While this representation of  $\partial\Omega$  allows for a concise and general formulation of the BVPs, in the numerical examples considered typically two of the three subsets of  $\partial\Omega$  are chosen empty, such that one BC is applied to the entirety of  $\partial\Omega$ .

The second required input of the method is an extraction topology, which consists of the placement of terminals on the conductors and the pairing of these terminals to ports (a terminal may be part of multiple ports). The terminals are nodes in the electrical network, and considered as surfaces in the 3D simulation through which the current excitation of the system is provided and on which the voltage is measured with (4.35). Since the voltage measurement uses the values of the ESP  $\phi$  on the terminals, these values must be determined in simulation and cannot be provided or constrained by a boundary condition. Therefore, the terminal surfaces must lie within the computational domain  $\Omega$  and cannot be part of its boundary  $\partial\Omega$ . The two kinds of extraction topologies relevant in this work are illustrated in Fig. 5.1. The figure shows five terminals distributed on two separate

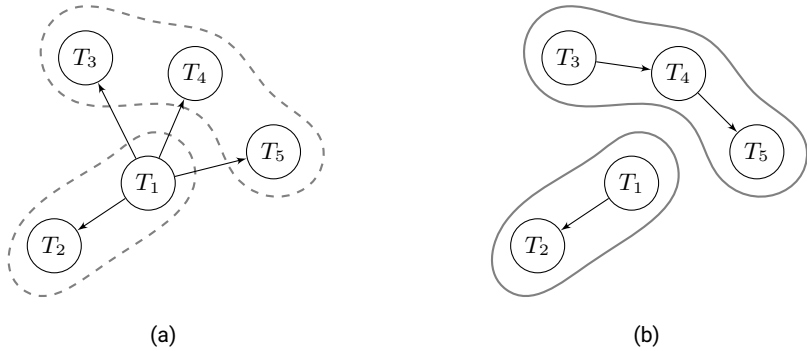


Figure 5.1.: [SKD22b] Abstract illustration of two conductors hosting five terminals  $T_i$  with different extraction topologies. (a) Star topology for the extraction of the nodal impedance matrix  $\mathbf{Z}_N$ . (b) Conductive topology for the extraction of the resistance and inductance matrices  $\mathbf{R}$  and  $\mathbf{L}$ .

conductors. In a star topology a reference or ground terminal is defined ( $T_1$  in Fig. 5.1a) and ports connecting the reference to all other terminals are added to the topology. Using this topology to compute the impedance matrix with (4.36) gives the nodal impedance matrix  $\mathbf{Z}_N$  with respect to the reference terminal, which constitutes a complete description of the system. In contrast, the MQS approximation only considers resistive and inductive effects, and can in the absence of the displacement current only be applied to ports whose terminals lie on the same conductor. This situation is given in the conductive topology of Fig. 5.1b.

### 5.1.2. Formulation of the fundamental differential equations

The impedance matrix  $\mathbf{Z}$  is calculated from the ESP  $\phi$  with (4.36). For a system excited by a given source current density  $\mathbf{J}_s$ , two possible strategies to calculate  $\phi$  are available: The first option is to solve Maxwell's equations directly in the potential formulation (2.27) for the ESP  $\phi$  and the MVP  $\mathbf{A}$ . However, if the current density  $\mathbf{J}$  also contains a conduction current density contribution  $\mathbf{J}_c = \sigma \mathbf{E}$  due to Ohm's law (2.16), the two equations of the potential formulation cannot be decoupled anymore by using the gauge conditions of (2.33) or (2.34). A computationally cheaper alternative to solving the coupled system of (2.27) is found with the *E-field formulation*. In this formulation all fields except the source current density  $\mathbf{J}_s$  are expressed with the electric field strength  $\mathbf{E}$  such that only one vector field needs to be determined in simulation, which makes it a popular choice when solving the frequency-domain Maxwell equations [Mon03]. It is derived by multiplying the Ampère-

Maxwell law (2.11a) with the factor  $-j\omega$ , and using the constitutive relations (2.14), Ohms law (2.16), and Faraday's law (2.11b) to express the fields with  $\mathbf{E}$ . This yields

$$\text{curl}(\nu \text{curl} \mathbf{E}) + j\omega\sigma\mathbf{E} - \omega^2\varepsilon\mathbf{E} = -j\omega\mathbf{J}_s. \quad (5.2)$$

The ESP  $\phi$  can be recovered from a solution  $\mathbf{E}$  using (2.26) and a gauge condition.

This second approach utilizing the E-field form is the one perused in the following, not only because the two fields  $\mathbf{E}$  and  $\phi$  can be calculated in sequence (except in the Darwin approximation discussed in Subsection 5.2.2), thereby avoiding a computationally more expensive coupled boundary value problem (BVP); moreover, the approach allows for an easy treatment of the useful perfect electric conductor case discussed in Section 5.3. Finally, the use of the E-field form facilitates the direct application of the low-frequency stable discretization scheme of [Ell+17], which is the subject of Chapter 6.

The full BVP to compute  $\mathbf{E}$  from  $\mathbf{J}_s$  is found by augmenting (5.2) with the EBC (2.19), MBC (2.21), and ABC (A.10):

$$\text{curl}(\nu_r \text{curl} \mathbf{E}) + j\omega\mu_0\sigma\mathbf{E} - \frac{\omega^2}{c^2}\varepsilon_r\mathbf{E} = -j\omega\mu_0\mathbf{J}_s \quad \text{in } \Omega, \quad (5.3a)$$

$$\hat{\mathbf{n}} \times \mathbf{E} = 0 \quad \text{on } \Gamma_{\text{el}}, \quad (5.3b)$$

$$\hat{\mathbf{n}} \times \nu_r \text{curl} \mathbf{E} = 0 \quad \text{on } \Gamma_{\text{mag}}, \quad (5.3c)$$

$$\hat{\mathbf{n}} \times \text{curl} \mathbf{E} = \alpha\mathbf{E}_t \quad \text{on } \Gamma_a. \quad (5.3d)$$

Here,  $\alpha := j\omega/c + 1/r$  with  $r$  being the radial coordinate, which is constant on  $\Gamma_a$  using a spherical boundary as discussed in Section A.1. Further,  $\mathbf{E}_t := (\hat{\mathbf{n}} \times \mathbf{E}) \times \hat{\mathbf{n}}$  denotes the tangential component of  $\mathbf{E}$  on the boundary. The relative reluctivity  $\nu_r$  and relative permittivity  $\varepsilon_r$  are used here to improve the numeric properties of the BVP.

The PDE to determine  $\phi$  is found by using (2.26) to eliminate the MVP  $\mathbf{A}$  from a gauge condition. The simplest result is produced with the Coulomb gauge (2.33),

$$-\text{div}(\varepsilon_r \text{grad} \phi) = \text{div}(\varepsilon_r \mathbf{E}). \quad (5.4)$$

The Lorenz gauge (2.34) can also be used to derive a suitable PDE for  $\phi$ ,

$$-\text{div}(\varepsilon_r \text{grad} \phi) - \frac{\omega^2}{c^2}\phi = \text{div}(\varepsilon_r \mathbf{E}). \quad (5.5)$$

This Lorenz-gauged PDE used in [SKD22a] is mainly relevant for the Darwin approximation where it provides an increased stability for magnetic boundaries,  $\partial\Omega = \Gamma_{\text{mag}}$ , as discussed in Subsection 5.2.2. In all other cases impedance results computed with (5.4) and (5.5) exhibit only insubstantial differences.

While the full BVP to compute the ESP  $\phi$  is given in Subsection 5.1.4 after modeling the source current density  $\mathbf{J}_s$  and introducing a necessary compensation term, the boundary

conditions for  $\phi$  are already discussed here. The EBC (2.19) demands a vanishing tangential component of  $\mathbf{E}$  on  $\Gamma_{\text{el}}$ . With the potential expression (2.26) of  $\mathbf{E}$  this condition is fulfilled if the tangential components of both the MVP  $\mathbf{A}$  and  $\text{grad } \phi$  vanish on  $\Gamma_{\text{el}}$ . For this to hold the ESP  $\phi$  must be constant on the boundary. If there is only one connected electric boundary  $\Gamma_{\text{el}}$ , only a single constant value is needed which can simply be chosen as zero, yielding a homogeneous Dirichlet boundary condition for  $\phi$ ,

$$\phi = 0 \quad \text{on } \Gamma_{\text{el}}. \quad (5.6)$$

An MBC applicable to  $\phi$  can be derived from the MBC (2.23):

$$\hat{\mathbf{n}} \cdot \varepsilon_r \text{grad } \phi = 0 \quad \text{on } \Gamma_{\text{mag}}. \quad (5.7)$$

This MBC adopts the prerequisite

$$\hat{\mathbf{n}} \cdot \mathbf{J} = 0 \quad \text{on } \Gamma_{\text{mag}}. \quad (5.8)$$

from (2.23). On the boundary  $\Gamma_a$  the ESP  $\phi$  of the Coulomb-gauged PDE (5.4) must fulfill the scalar asymptotic BC (A.6), whereas the ESP of the Lorenz-gauged PDE (5.5) requires the scalar absorbing BC (A.11) due to its wave term.

### 5.1.3. Modeling the connecting source current density

The remaining task is to identify a suitable source current density  $\mathbf{J}_s$  modeling a current source connected to the two terminals of one port of the model. The source current density  $\mathbf{J}_s$  must inject a current  $I_0$  at the terminal surface  $T_b$  and extract the same current again at  $T_a$ , such that this current flows inside the device. There, the current  $I_0$  is transported between the terminals by the conduction current density  $\mathbf{J}_c$  (and in a capacitive setting also partly by the displacement current  $j\omega\mathbf{D}$ ), which unlike  $\mathbf{J}_s$  directly couples to  $\mathbf{E}$  via Ohm's law (2.16) and thereby captures the resistive response to the enforced current flow. It is necessary to choose how the current source distributes the supplied current on the terminals surfaces. With the objective of developing a general method applicable to any geometry and in the absence of additional information on, e.g., the importance of the skin effect, homogeneous distributions are chosen as a default for the current densities  $\mathbf{J}_a$  and  $\mathbf{J}_b$  on the terminal surfaces,

$$\mathbf{J}_a = \hat{\mathbf{n}}_a \frac{I_0}{A(T_a)} \quad \text{and} \quad \mathbf{J}_b = -\hat{\mathbf{n}}_b \frac{I_0}{A(T_b)}, \quad (5.9)$$

with  $\hat{\mathbf{n}}_i$  denoting the unit normal vector pointing out of the conductor, and  $A(T_i)$  again the area of the respective terminals. However, non-homogeneous choices are possible for specific problems. The expression (5.9) dictates the associated divergence of  $\mathbf{J}_s$  on the terminals,

$$\text{div } \mathbf{J}_s = -\text{div } \mathbf{J}_c = |\mathbf{J}_a| \delta_a(\mathbf{r}) - |\mathbf{J}_b| \delta_b(\mathbf{r}) \quad (5.10)$$

where the delta distribution  $\delta_i(\mathbf{r})$  on terminal  $T_i$  is defined by

$$\int_{\Omega} \delta_i(\mathbf{r}) f(\mathbf{r}) dV = \int_{T_i} f(\mathbf{r}) dS \quad \forall f(\mathbf{r}) : \Omega \rightarrow \mathbb{C}. \quad (5.11)$$

Equation (5.10) describes the situation that on the terminal surface the source current density  $\mathbf{J}_s$  takes over the task of transporting the current  $I_0$  from the conduction current density  $\mathbf{J}_c$ .

In order to derive an universal parasitic extraction method, a strategy to calculate  $\mathbf{J}_s$  has to be found that can automatically produce a connecting  $\mathbf{J}_s$  independently of how the terminal surfaces are positioned in relation to, e.g., the boundary  $\partial\Omega$  or any of the conducting areas of the DUT. Generally, an expression for the divergence of the vector field  $\mathbf{J}_s$  is not sufficient to determine  $\mathbf{J}_s$ . However, choosing a gradient field ansatz,

$$\mathbf{J}_s = -\tilde{\sigma} \text{grad } \xi, \quad (5.12)$$

enables a computation of  $\mathbf{J}_s$  from its divergence given in (5.10) without further specifying the path of the source current. The fictitious conductivity  $\tilde{\sigma}$  is a parameter of the algorithm and is here chosen to be constant in the whole domain  $\Omega$ . The PDE determining the underlying potential  $\xi$  (and therefore  $\mathbf{J}_s$ ) is equivalent to the PDE of the standard stationary current problem,

$$-\text{div}(\tilde{\sigma} \text{grad } \xi) = \text{div } \mathbf{J}_s. \quad (5.13)$$

A BVP using this PDE is provided after the discussion the inductive influence of  $\mathbf{J}_s$  in the following subsection.

#### 5.1.4. Compensating the inductive influence of the source current density

The gradient-field source current density (5.12) does not model an ideal current source in one respect: Ideal current sources should not influence the DUT inductively. In the reduced voltage  $V_r$  of (4.35) the voltage contribution of the total partial inductance of the return path  $r$  (i.e., the source current) is eliminated. However, to fully remove the inductive influence of the source current density from the impedance result, also those contributions to  $V_r$  have to be eliminated that are due to the mutual partial inductances  $L_{p,i,j}$  whose generating current  $I_j$  is located in  $r$ . The electric field calculated with (5.3) includes this unwanted influence of the source current since any source current density that has a component parallel to the DUT at a finite distance is expected to have a direct inductive influence on the fields in the DUT (such parallel components are unavoidable for three-dimensional conductors of arbitrary shape). It is, however, possible to quantify and eliminate (and thereby de-embed) the contribution of this unwanted direct influence of the source current density in the calculation of the scalar potential with (5.4) or (5.5). The de-embedding technique developed in the following is a generalization of the approach

that was presented in [Tra+12; Tra14] for the Darwin approximation in the PEC case (cf. Subsection 5.3.2) with homogeneous material parameters  $\varepsilon$  and  $\mu$ .

The “total” electric field  $\mathbf{E}$  of (5.2), incorporating inductive effects related to both the conduction currents and the source current, is expressed as the difference of the compensated field  $\mathbf{E}_c$  capturing only the influence of the conductors and the field  $\mathbf{E}_s$  capturing the counteractive inductive influence of the source current density,

$$\mathbf{E} = \mathbf{E}_c - \mathbf{E}_s. \quad (5.14)$$

The scalar potential to be calculated with (5.4) for use in the impedance calculation is the compensated potential  $\phi_c$  excluding the unwanted inductive influence of  $\mathbf{J}_s$ ,

$$-\operatorname{div}(\varepsilon_r \operatorname{grad} \phi_c) = \operatorname{div}(\varepsilon_r \mathbf{E}_c) = \operatorname{div}(\varepsilon_r \mathbf{E}) + \operatorname{div}(\varepsilon_r \mathbf{E}_s). \quad (5.15)$$

The compensation term  $\operatorname{div} \varepsilon_r \mathbf{E}_s$  can be determined employing the potential formulation of Maxwell’s equations (2.27) in Lorenz gauge (2.34),

$$\operatorname{curl}(\nu_r \operatorname{curl} \mathbf{A}) - \varepsilon_r \operatorname{grad} \operatorname{div}(\varepsilon_r \mathbf{A}) - \frac{\omega^2}{c^2} \varepsilon_r \mathbf{A} = \mu_0 \mathbf{J}, \quad (5.16a)$$

$$-\operatorname{div}(\varepsilon_r \operatorname{grad} \phi) - \frac{\omega^2}{c^2} \phi = \frac{1}{\varepsilon_0} \rho. \quad (5.16b)$$

This formulation of Maxwell’s equations enables the independent calculation of the vector potential  $\mathbf{A}$  from the current density  $\mathbf{J}$  and the scalar potential  $\phi$  from the charge density  $\rho$  in the case that all currents in a given system are source currents,  $\mathbf{J} = \mathbf{J}_s$ , that do not couple to the electric field via Ohm’s law.

To calculate  $\operatorname{div}(\varepsilon_r \mathbf{E}_s)$ , the non-physical (since not charge conserving) situation  $\mathbf{J} = \mathbf{J}_s$  and  $\rho = 0$  is considered. Here, the conducting structures of the DUT are not modeled as the conduction current density  $\mathbf{J}_c$  is disregarded. The correction term calculated from these sources therefore captures the isolated effects of the source current density  $\mathbf{J}_s$ . By only considering source currents and no source charges, the “source” scalar potential  $\phi_s$  associated with  $\mathbf{E}_s$  vanishes and the correction term only depends on the “source” vector potential  $\mathbf{A}_s$ ,

$$\operatorname{div}(\varepsilon_r \mathbf{E}_s) = -j\omega \operatorname{div}(\varepsilon_r \mathbf{A}_s). \quad (5.17)$$

A PDE to calculate the scalar field  $\operatorname{div} \varepsilon_r \mathbf{A}_s$  directly is found by applying the divergence operator to (5.16a). In the resulting equation the  $\omega$ -dependent term is neglected to fully isolate the inductive contribution of the frequency-independent source current density by precluding wave propagation (i.e., Darwin’s approximation (2.40)). This yields

$$-\operatorname{div}(\varepsilon_r \operatorname{grad} \operatorname{div}(\varepsilon_r \mathbf{A}_s)) = \mu_0 \operatorname{div} \mathbf{J}_s. \quad (5.18)$$

The source term  $\text{div } \mathbf{J}_s$  is given with (5.10). To simplify the notation in the following, the scalar field

$$g := -\frac{1}{\mu_0} \text{div}(\varepsilon_r \mathbf{A}_s) \quad (5.19)$$

is defined. Expressing (5.18) with  $g$  and supplying BCs yields the BVP

$$-\text{div}(\varepsilon_r \text{grad } g) = -\text{div } \mathbf{J}_s \quad \text{in } \Omega, \quad (5.20a)$$

$$g = 0 \quad \text{on } \Gamma_{\text{el}} \cup \Gamma_a, \quad (5.20b)$$

$$\hat{\mathbf{n}} \cdot \varepsilon_r \text{grad } g = 0 \quad \text{on } \Gamma_{\text{mag}}. \quad (5.20c)$$

The homogeneous Dirichlet BC on  $\Gamma_a$  is motivated in Section A.1. On  $\Gamma_{\text{el}}$  and  $\Gamma_{\text{mag}}$  the BCs are chosen equivalently to those of  $\phi$  provided in (5.6) and (5.7), respectively. While this choice suggests itself due the close relationship of  $g$  and  $\phi$  established by the Lorenz gauge (2.34), for  $\Gamma_{\text{mag}}$  it is required due to a second function that the scalar field  $g$  fulfills beyond providing the inductive compensation term: A comparison of (5.20a) with the PDE (5.13) of the potential  $\xi$  of the source current density  $\mathbf{J}_s$  shows that  $g$  can be used to express  $\mathbf{J}_s$ ,

$$\mathbf{J}_s = -\tilde{\sigma} \text{grad } \xi = \varepsilon_r \text{grad } g. \quad (5.21)$$

It is hence sufficient to solve (5.20) to produce both the source current density  $\mathbf{J}_s$  and its associated inductive compensation term. The prerequisite (5.8) of the MBCs (2.23) and (5.7) requires that the normal component of  $\mathbf{J}$  vanishes on  $\Gamma_{\text{mag}}$ , which is fulfilled through (5.20c) for the  $\mathbf{J}_s$  of (5.21). In case of a purely magnetic boundary,  $\partial\Omega = \Gamma_{\text{mag}}$ , the BVP (5.20) does not determine the spatially constant component of  $g$ . While this component does not influence  $\mathbf{J}_s$  in (5.21), it is relevant for the more direct use of  $g$  as  $\text{div } \mathbf{E}_s$  in (5.17). In order to obtain plausible impedance results, the constant component of  $g$  must be chosen such that  $g$  vanishes at equal distance to both terminals.

Using the definition of  $g$  in (5.15) and supplementing the BCs (5.6), (5.7), and (A.6), yields the BVP determining the compensated scalar potential  $\phi_c$ ,

$$-\text{div}(\varepsilon_r \text{grad } \phi_c) = \text{div}(\varepsilon_r \mathbf{E}) + j\omega\mu_0 g \quad \text{in } \Omega, \quad (5.22a)$$

$$\phi_c = 0 \quad \text{on } \Gamma_{\text{el}}, \quad (5.22b)$$

$$\hat{\mathbf{n}} \cdot \varepsilon_r \text{grad } \phi_c = 0 \quad \text{on } \Gamma_{\text{mag}}, \quad (5.22c)$$

$$\hat{\mathbf{n}} \cdot \text{grad } \phi_c = -(2/r)\phi \quad \text{on } \Gamma_a. \quad (5.22d)$$

The PDE (5.22a) can if necessary (as for the Darwin approximation of Section 5.2.2) be replaced with the Lorenz-gauged alternative

$$-\text{div}(\varepsilon_r \text{grad } \phi_c) - \frac{\omega^2}{c^2} \phi_c = \text{div}(\varepsilon_r \mathbf{E}) + j\omega\mu_0 g. \quad (5.23)$$

Due to its wave term, this PDE requires on the ABC boundary  $\Gamma_a$  the scalar absorbing BC (A.11) instead of the asymptotic BC (A.6).

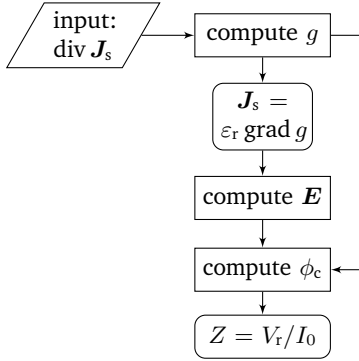


Figure 5.2.: Flowchart connecting the individual steps of the derived impedance computation method. The reduced voltage  $V_r$  used in the final step is computed from  $\phi_c$  with (4.35).

This concludes the derivation of the field theoretical model. There are in total four steps in the impedance calculation, including the solution of three BVPs:

1. Compute  $g$  from the  $\text{div } \mathbf{J}_s$  expression of (5.10) using (5.20).
2. Compute  $\mathbf{E}$  from  $\mathbf{J}_s = \epsilon_r \text{grad } g$  using (5.3).
3. Compute  $\phi_c$  from  $\mathbf{E}$  and  $g$  using (5.22).
4. Compute  $\mathbf{Z}$  from  $\phi_c$  using (4.36).

This procedure is illustrated in Fig 5.2.

Usually the impedance matrix  $\mathbf{Z}$  is determined in a frequency sweep for several frequency points in a given interval. Whereas the BVP (5.3) determining  $\mathbf{E}$  is frequency dependent and requires a solution at each frequency point, the frequency-independent BVP (5.20) determining  $g$  needs only to be solved once per model. Moreover, using a direct solver for the linear equation systems resulting from a FE discretization of the BVPs (which is already necessary due to the fact that for multi-port systems multiple right-hand sides have to be considered), the frequency-independent system matrix of the BVP (5.22) determining  $\phi_c$  needs to be factorized only once.

## 5.2. Quasistatic Approximations

Two of the quasistatic approximations introduced in Section 2.5 are useful in the context of parasitic extraction: The MQS approximation neglecting capacitive and wave effects enables a direct computation of the resistance and inductance matrices  $\mathbf{R}$  and  $\mathbf{L}$ . The elements of these matrices can be identified with individual conductors or conductor segments,

increasing the interpretability of the extracted parasitics. The MQS results can be combined with ES capacitances due to (4.50), which constitutes the foundation of the sensitivity analysis of Chapter 8 and the stable export of frequency-dependent parasitics discussed in Section 7.2. Moreover, the MQS problem has a lower computational cost than the full-wave BVP (5.3) due to the lack of a gradient field component of  $\mathbf{E}$  in the non-conducting domain, as discussed in Subsection 6.4.1.

In addition to the very useful MQS approximation, also Darwin's approximation is considered, which only neglects wave effects, while still considering capacitive effects. This allows to compute a complete nodal impedance matrix  $\mathbf{Z}_N$  without having to rely on an absorbing BC to treat reflections occurring at the boundary of the domain. In the PEC case discussed in Section 5.3, the Darwin approximation enables the extraction of *non-static capacitances*, as well as an eigenmode computation in a generalized eigenvalue problem.

### 5.2.1. Magnetoquasistatic approximation

The parasitic extraction in the MQS approximation follows the same steps derived for the full-wave case in the previous section and summarized in Fig. 5.2; the only exceptions being that in the computation of  $\mathbf{E}$  the displacement current  $j\omega\varepsilon\mathbf{E}$  is neglected (as in (2.39a)), and that on  $\Gamma_a$  the asymptotic BC (A.4) holds instead of the absorbing BC (A.10). The BVP to determine  $\mathbf{E}$  in the MQS approximation is hence given by

$$\operatorname{curl}(\nu_r \operatorname{curl} \mathbf{E}) + j\omega\mu_0\sigma\mathbf{E} = -j\omega\mu_0\varepsilon_r \operatorname{grad} g \quad \text{in } \Omega, \quad (5.24a)$$

$$\hat{\mathbf{n}} \times \mathbf{E} = 0 \quad \text{on } \Gamma_{\text{el}}, \quad (5.24b)$$

$$\hat{\mathbf{n}} \times \nu_r \operatorname{curl} \mathbf{E} = 0 \quad \text{on } \Gamma_{\text{mag}}, \quad (5.24c)$$

$$\hat{\mathbf{n}} \times \operatorname{curl} \mathbf{E} = \frac{1}{r} \mathbf{E}_t \quad \text{on } \Gamma_a. \quad (5.24d)$$

In the absence of capacitive effects, a conductive extraction topology as exemplified in Fig. 5.1b must be chosen, and the resistance and inductance matrices can be recovered from the computed branch impedance matrix  $\mathbf{Z}$  with  $\mathbf{R} = \operatorname{Re}(\mathbf{Z})$  and  $\mathbf{L} = \operatorname{Im}(\mathbf{Z})/\omega$ , respectively.

### 5.2.2. Darwin approximation

As discussed in the context of (2.40), in the Darwin approximation the MVP contribution to the displacement current is neglected, which leads to the ESP  $\phi$  appearing explicitly as an unknown in the E-field formulation. To also determine this additional unknown, an additional scalar PDE is needed. As the QoI of the simulation is the compensated scalar potential  $\phi_c$ , the ESP considered in the displacement current is chosen to be  $\phi_c$  and the required scalar PDE is found with the Lorenz-gauged equation (5.23) for  $\phi_c$ . This gives a

coupled BVP for  $\mathbf{E}$  and  $\phi_c$ :

$$\text{curl}(\nu_r \text{curl } \mathbf{E}) + j\omega\mu_0\sigma\mathbf{E} + \frac{\omega^2}{c^2}\varepsilon_r \text{grad } \phi_c = -j\omega\mu_0\varepsilon_r \text{grad } g \quad \text{in } \Omega, \quad (5.25a)$$

$$-\text{div}(\varepsilon_r \mathbf{E}) - \text{div}(\varepsilon_r \text{grad } \phi_c) - \frac{\omega^2}{c^2}\phi_c = j\omega\mu_0 g \quad \text{in } \Omega, \quad (5.25b)$$

$$\hat{\mathbf{n}} \times \mathbf{E} = 0 \quad \text{and} \quad \phi_c = 0 \quad \text{on } \Gamma_{\text{el}}, \quad (5.25c)$$

$$\hat{\mathbf{n}} \times \nu_r \text{curl } \mathbf{E} = 0, \quad \hat{\mathbf{n}} \cdot \varepsilon_r \mathbf{E} = 0 \quad \text{and} \quad \hat{\mathbf{n}} \cdot \varepsilon_r \text{grad } \phi_c = 0 \quad \text{on } \Gamma_{\text{mag}}. \quad (5.25d)$$

No ABCs are available in the Darwin approximation, as they require the PDEs to simplify to a Helmholtz or Laplace equation in free space. Solving this coupled BVP has a higher computational cost than computing  $\mathbf{E}$  and  $\phi_c$  in the full-wave case.

In the formulation of (5.25), the Lorenz-gauged equation (5.23) is preferred over the Coulomb-gauged equation (5.22a) because it increases the stability of the BVP in the case of a magnetic boundary,  $\partial\Omega = \Gamma_{\text{mag}}$ . As stated in Subsection 5.1.4, in order to obtain plausible results in the Coulomb gauge,  $g$  must vanish at equal distance to both terminals. For the full-wave case and the MQS approximation, it is sufficient if this condition is fulfilled approximately, which can be achieved by setting  $g$  to zero on one mesh node  $\in \partial\Omega$  that has approximately equal distance to both of the terminals where  $\text{div } \mathbf{J}_s \neq 0$ . The Darwin BVP (5.25) remains unstable if the condition is fulfilled only approximately. This issue does not occur, however, if the Lorenz-gauged equation (5.23) is used, which features an additional “mass term” proportional to  $\phi_c$ , that increases the BVP’s stability. Whereas for the full-wave and MQS systems adding this the frequency-dependent mass term would render the BVP (5.22) determining  $\phi_c$  frequency dependent and thereby increase its computational cost, the cost of the coupled Darwin BVP (5.25) is not impacted by the term.

### 5.3. Perfect Electric Conductor Case

For some applications of EMC analysis the resistance  $\mathbf{R}$  is of only minor importance, and it suffices to quantify the inductive and capacitive responses of the DUT. In this case a convenient simplification reducing the numerical cost is to model the conductors of the DUT as perfect electric conductors (PECs), i.e., setting their resistivity to zero,  $1/\sigma = 0$ . This enforces a fully developed skin effect in the conductors such that the electric field  $\mathbf{E}$  vanishes in the conducting domains. The computational cost of this approach is lower than for the general case for two reasons: First, in the PEC case (5.3a) is enforced only in the nonconducting subdomain  $\Omega_0 = \Omega \setminus \Omega_c$ . Supplementing the PDE with electric boundary conditions for  $\mathbf{E}$  on the boundary of the conducting subdomain  $\Omega_c$ , only  $\Omega_0$  must be discretized with the  $H(\text{curl})$ -conforming finite elements used to express  $\mathbf{E}$ . Second, the ohmic loss term  $j\omega\sigma\mathbf{E}$  disappears from the E-field form, such that the system of equations only needs to be solved for the imaginary part of the fields  $\mathbf{E}$  and  $\phi_c$ , since  $\text{Re}(\mathbf{E}) = 0$

and  $\text{Re}(\phi_c) = 0$  if  $\mathbf{J}_s$  is chosen real. This leads to real-valued operator matrices after FE discretization. Applying the PEC approach to the full-wave BVP (5.3) yields

$$\text{curl}(\nu_r \text{curl } \mathbf{E}) - \frac{\omega^2}{c^2} \varepsilon_r \mathbf{E} = -j\omega\mu_0 \mathbf{J}_s \quad \text{in } \Omega_0, \quad (5.26a)$$

$$\hat{\mathbf{n}} \times \mathbf{E} = 0 \quad \text{on } \partial\Omega_c \cup \Gamma_{\text{el}}, \quad (5.26b)$$

$$\hat{\mathbf{n}} \times \nu_r \text{curl } \mathbf{E} = 0 \quad \text{on } \Gamma_{\text{mag}}. \quad (5.26c)$$

No absorbing BC is provided in the PEC case as it would conflict with the goal of producing real-valued system matrices. The BVP (5.22) determining  $\phi_c$  remains unchanged. Its PDE must be enforced in the whole domain  $\Omega$  without requiring an EBC on  $\partial\Omega_c$  because otherwise no potential difference is possible between two terminals on the same conductor.

The PEC approach is especially useful in combination with the quasistatic approximations discussed in the previous section: Applied together with the MQS approximation, it provides a frequency-independent way to compute the external inductance  $\mathbf{L}_{\text{ext}}$  directly, as detailed in the following subsection. The Darwin approximation in the PEC case, the topic of Subsection 5.3.2, enables an eigenmode computation in a generalized eigenvalue problem and provides the basis for the extraction of additional non-static capacitances that can supplement the electrostatic capacitances of Section 4.1.3 for some models.

### 5.3.1. Magnetostatic computation of the external inductance

Considering the PEC case in the MQS approximation, only the effects of the external inductance as introduced in Subsection 4.1.2 remain in the system. The BVPs for the electric field and scalar potential can be rendered real and frequency-independent by introducing the frequency-scaled fields

$$\mathbf{E}_V := \frac{1}{j\mu_0\omega} \mathbf{E}, \quad \vartheta := \frac{1}{j\mu_0\omega} \phi_c. \quad (5.27)$$

The meaning of the subscript  $V$  of  $\mathbf{E}_V$  becomes clear in Chapter 6 treating the low-frequency stabilization. With these fields the BVPs (5.24) and (5.22) become in the PEC case

$$\text{curl}(\nu_r \text{curl } \mathbf{E}_V) = -\varepsilon_r \text{grad } g \quad \text{in } \Omega_0, \quad (5.28a)$$

$$\hat{\mathbf{n}} \times \mathbf{E}_V = 0 \quad \text{on } \partial\Omega_c \cup \Gamma_{\text{el}}, \quad (5.28b)$$

$$\hat{\mathbf{n}} \times \nu_r \text{curl } \mathbf{E}_V = 0 \quad \text{on } \Gamma_{\text{mag}}, \quad (5.28c)$$

$$\hat{\mathbf{n}} \times \text{curl } \mathbf{E}_V = \frac{1}{r} \mathbf{E}_t \quad \text{on } \Gamma_a, \quad (5.28d)$$

and

$$-\operatorname{div}(\varepsilon_r \operatorname{grad} \vartheta) = \operatorname{div}(\varepsilon_r \mathbf{E}_V) + g \quad \text{in } \Omega, \quad (5.29a)$$

$$\vartheta = 0 \quad \text{on } \Gamma_{\text{el}}, \quad (5.29b)$$

$$\hat{\mathbf{n}} \cdot \varepsilon_r \operatorname{grad} \vartheta = 0 \quad \text{on } \Gamma_{\text{mag}}, \quad (5.29c)$$

$$\hat{\mathbf{n}} \cdot \operatorname{grad} \vartheta = -\frac{2}{r} \phi \quad \text{on } \Gamma_a. \quad (5.29d)$$

The BVP (5.28) can be considered MS rather than MQS due to its frequency independence.

From the result  $\vartheta$  of (5.29), the external inductance  $\mathbf{L}_{\text{ext}}$  can be computed analogously to the computation of  $\mathbf{Z}$  with (4.36),

$$[\mathbf{L}_{\text{ext}}]_{ij} = \frac{\mu_0}{I_0 A(T_{i,2})} \int_{T_{i,2}} \vartheta_j \, dS - \frac{\mu_0}{I_0 A(T_{i,1})} \int_{T_{i,1}} \vartheta_j \, dS. \quad (5.30)$$

Here,  $T_{i,1}$  and  $T_{i,2}$  are the two terminal surfaces of port  $i$ , and  $\vartheta_j$  denotes the field computed for a current excitation applied to port  $j$ .

In most cases and especially at higher frequencies the external inductance  $\mathbf{L}_{\text{ext}}$  is very close to the frequency-dependent inductance  $\mathbf{L}$  as discussed in Subsection 4.1.2. Moreover, neglecting the frequency dependence of  $\mathbf{L}$  enables a direct utilization of the extracted inductance in transient network simulations without employing the involved method introduced in Chapter 7 for frequency-dependent parasitics. Therefore, this computationally efficient PEC approach to obtain  $\mathbf{L}_{\text{ext}}$  has a high relevance for EMC applications, especially for computationally demanding device models.

### 5.3.2. Darwin approximation in the PEC case

In the PEC case, the Darwin BVP (5.25) simplifies to

$$\operatorname{curl}(\nu_r \operatorname{curl} \mathbf{E}) + \frac{\omega^2}{c^2} \varepsilon_r \operatorname{grad} \phi_c = -j\omega\mu_0 \varepsilon_r \operatorname{grad} g \quad \text{in } \Omega, \quad (5.31a)$$

$$-\operatorname{div}(\varepsilon_r \mathbf{E}) - \operatorname{div}(\varepsilon_r \operatorname{grad} \phi_c) - \frac{\omega^2}{c^2} \phi_c = j\omega\mu_0 g \quad \text{in } \Omega, \quad (5.31b)$$

$$\hat{\mathbf{n}} \times \mathbf{E} = 0 \quad \text{and} \quad \phi_c = 0 \quad \text{on } \partial\Omega_c \cup \Gamma_{\text{el}}, \quad (5.31c)$$

$$\hat{\mathbf{n}} \times \nu_r \operatorname{curl} \mathbf{E} = 0, \quad \hat{\mathbf{n}} \cdot \varepsilon_r \mathbf{E} = 0 \quad \text{and,} \quad \hat{\mathbf{n}} \cdot \varepsilon_r \operatorname{grad} \phi_c = 0 \quad \text{on } \Gamma_{\text{mag}}, \quad (5.31d)$$

which can be understood as a real-valued system to determine the imaginary parts of  $\mathbf{E}$  and  $\phi_c$ . From  $\operatorname{Im}(\phi_c)$  the reactance  $\mathbf{X} = \operatorname{Im}(\mathbf{Z})$  can be computed with (4.36). The fact that the terms on the left-hand sides of the PDEs (5.31a) and (5.31b) are either of order zero or two in  $\omega$  enables a relatively simple computation of the eigenfrequencies and eigenmodes

of models described with (5.31) by utilizing the generalized eigenvalue problem derived in [Tra+13b].

The PEC case Darwin system (5.31) and its associated eigenvalue problem constitute the foundations of the parasitic extraction and sensitivity analysis approaches of [Tra+12; Tra+13a; Tra14; HP15; Sch+18a; Sch18], that can be considered predecessors of the method developed in this thesis (as has been discussed in Chapter 1). All of these approaches depend on the fact that for a frequency-independent inductance matrix  $\mathbf{L} = \mathbf{L}_{\text{ext}}$ , which is ensured in (5.31) by neglecting wave effects and disregarding the interior of the conductors, the inverse of the nodal reactance matrix can be expressed as

$$\mathbf{X}_N^{-1} = \omega \mathbf{C}_N - \frac{1}{\omega} \mathbf{L}_N^{-1}, \quad (5.32)$$

where  $\mathbf{C}_N$  is a nodal capacitance matrix. The inverse nodal inductance matrix  $\mathbf{L}_N^{-1}$  is not necessarily invertible and relates to the (invertible) branch inductance matrix  $\mathbf{L}_{\text{ext}}$  due to (4.49) with

$$\mathbf{L}_N^{-1} = \mathbf{A}_L \mathbf{L}_{\text{ext}}^{-1} \mathbf{A}_L^T, \quad (5.33)$$

where  $\mathbf{A}_L$  is the part of the reduced incidence matrix  $\mathbf{A}_r$  associated with inductive branches.

The inductance computation method of the predecessor approaches is summarized in [Sch18] in its final form. It consists of computing  $\mathbf{X}_N$  at  $n \geq 2$  frequency points, extracting  $\mathbf{L}_N^{-1}$  by fitting (5.32) to the data, and using a Moore-Penrose pseudoinverse  $\mathbf{A}_L^+$  of the inductive incidence matrix  $\mathbf{A}_L$  to retrieve  $\mathbf{L}_{\text{ext}}$  with (5.33). For the purpose of inductance extraction any method based on Darwin's approximation in the PEC case is vastly inferior to the direct MS method of Subsection 5.3.1 with regards to efficiency and robustness (and as noted in [HP15; Sch18], the purely eigenmode-based approaches of [Tra+13b; Tra14] are entirely unfeasible for most industrial applications).

It is, however, possible to utilize the nodal capacitance matrix  $\mathbf{C}_N$  produced by the least-squares fit of the nodal reactance  $\mathbf{X}_N$  to (5.32) to extract “non-static” capacitances, i.e., capacitances that cannot be described by the electrostatic extraction approach of Section 4.1.3. A method to achieve this non-static capacitance extraction is developed in Section A.2 in the appendix. Since these non-static capacitances typically do not provide a substantial improvement over using only electrostatic capacitances, they are not part of any further considerations in this work.

## 5.4. Numerical Results

### 5.4.1. Verification with analytical results

In the MQS approximation, there exists with (4.20) an analytical result for the impedance  $Z$  of a cylindrical wire segment (i.e., a straight wire with circular cross section). This result provides a reference to verify the accuracy of the proposed parasitic extraction approach

when using the MQS BVP (5.24) for the calculation of  $\mathbf{E}$ . The full-wave and Darwin systems are compared to a numerical reference in the following subsection and the former is verified with measurement results in Chapter 9. All numerical results in this thesis use finite elements of order  $p = 2$  (i.e., all elements use both linear and quadratic polynomial basis functions). If not stated otherwise, the relative electric permittivity and magnetic permeability are assumed to be  $\varepsilon_r = \mu_r = 1$  in the entire computational domain.

For a cylindrical wire segment of length  $l = 20$  mm, radius  $r = 1$  mm, and conductivity  $\sigma = 5.8 \cdot 10^7$  S/m, Fig. 5.3 compares the analytical resistance  $R$  and inductance  $L$  of (4.20) with numerical results obtained with the MQS system for the three discussed BCs in the frequency interval  $100 \text{ kHz} \leq f \leq 100 \text{ MHz}$ . In the legend, e.g., “ABC” denotes those numerical values obtained for  $\partial\Omega = \Gamma_a$ , i.e., with the ABC applied everywhere on the boundary  $\partial\Omega$ . A spherical boundary of radius  $r_b = 80$  mm was used for the simulations and the computational domain  $\Omega$  was meshed with about 82000 elements. The numerical resistance results are identical for all BCs and agree closely with the analytical reference for  $f < 3$  MHz. For higher frequencies, the numerical resistance saturates in contrast to the analytical resistance, which continues to grow due to the skin effect. The saturating behavior is due to the finite size of the mesh cells limiting the minimal skin depth of the current density  $\mathbf{J}_s$  and thereby also the maximal resistance. However, this fundamental incapability of the FEM to compute ohmic losses at very high frequencies is inconsequential for most EMC applications, where the resistance is typically of only minor importance.

The numerical inductance results depend strongly on the applied BC: Whereas the ABC

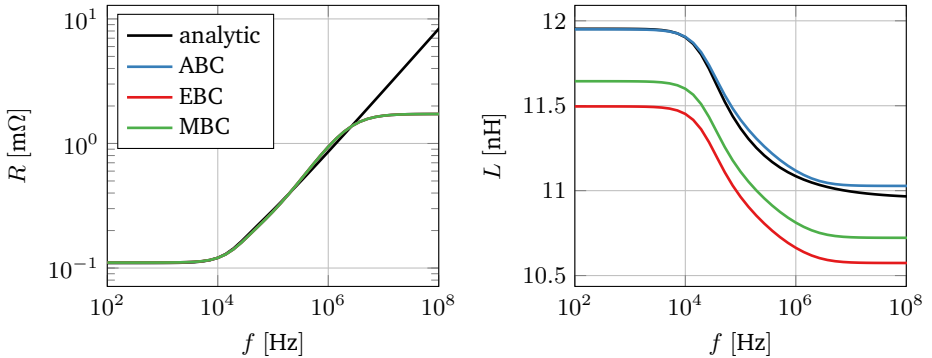


Figure 5.3.: Resistance  $R$  and inductance  $L$  of a cylindrical wire segment of length  $l = 20$  mm and radius  $r = 1$  mm in the frequency interval  $100 \text{ kHz} \leq f \leq 100 \text{ MHz}$ . The analytical result is compared to MQS numerical results using the three different BCs discussed in this chapter.

result agrees very well with the analytical reference, especially for low frequencies, the EBC and MBC results are 3.8 % and 2.6 % smaller, respectively, than the reference at  $f = 100$  Hz. While the correct open boundary result of MQS simulations lies typically between the values obtained with homogeneous Dirichlet and Neumann BCs (i.e., EBC and MBC) [STH87], this is not the case here because the MBC result uses a different source current density  $\mathbf{J}_s = \epsilon_r \text{grad } g$  due to the boundary conditions of the BVP (5.20) determining  $g$ .

The small difference between the ABC  $L$  values and the reference at higher frequencies in Fig. 5.3 is due to a difference in the current excitation: The analytical values assume that the current density is determined by the skin effect already on the terminals (i.e., the planar surfaces at the ends of the cylinder). In contrast, since the proposed parasitic extraction method must be applicable for arbitrary models, it enforces a homogeneous current density on the terminals as stated in (5.9). Fig. 5.4 shows the resistance and inductance results of a similar wire of the greater length  $l = 50$  mm, which were calculated using a spherical boundary of radius  $r_b = 200$  mm. For this longer wire, the relative influence of the homogeneous current excitation on the inductance is visibly smaller. However, the displayed  $L$  values show that the ABC produces slightly less accurate results for the wire of length  $l = 50$  mm. This is because the sources of the longer wire fulfill the requirement of the ABC that the sources must lie in the center of the domain less well.

Fig. 5.5a illustrates the influence of the  $g$  field compensation term that eliminates the

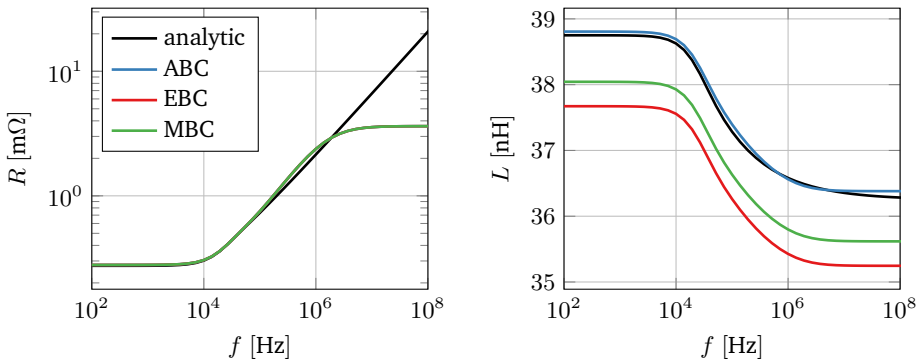


Figure 5.4.: Same plot as Fig. 5.3 but for a wire of length  $l = 50$  mm. For this longer wire, the difference between ABC and analytical  $L$  results is smaller at high frequencies than in Fig. 5.3 (relative to the respective  $L$  values) because of the smaller influence of the homogeneous current density imprinted at the terminals. The ABC  $L$  result at low-frequencies shows that the ABC works slightly less well for the longer model.

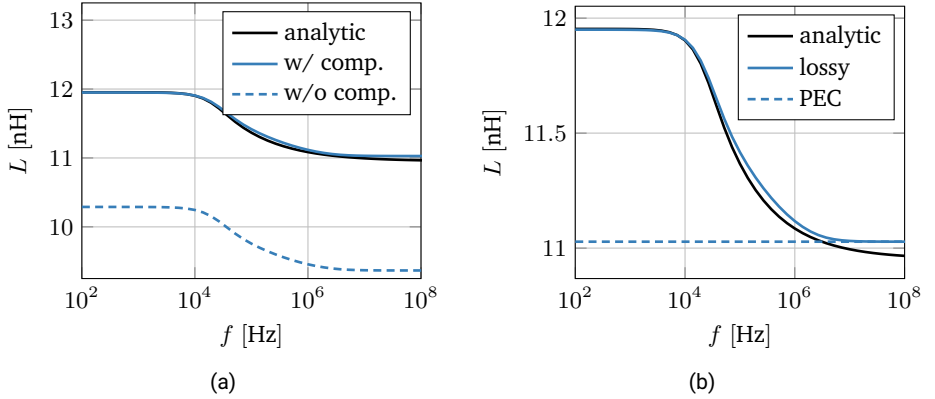


Figure 5.5.: Inductance  $L$  of the wire of Fig. 5.3, only considering ABC results. (a) Comparison of numerical values obtained with and without the inductive compensation provided by the  $g$  term in (5.22). (b) Comparison of the MQS results obtained with the BVP (5.24), that considers ohmic losses, and the PEC case BVP (5.28).

unwanted inductive influence of the source current density  $\mathbf{J}_s$  in (5.22) on the inductance  $L$ . The values obtained without the compensation term are about 14 % too low compared to both the analytical reference and the values with compensation.

Fig. 5.5b compares the inductance  $L$  obtained with the MQS BVP (5.24) that considers ohmic losses to the inductance of the frequency-independent PEC case BVP (5.24). As discussed in Subsection 5.3.1, the latter BVP directly gives the external inductance  $L_{\text{ext}}$ , which is also the high-frequency limit of the MQS inductance.

Fig. 5.6 shows the resistance and inductance of the 20 mm wire of Fig. 5.3, but using the full-wave BVP (5.3) instead of the MQS BVP (5.24) for the numerical results. The figure illustrates three main points: First, the absorbing BC derived in Section A.1 is capable of obtaining the same accurate  $R$  and  $L$  values in the low-frequency regime as the asymptotic BC of the MQS system. Second, whereas the EBC and MBC do not allow for power dissipation through radiation since all waves are reflected at the boundary  $\partial\Omega$  with these BCs, the ABC  $R$  values exhibit the  $f^2$  behavior of radiation resistance [RWV94, Section 12.7] in the high-frequency regime. Third, for frequencies  $f > 100$  MHz the inductance loses its at lower frequencies relatively constant behavior due to resonance effects. This shows that for high frequencies, where the MQS approximation is no longer valid, the concept of inductance loses its usefulness, and a direct analysis of the impedance  $Z$  is more appropriate.

While the partial inductance is in general a gauge-dependent quantity, as discussed in

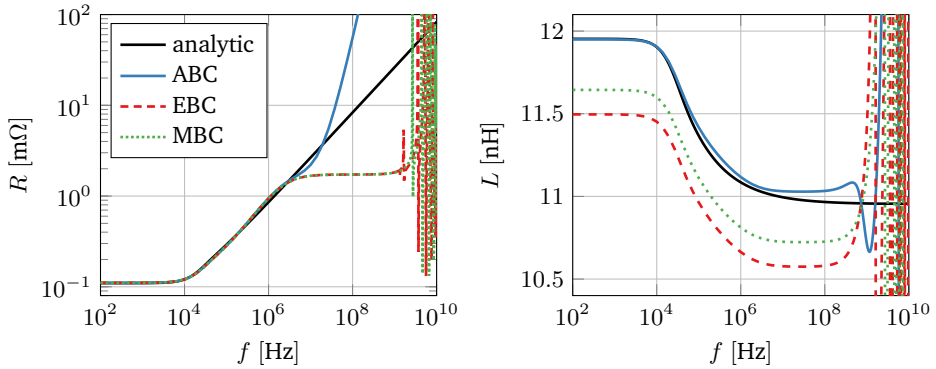


Figure 5.6.: Same plot as Fig. 5.3 but showing results of the full-wave BVP (5.3) in the larger frequency interval  $100 \text{ kHz} \leq f \leq 10 \text{ GHz}$ . For  $f < 100 \text{ MHz}$ , the full-wave values are identical to the MQS values of Fig. 5.3, with the exception of the radiation resistance in the ABC  $R$  values. For  $f > 100 \text{ MHz}$ , the  $L$  values become dominated by resonances, illustrating that the concept of inductance is useful mainly in the quasistatic frequency regime.

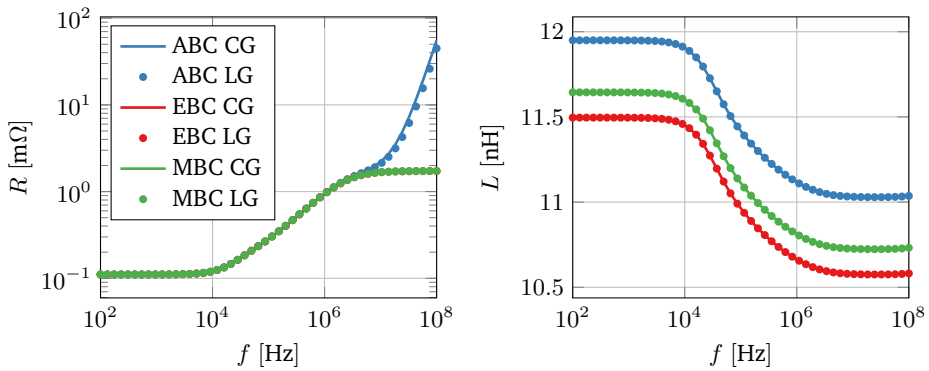


Figure 5.7.: Same plot as Fig. 5.6 but comparing results obtained with the Coulomb-gauged (CG) BVP (5.22) to results of the Lorenz-gauged (LG) equation (5.23) for frequencies where the inductance remains a useful concept. The different gauges yield the same resistance and inductance results, the only difference being slightly different radiation resistances for the ABC values caused by the difference of the BCs (A.6) and (A.11).

Subsection 4.1.2, Fig. 5.7 demonstrates that the  $R$  and  $L$  values obtained with the Coulomb-gauged BVP (5.22) and Lorenz-gauged equation (5.23) agree almost perfectly at those frequencies where the inductance remains a useful concept. The only minor discrepancy that can be observed in the plot is a slightly different radiation resistance at frequencies  $f > 10$  MHz in the case of an ABC boundary. This difference is caused by the fact that the Coulomb-gauged PDE (5.22a) demands the asymptotic BC (A.6) on  $\Gamma_a$  whereas the Lorenz-gauged PDE (5.23) requires the scalar absorbing BC (A.11).

Table 5.1 compares the computational cost of extractions using the full-wave BVP (5.3), the MQS (5.24), and the MS PEC case BVP (5.28) for the 20 mm wire model discretized with 82000 elements (using ABCs on  $\partial\Omega$ ). The table references the respective BVPs to compute the electric field  $\mathbf{E}$ , and lists the dimension  $N$  of the  $N \times N$  system matrices resulting from a FE discretization of the BVPs as described in Chapter 6. The average setup time  $\bar{t}_0$  contains the time needed to assemble the FE matrices, solve the  $g$  BVP (5.20), and factorize the system matrix of the  $\phi_c$  BVP (5.22) (or  $\vartheta$  BVP (5.29) for the PEC system). Finally,  $\bar{t}_f$  is the average impedance computation time per frequency point after the setup of the system, which is mostly equivalent to the time necessary to solve the  $\mathbf{E}$  BVP. For the frequency-independent MS PEC system, the time to solve the  $\mathbf{E}$  BVP is included in  $\bar{t}_0$ . The computations were made on a 2.8 GHz Intel Xeon CPU, using the Intel MKL PARDISO direct sparse solver to solve the FE linear systems. Whereas the solver is written in the compiled programming languages Fortran and C, the remaining program is written in the interpreted language Python, that emphasizes readability over raw computational performance. The used implementation can therefore not be understood as fully optimized with respect to performance, in particular regarding the assembly of the FE matrices, which contributes to the setup time  $\bar{t}_0$ .

A performance comparison for a larger model, that also includes the Darwin system of Subsection 5.2.2, can be found in [SKD22a].

Table 5.1.: Comparison of the computational cost of extractions with the full-wave system, the MQS system, and the MS PEC case system. Here,  $N$  is the dimension of the matrix resulting from a FE discretization of the  $\mathbf{E}$  BVP,  $\bar{t}_0$  denotes the average setup time of the system, and  $\bar{t}_f$  is the average extraction time per frequency point after the setup of the system. For the frequency-independent MS PEC system,  $\bar{t}_0$  is the entire average computation time.

	full wave	MQS	MS PEC
$\mathbf{E}$ BVP	(5.3)	(5.24)	(5.28)
$N$	520 k	435 k	336 k
$\bar{t}_0$ [s]	35.7	34.9	38.2
$\bar{t}_f$ [s]	86.5	36.1	-

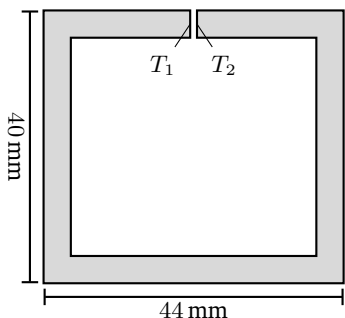


Figure 5.8.: Rectangular loop with a conductor cross section of  $4 \times 4 \text{ mm}^2$ . The gap between the terminals  $T_1$  and  $T_2$  is 1 mm wide. The conductivity is set to  $\sigma = 5.8 \cdot 10^7 \text{ S/m}$ . For simulation, the loop is considered in a computational domain with a spherical boundary of radius  $r_b = 125 \text{ mm}$ , and the whole model is discretized with about 40000 finite elements.

### 5.4.2. Loop model at high frequencies

The analytical MQS result of the previous subsection is unsuitable as a reference for the high-frequency behavior of the full-wave and Darwin systems. To demonstrate the different behavior these systems exhibit depending on the chosen boundary condition, numerical reference values are obtained with the high-frequency solver of the commercial FE software CST Studio Suite [CST21] (abbreviated CST in the following). This software does not de-embed the impedance from the inductive influence of the current source as described in Subsections 4.1.4 and 5.1.4. Therefore, in order to facilitate a comparison between this reference and the proposed parasitic extraction method, a loop model with a very small distance between its two terminals is considered as depicted in Fig. 5.8, such that the influence of the current return path on the impedance is negligible. The CST values are computed in a box-shaped domain with the software’s “open boundary” feature, that uses a perfectly matched layer. As discussed in Section A.1, this open boundary approach can be assumed to be more accurate at high frequencies than the ABC used to calculate  $\mathbf{E}$  in (5.3), and is therefore a suitable benchmark.

Fig. 5.9a compares the modulus of the impedance  $Z$  computed with the full-wave BVP (5.3) using all three introduced BCs to the CST reference in a high frequency regime. While all results agree reasonably well for  $f < 1 \text{ GHz}$ , at higher frequencies the EBC and MBC results exhibit numerous resonances. The fact that the resonances’ positions depend on the BC shows that they are caused by wave reflections from the boundary. This behavior is absent from the ABC result, which agrees reasonably well with the reference throughout the considered frequency interval. This demonstrates, firstly, that EBC and MBC are entirely unsuitable for parasitic extraction of a component in free space when using the full-wave system at high frequencies. And secondly, that the relatively simple ABC used in this work is a suitable choice for parasitic extraction not only at low but also at high frequencies.

Fig. 5.9b compares the modulus of the impedance  $Z$  obtained with the Darwin BVP (5.25) using the EBC and MBC to both the full-wave ABC result and the CST reference.

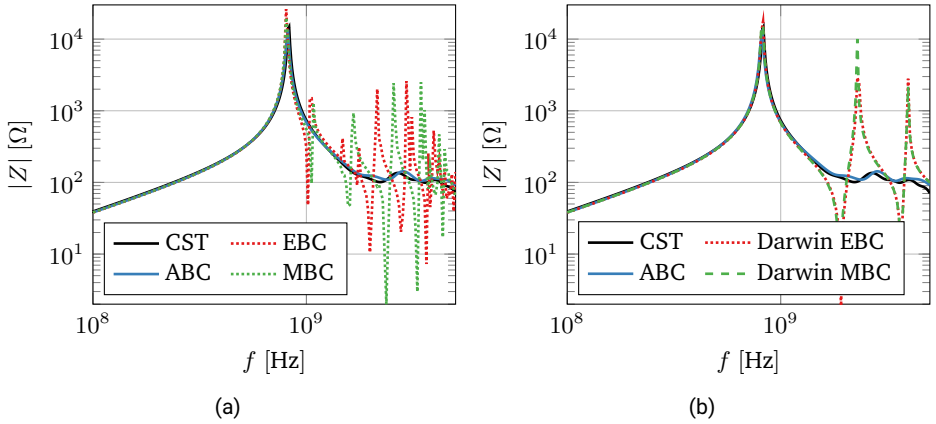


Figure 5.9.: Modulus of the impedance  $Z$  of the loop model depicted in Fig. 5.8 in the high frequency regime  $100 \text{ MHz} \leq f \leq 5 \text{ GHz}$ . (a) Full-wave results compared to the CST reference. The ABC values are reasonably close to the reference whereas the EBC and MBC results become dominated by resonances at higher frequencies. (b) EBC and MBC results of the Darwin system compared to the full-wave ABC result and the CST reference. The Darwin results agree for both BCs, indicating that their resonances do not stem from interactions with the boundary.

The fact that the Darwin results agree for both BCs indicates that their resonances are not caused by interactions with the boundary but rather by inductive and capacitive effects within the loop. The Darwin system can hence be an alternative to the full-wave system for applications where the radiation resistance and its dampening of resonances at higher frequencies is not needed.



---

## 6. Low-Frequency Stable Finite Element Discretization

---

### 6.1. Introduction

The parasitic extraction method developed in Chapter 5 requires a numerical solution method for its various BVPs. The FEM discussed in Chapter 3 is ideal for this task as it allows for a flexible discretization of the computational domain without requiring any special treatment for inhomogeneous material parameters. However, FEM solutions of the frequency-domain Maxwell equations in general and of the E-field formulation (5.2) in particular are notorious for exhibiting stability issues at low frequencies. Remedying this so-called low-frequency (LF) breakdown has been the concern of numerous works in the past decades, e.g., [DB96; HKO08; ZJ10; JFD15; Ell+17]. A comprehensive literature review is provided in [Ell+17].

For the E-field form (5.2) the cause of the LF breakdown is easily understood: Applying the divergence operator to the equation shows that at finite frequencies  $f > 0$  it contains both the continuity equation (2.12) in the conducting domain  $\Omega_c$  and Gauss law (2.11c) in the non-conducting domain  $\Omega_0$  (the former scaled by  $\omega \equiv 2\pi f$  and the latter by  $\omega^2$ ). These scalar equations are necessary to determine the gradient-field component of  $\mathbf{E}$ . As gradient fields lie in the kernel of the curl operator, the equation can at  $f = 0$  only determine the solenoidal (i.e., divergence-free) component of  $\mathbf{E}$ , while its irrotational component remains undetermined. Since numerical solutions must rely on the finite precision of computers, round-off errors cause the breakdown to already occur at a finite frequency  $f > 0$ . In [ZJ10] an estimate of the breakdown frequency is provided for the non-lossy case, where no subdomains of finite conductivity  $\sigma$  are included in the computational domain  $\Omega$  (i.e., the PEC case of Section 5.3).

A treatment of the LF breakdown in the non-lossy case is significantly less difficult than a treatment of the general lossy case. At the cost of introducing an additional unknown scalar field, the potential formulation (2.27) contains with (2.27b) Gauss's law explicitly. While a FE discretization of (2.27) results in a singular system matrix due to the gauge freedom of the potentials (discussed in Section 2.4), this does not hinder a solution of the linear system with an iterative solver as its right-hand side (RHS) is guaranteed to lie in the span of its matrix. Both gauged and ungauged non-lossy potential formulations are discussed in [DB96].

The superfluous DoFs that render the FE linear system singular can be eliminated by applying a tree-cotree gauge [AR88]. The approach eliminates the pure gradient-field DoFs

of the unknown vector field after FE discretization, and is discussed in detail in Subsection 6.6.1. In [JFD15] the non-conducting subdomain  $\Omega_0$  is treated with this approach.

The general non-lossy case poses a challenge also in the potential formulation. In contrast to the E-field formulation, supplementing the potential formulation of the Ampère-Maxwell law (2.27a) with Ohm's law (2.16) leads to the continuity equation (2.12) being contained in the equation even at  $f = 0$ . However, enforcing Gauss's law (2.27b) explicitly in the entire domain  $\Omega$  yields in this case

$$\operatorname{div} \left( \varepsilon + \frac{\sigma}{j\omega} (\operatorname{grad} \phi + j\omega \mathbf{A}) \right) = \frac{1}{j\omega} \mathbf{J}_s. \quad (6.1)$$

This equation contains the unstable term  $(j\omega)^{-1} \operatorname{div} \sigma \operatorname{grad} \phi$  on its left-hand side (LHS). Moreover, for non-divergence free source current densities  $\mathbf{J}_s$  (as used in this work with (5.10)) the RHS diverges as well for  $\omega \rightarrow 0$ . Hiptmair et al. [HKO08] avoid a diverging LHS with a so-called generating systems approach. A splitting of the Sobolev space  $H^1$  of the ESP  $\phi$  into a subspace of functions that are constant on the conductors and a complementary subspace enables the enforcement of Gauss's law in the non-conducting domain only, while in the conducting domain the Coulomb gauge is enforced. The resulting system matrices are singular and non-symmetric.

The formulation of Jochum et al. [JFD15] yields symmetric regular matrices also in the general lossy case, thereby facilitating the use of direct solvers. This is accomplished by treating conducting and non-conducting regions with separate equations and enforcing interface conditions on the boundary  $\partial\Omega_c$  of the conductors. Compared to the E-field formulation, this approach requires additional DoFs in the conducting regions and can yield significantly less sparse matrices, increasing the computation times considerably [Joc+16].

A particularly elegant and efficient solution of the LF instability was developed by Eller et al. in [Ell+17] and in Eller's dissertation [Ell17]. This approach can be considered the synthesis of the approaches of Hiptmair et al. [HKO08] and Jochum et al. [Joc+16]: From the former it adopts the splitting of the Sobolev space  $H^1$  and from the latter the perspective that understands the tree-cotree approach as a Helmholtz-type decomposition of the space  $H(\operatorname{curl})$ . Eller et al. unite these two function space splittings to the effect of decomposing  $H(\operatorname{curl})$  into three parts, thereby enabling a splitting of the E-field formulation (5.2) into three separate equations in the weak formulation. An individual frequency scaling of the three equations causes the formulation to be stable at all frequencies (a pre-processing step is required if  $\operatorname{div} \mathbf{J}_s \neq 0$ ). In the PEC case of Section 5.3 the equations of [Ell+17] and [JFD15] are equivalent.

The LF stabilization scheme for the parasitic excitation method of Chapter 5 developed in the following sections is based on the LF stable E-field formulation of Eller et al. for the following reasons:

1. A FE discretization of the formulation yields a regular system matrix, facilitating the use of a direct solver and thereby a computationally efficient evaluation of the system

for multiple right-hand sides. For the computation of an  $N$ -port impedance matrix  $N$  different current excitations (right-hand sides) must be considered.

2. A discretization of the formulation requires virtually the same number of DoFs as conventional discretizations of the E-field formulation. Moreover, the number of non-zero entries in the resulting system matrix is not significantly increased. The overall computational cost is hence comparable to that of conventional FE solutions of the E-field formulation.
3. The elegant approach of fundamentally splitting the Sobolev space  $H(\text{curl})$  enables a seamless treatment of the quasistatic approximations of Section 5.2 and the PEC case of Section 5.3, in each case yielding systems with a minimal number of DoFs.

The remainder of this chapter is an expansion of the discussion presented in [SKD22c] and structured as follows: Section 6.2 summarizes the approach of Eller et al. and applies it to the specific source current density  $\mathbf{J}_s$  used in Chapter 5. In addition to the EBCs used in [Ell+17], also MBCs and the ABCs of Section A.1 are considered. Section 6.3 details how the computation of the compensated scalar potential  $\phi_c$  can be stabilized. Sections 6.4 and 6.5 apply the stabilization to the quasistatic approximations and the PEC case, respectively. Section 6.6 discusses how the splitting of  $H(\text{curl})$  can be realized with  $H^1$ -conforming and  $H(\text{curl})$ -conforming finite elements, considering crucial details especially with regards to the tree creation that were omitted in [Ell+17; Ell17]. Finally, Section 6.7 compares numerical results obtained with and without LF stabilization.

## 6.2. Stabilization of the Electric Field Formulation

Before the LF stabilization can be discussed, the E-field-formulation BVP (5.3) must be expressed in weak form as required by the FEM. The EBC (5.3b) is an essential BC that is considered in the FEM by restricting the Sobolev space of the trial and test functions. To this end, three subspaces of  $H(\text{curl}, \Omega)$  and  $H^1(\Omega)$  are defined as

$$H(\text{curl}, \Omega)' := \{\mathbf{f} \in H(\text{curl}, \Omega) : \hat{\mathbf{n}} \times \mathbf{f} = 0 \text{ on } \Gamma_{\text{el}}\}, \quad (6.2)$$

$$H^1(\Omega)' := \{\psi \in H^1(\Omega) : \psi = 0 \text{ on } \Gamma_{\text{el}}\}, \quad (6.3)$$

$$H^1(\Omega)'' := \{\psi \in H^1(\Omega) : \psi = 0 \text{ on } \Gamma_{\text{el}} \cup \Gamma_{\text{a}}\}. \quad (6.4)$$

To make the the weak formulations below more concise, a bracket notation is introduced for the inner products over  $\Omega$  and  $\Gamma_i \subseteq \partial\Omega$ ,

$$\langle \mathbf{f}, \mathbf{g} \rangle := \int_{\Omega} \mathbf{f} \cdot \mathbf{g} \, dV, \quad \langle \mathbf{f}, \mathbf{g} \rangle_{\Gamma_i} := \int_{\Gamma_i} \mathbf{f} \cdot \mathbf{g} \, dS, \quad (6.5)$$

where  $\mathbf{f}, \mathbf{g} : \mathbb{R}^3 \rightarrow \mathbb{C}^n$  and  $n \in \{1, 3\}$ . The non-essential BCs (5.3c) and (5.3d) are considered through a boundary term that originates from an integration by parts applied to the curl-curl term of (5.3a): In the weak form, the E-field formulation is tested with a function  $\mathbf{f} \in H(\text{curl}, \Omega)'$  (i.e., the scalar product with the test function is integrated over the domain  $\Omega$ ). With the vector calculus identity [Mon03, Section 3]

$$\langle \text{curl } \mathbf{g}, \mathbf{f} \rangle = \langle \mathbf{g}, \text{curl } \mathbf{f} \rangle + \langle \hat{\mathbf{n}} \times \mathbf{g}, \mathbf{f} \rangle_{\partial\Omega} \quad \forall \mathbf{g}, \mathbf{f} \in H(\text{curl}, \Omega), \quad (6.6)$$

the curl-curl term becomes

$$\begin{aligned} \langle \text{curl}(\nu_r \text{curl } \mathbf{E}), \mathbf{f} \rangle &= \langle \nu_r \text{curl } \mathbf{E}, \text{curl } \mathbf{f} \rangle + \langle \hat{\mathbf{n}} \times \nu_r \text{curl } \mathbf{E}, \mathbf{f} \rangle_{\partial\Omega} \\ &= \langle \nu_r \text{curl } \mathbf{E}, \text{curl } \mathbf{f} \rangle + \alpha \langle \mathbf{E}_t, \mathbf{f} \rangle_{\Gamma_a}, \end{aligned} \quad (6.7)$$

with  $\alpha = (jk + 1/r)$ , and the angular vacuum wave number  $k = \omega/c$ . The boundary term vanishes on the electric boundary  $\Gamma_{\text{el}}$  because there all test functions  $\mathbf{f} \in H(\text{curl}, \Omega)'$  are zero and on the magnetic boundary  $\Gamma_{\text{mag}}$  due to the MBC (5.3c). On the ABC boundary  $\Gamma_a$  the term is expressed with (5.3a). With (6.7) the weak form of the BVP (5.3) reads:

Find  $\mathbf{E} \in H(\text{curl}, \Omega)'$  such that

$$\begin{aligned} \langle \nu_r \text{curl } \mathbf{E}, \text{curl } \mathbf{f} \rangle + \alpha \langle \mathbf{E}_t, \mathbf{f} \rangle_{\Gamma_a} + j\mu_0 ck \langle \sigma \mathbf{E}, \mathbf{f} \rangle - k^2 \langle \varepsilon_r \mathbf{E}, \mathbf{f} \rangle &= -j\mu_0 ck \langle \mathbf{J}_s, \mathbf{f} \rangle \\ \forall \mathbf{f} \in H(\text{curl}, \Omega)'. \end{aligned} \quad (6.8)$$

A weak-form BVP for the scalar field  $g$  that provides  $\mathbf{J}_s$  with (5.12) is obtained by testing PDE (5.20a) with the functions of (6.4). The divergence operator on the LHS of the equation is transformed into a gradient operator acting on the test function  $\psi$  with an equation analogous to (6.6): Using [Mon03, Section 3]

$$- \langle \text{div } \mathbf{f}, \psi \rangle = \langle \mathbf{f}, \text{grad } \psi \rangle - \langle \hat{\mathbf{n}} \cdot \mathbf{f}, \psi \rangle_{\partial\Omega} \quad \forall \mathbf{f} \in H(\text{div}, \Omega), \psi \in H^1(\Omega) \quad (6.9)$$

and the MBC (5.20c), the weak form of the BVP (5.20) reads

Find  $g \in H^1(\Omega)''$  such that

$$\langle \varepsilon_r \text{grad } g, \text{grad } \psi \rangle = - \langle \text{div } \mathbf{J}_s, \psi \rangle \quad \forall \psi \in H^1(\Omega)''. \quad (6.10)$$

As mentioned in the previous section, the guiding principle of Eller et al.'s LF stabilization is to divide the Sobolev space  $H(\text{curl}, \Omega)'$  into three subspaces in a way that enables an individual frequency scaling of the three resulting LHS terms of (6.8). First, a Helmholtz-type decomposition, facilitated by the first level of the De Rham complex (3.16), is used to divide  $H(\text{curl}, \Omega)'$  into a subspace of functions with non-vanishing curl denoted  $V$  and the subspace of gradient fields  $Y$ . In a generalized form allowing for the use of an ABC boundary  $\Gamma_a$ , the decomposition reads

$$H(\text{curl}, \Omega)' = V \oplus Y, \quad (6.11a)$$

$$\forall \mathbf{v} \in V \quad \langle \text{curl } \mathbf{v}, \text{curl } \mathbf{v} \rangle \neq 0 \vee \langle \hat{\mathbf{n}} \times \mathbf{v}, \hat{\mathbf{n}} \times \mathbf{v} \rangle_{\Gamma_a} \neq 0, \quad (6.11b)$$

$$Y := \{ \mathbf{w} \in H(\text{curl}, \Omega)' : \text{curl } \mathbf{w} = 0 \wedge \hat{\mathbf{n}} \times \mathbf{w} = 0 \text{ on } \Gamma_a \}. \quad (6.11c)$$

Jochum et al. formulate a similar decomposition [Joc+16]. Whereas (6.11c) defines the space  $Y$  directly, (6.11a) and (6.11b) are only necessary conditions for  $V$  (i.e.,  $V$  is not uniquely defined). In the presence of a non-empty ABC boundary  $\Gamma_a \neq \emptyset$ , the tangential components of the functions on  $\Gamma_a$  are fully assigned to  $V$ . Section 6.6 discussed how the finite-dimensional subspaces  $V_h \subset V$  and  $Y_h \subset Y$  necessary for a FE discretization can actually be constructed using  $H(\text{curl})$ - and  $H^1$ -conforming finite elements.

In the general lossy case, the space of gradient fields  $Y$  requires a further decomposition similar to that used by Hiptmair et al. for the scalar Sobolev space  $H^1$  in [HKO08]:

$$Y = W \oplus U, \quad (6.12a)$$

$$\forall \mathbf{w} \in W \quad \langle \mathbf{w}, \mathbf{w} \rangle_{\Omega_c} \neq 0, \quad (6.12b)$$

$$U := \{ \mathbf{u} \in Y : \mathbf{u} = 0 \text{ in } \Omega_c \}. \quad (6.12c)$$

The subscript of the bracket notation in (6.12b) denotes that the domain of its integral is restricted to the conducting subdomain  $\Omega_c$ . Hence, functions  $\mathbf{w} \in W$  must not vanish everywhere in  $\Omega_c$ .

With the decomposition

$$H(\text{curl}, \Omega)' = V \oplus W \oplus U \quad (6.13)$$

the BVP (6.8) can be stabilized in two steps: Firstly, the LHS of the equation is treated such that the system matrix resulting from FE discretization has full rank and a finite condition number for  $k \rightarrow 0$ . Secondly, as the excitations considered in this work are not divergence free ( $\text{div } \mathbf{J}_s \neq 0$ ), a pre-processing step is necessary to also render the RHS LF stable. This second step may be omitted for conductive extraction topologies if the DC point  $f = k = 0$  is not of interest (e.g., for frequencies  $f \geq 1$  Hz).

### 6.2.1. Stabilizing the System Matrix

Utilizing the Sobolev space splitting of (6.13), the electric field  $\mathbf{E}$  can be expressed with frequency-scaled fields from the three subspaces as

$$\mathbf{E} = j\mu_0 c \left( k\mathbf{E}_V + \sqrt{k}\mathbf{E}_W + \mathbf{E}_U \right) \quad (6.14)$$

with  $\mathbf{E}_V \in V$ ,  $\mathbf{E}_W \in W$ , and  $\mathbf{E}_U \in U$ . The scaling differs slightly from [Ell+17] to simplify the resulting equations and facilitate the implementation in a computer program by eliminating some constant factors. The imaginary unit  $j$  is part of the scaling such that the linear system resulting from FE discretization becomes real in the special case of perfect electric conductors discussed in Section 5.3. The magnetic flux density can be recovered with the simple expression  $\mathbf{B} = -\mu_0 \text{curl } \mathbf{E}_V$ , illustrating that  $\mathbf{E}_V$  is essentially a MVP, while  $\mathbf{E}_W$  and  $\mathbf{E}_U$  can be understood as gradient fields produced by ESPs. Inserting (6.14)

into the weak E-field formulation (6.8) and testing with the functions of the subspaces individually yields the LF stable weak form BVP:

Find  $\mathbf{E}_V \in V$ ,  $\mathbf{E}_W \in W$ , and  $\mathbf{E}_U \in U$  such that

$$\begin{aligned} \langle \nu_r \operatorname{curl} \mathbf{E}_V, \operatorname{curl} \mathbf{v} \rangle + \alpha \langle \mathbf{E}_V^t, \mathbf{v} \rangle_{\Gamma_a} + j \langle \hat{\sigma}(\sqrt{k} \mathbf{E}_W + k \mathbf{E}_V), \mathbf{v} \rangle \\ - \langle \varepsilon_r(k \mathbf{E}_U + k^{\frac{3}{2}} \mathbf{E}_W + k^2 \mathbf{E}_V), \mathbf{v} \rangle = - \langle \mathbf{J}_s, \mathbf{v} \rangle, \end{aligned} \quad (6.15a)$$

$$j \langle \hat{\sigma}(\mathbf{E}_W + \sqrt{k} \mathbf{E}_V), \mathbf{w} \rangle - \langle \varepsilon_r(\sqrt{k} \mathbf{E}_U + k \mathbf{E}_W + k^{\frac{3}{2}} \mathbf{E}_V), \mathbf{w} \rangle = \frac{1}{\sqrt{k}} \langle \operatorname{div} \mathbf{J}_s, \psi_W \rangle, \quad (6.15b)$$

$$- \langle \varepsilon_r(\mathbf{E}_U + \sqrt{k} \mathbf{E}_W + k \mathbf{E}_V), \mathbf{u} \rangle = \frac{1}{k} \langle \operatorname{div} \mathbf{J}_s, \psi_U \rangle, \quad (6.15c)$$

for all  $\mathbf{v} \in V$ ,  $\mathbf{w} \equiv \operatorname{grad} \psi_W \in W$ , and  $\mathbf{u} \equiv \operatorname{grad} \psi_U \in U$ .

Here,  $\hat{\sigma} := \mu_0 c \sigma$  denotes the scaled conductivity and  $\mathbf{E}_V^t$  the tangential component of  $\mathbf{E}_V$ . The scalar fields  $\psi_U$  and  $\psi_W$  are the potentials that produce the gradient fields  $\mathbf{u}$  and  $\mathbf{w}$ , respectively. The formulation (6.15) differs from the one found in [Ell+17] not only due to the  $\Gamma_a$  term but also because the right-hand sides of (6.15b) and (6.15c) are expressed with  $\operatorname{div} \mathbf{J}_s$  and the potentials  $\psi_U$  and  $\psi_W$ . This choice is made because the input quantity of the discussed parasitic extraction method is  $\operatorname{div} \mathbf{J}_s$  (provided by (5.10)). The expression utilizes the identity

$$\langle \mathbf{J}_s, \operatorname{grad} \psi \rangle = - \langle \operatorname{div} \mathbf{J}_s, \psi \rangle \quad \forall \operatorname{grad} \psi \in Y, \quad (6.16)$$

which follows from (6.9) using the MBC (5.8).

The system matrix resulting from an FE discretization of (6.15) is symmetric. The system (6.15) is LF stable only in the sense that the resulting system matrix has full rank at all frequencies. The right-hand sides of (6.15b) and (6.15c) diverge for  $k \rightarrow 0$ , which can pollute the solution  $\mathbf{E}$  at very low frequencies and prohibits any solution at the DC point  $k = 0$ . This diverging behavior can be eliminated as described in the following subsection.

To illustrate the LF breakdown and stabilization of the system matrix, a model of a conductor segment of length  $l = 10$  mm with a square cross section of  $A = 1$  mm<sup>2</sup> is considered with a magnetic boundary  $\partial\Omega = \Gamma_{\text{mag}}$  at distance  $d = 5$  mm. A FE discretization using 680 elements yields an  $N \times N$  system matrix with  $N = 4518$  for the unstable system of (6.8) and almost the same number  $N = 4519$  for the stabilized system of (6.15). The comparatively low matrix dimensions facilitate a direct computation of condition number and rank deficiency (i.e., dimension of the kernel of the matrix). Fig. 6.1 displays condition numbers of both the unstable and stabilized system matrix in the frequency interval  $100 \text{ Hz} \leq f \leq 100 \text{ kHz}$ , as well as the rank deficiency in the unstable case (the stabilized system matrix has full rank at all frequencies). Whereas the condition number of the stabilized matrix stays relatively constant, the condition number of the unstable matrix rises sharply for frequencies  $f < 10$  kHz before exhibiting an increasingly plateauing behavior due to finite machine precision preventing an exact computation. This is accompanied by the rank deficiency increasing from 0 at  $f = 10$  kHz to 630 at  $f = 1$  kHz.

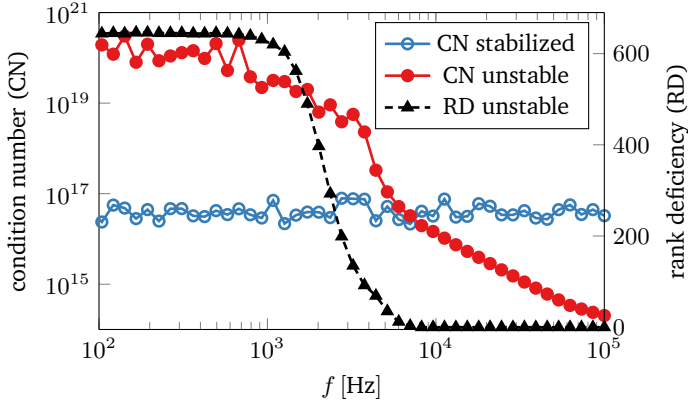


Figure 6.1.: [SKD22c] Frequency dependence of the condition number (CN) of the system matrices of both the unstable and stabilized system, and rank deficiency (RD) of the unstable matrix for a conductor segment model. Whereas both the CN and RD of the unstable matrix indicate a LF breakdown for  $f < 10$  kHz, the stabilized matrix has an approximately constant CN (and full rank) at all frequencies.

## 6.2.2. Stabilizing the Right-Hand Side

The strategy employed by Eller et al. to stabilize the diverging RHS of (6.15) is re-derived in the following from a slightly less abstract angle than in [Ell+17], and applied to the source current density used in the proposed parasitic extraction method. The general idea is to eliminate the diverging RHS terms by first solving the electroquasistatic (EQS) equation in the static limit for the capacitive electrostatic field  $\mathbf{F}_U \in U$  and the static current field  $\mathbf{F}_W \in W$ . The total electric field is then expressed in the weak formulation (6.8) as a sum of these static fields and the non-static contributions  $\mathbf{E}_V \in V$ ,  $\mathbf{E}_W \in W$ , and  $\mathbf{E}_U \in U$ ,

$$\mathbf{E} = j\mu_0 c \left( k\mathbf{E}_V + \sqrt{k}\mathbf{E}_W + \mathbf{E}_U - j\mathbf{F}_W - \frac{1}{k}\mathbf{F}_U \right). \quad (6.17)$$

This yields a stabilized system with the same operator as (6.15) but no diverging terms on the RHS.

The electric field in the EQS approximation is a gradient field  $\mathbf{E}_{\text{eqs}} \in Y$ . The EQS PDE (2.38) can be solved in the static limit  $k \rightarrow 0$  with the ansatz

$$\lim_{k \rightarrow 0} \mathbf{E}_{\text{eqs}} = \mu_0 c \left( \mathbf{F}_W + \frac{1}{jk} \mathbf{F}_U \right). \quad (6.18)$$

The static current field  $\mathbf{F}_W \in W$  produces the static conduction current  $\hat{\sigma}\mathbf{F}_W$ , and the electrostatic field  $\mathbf{F}_U \in U$  captures the static capacitive effects in the non-conducting domain  $\Omega_0$ . Testing (2.38) in the static limit separately with all scalar functions  $\psi_U$  and  $\psi_W$  that produce the gradient fields  $\mathbf{u} = \text{grad } \psi_U \in U$  and  $\mathbf{w} = \text{grad } \psi_W \in W$ , respectively, yields two BVPs for  $\mathbf{F}_U$  and  $\mathbf{F}_W$ , that can be solved in sequence:

Find  $\mathbf{F}_U \in U$  and  $\mathbf{F}_W \in W$  such that

$$\langle \varepsilon_r \mathbf{F}_U, \mathbf{u} \rangle = \langle \text{div } \mathbf{J}_s, \psi_U \rangle \quad \forall \mathbf{u} \equiv \text{grad } \psi_U \in U, \quad (6.19)$$

$$\langle \hat{\sigma} \mathbf{F}_W, \mathbf{w} \rangle = \langle \text{div } \mathbf{J}_s, \psi_W \rangle - \langle \varepsilon_r \mathbf{F}_U, \mathbf{w} \rangle \quad \forall \mathbf{w} \equiv \text{grad } \psi_W \in W. \quad (6.20)$$

Again (6.16) is used express the right-hand sides of the equations with  $\text{div } \mathbf{J}_s$ .

Inserting (6.17) into the unstable weak form (6.8) yields a system for the non-static fields  $\mathbf{E}_V$ ,  $\mathbf{E}_W$ , and  $\mathbf{E}_U$  with the same LHS as (6.15) and the stabilized RHS of

$$\dots = - \langle \mathbf{J}_s + \hat{\sigma} \mathbf{F}_W + \varepsilon_r \mathbf{F}_U + jk\varepsilon_r \mathbf{F}_W, \mathbf{v} \rangle, \quad (6.21a)$$

$$\dots = -j\sqrt{k} \langle \varepsilon_r \mathbf{F}_W, \mathbf{w} \rangle + \frac{1}{\sqrt{k}} \underbrace{\langle \text{div } \mathbf{J}_s, \psi_W \rangle - \langle \hat{\sigma} \mathbf{F}_W + \varepsilon_r \mathbf{F}_U, \mathbf{w} \rangle}_{=0}, \quad (6.21b)$$

$$\dots = -j \langle \varepsilon_r \mathbf{F}_W, \mathbf{u} \rangle + \frac{1}{k} \underbrace{\langle \text{div } \mathbf{J}_s, \psi_U \rangle - \langle \varepsilon_r \mathbf{F}_U, \mathbf{u} \rangle}_{=0}. \quad (6.21c)$$

The fully stabilized weak form BVP thus reads:

Find  $\mathbf{E}_V \in V$ ,  $\mathbf{E}_W \in W$ , and  $\mathbf{E}_U \in U$  such that

$$\begin{aligned} \langle \nu_r \text{curl } \mathbf{E}_V, \text{curl } \mathbf{v} \rangle + \alpha \langle \mathbf{E}_V, \mathbf{v} \rangle_{\Gamma_a} + j \langle \hat{\sigma}(\sqrt{k}\mathbf{E}_W + k\mathbf{E}_V), \mathbf{v} \rangle \\ - \langle \varepsilon_r(k\mathbf{E}_U + k^{\frac{3}{2}}\mathbf{E}_W + k^2\mathbf{E}_V), \mathbf{v} \rangle = - \langle \mathbf{J}_s + \hat{\sigma}\mathbf{F}_W + \varepsilon_r\mathbf{F}_U + jk\varepsilon_r\mathbf{F}_W, \mathbf{v} \rangle, \end{aligned} \quad (6.22a)$$

$$j \langle \hat{\sigma}(\mathbf{E}_W + \sqrt{k}\mathbf{E}_V), \mathbf{w} \rangle - \langle \varepsilon_r(\sqrt{k}\mathbf{E}_U + k\mathbf{E}_W + k^{\frac{3}{2}}\mathbf{E}_V), \mathbf{w} \rangle = -j\sqrt{k} \langle \varepsilon_r \mathbf{F}_W, \mathbf{w} \rangle, \quad (6.22b)$$

$$- \langle \varepsilon_r(\mathbf{E}_U + \sqrt{k}\mathbf{E}_W + k\mathbf{E}_V), \mathbf{u} \rangle = -j \langle \varepsilon_r \mathbf{F}_W, \mathbf{u} \rangle, \quad (6.22c)$$

for all  $\mathbf{v} \in V$ ,  $\mathbf{w} \equiv \text{grad } \psi_W \in W$ , and  $\mathbf{u} \equiv \text{grad } \psi_U \in U$ .

If the two terminals  $T_a$  and  $T_b$  connected by the source current density  $\mathbf{J}_s$  lie on the same conductor,  $\mathbf{F}_U$  is zero: The gradient field  $\mathbf{F}_U \in U$  is produced by a potential,  $\mathbf{F}_U = \text{grad } f_U$ , which must be constant on each of the  $n_c \geq 1$  disconnected conductors of the model. Thus, no potential difference can exist in this case between the locations of the two discrete excitations that (5.10) provides on the RHS of (6.19). If  $\mathbf{F}_U$  is zero, the electric field  $\mathbf{E}$  of (6.17) and hence the impedance  $Z$  do not diverge for  $k \rightarrow 0$  and can therefore be computed directly at the DC point  $k = 0$ .

The LF behavior of the system with diverging RHS (6.15) is compared to that of the system with stabilized RHS (6.21) using the example of the capacitor-coil model displayed

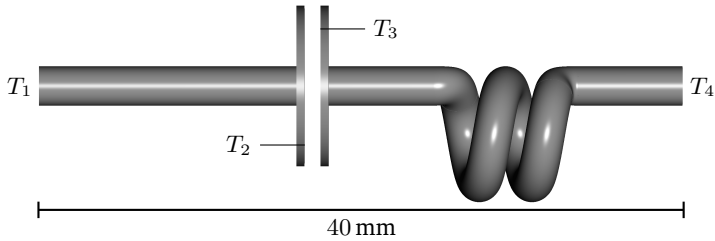


Figure 6.2.: [SKD22c] Capacitor-coil model with four terminals  $T_i$ . The conductivity is assumed to be  $\sigma = 5.7 \cdot 10^7$  S/m in the conductors. For simulations with an ABC boundary  $\partial\Omega = \Gamma_a$  the model is considered at the center of a spherical domain  $\Omega$  of radius  $r_b = 120$  mm meshed with 49000 tetrahedra. For simulations with an electric boundary  $\partial\Omega = \Gamma_{el}$  a box-shaped computational domain of dimensions  $240$  mm  $\times$   $212$  mm  $\times$   $210$  mm is meshed with 53000 tetrahedra. (© 2021 IEEE)

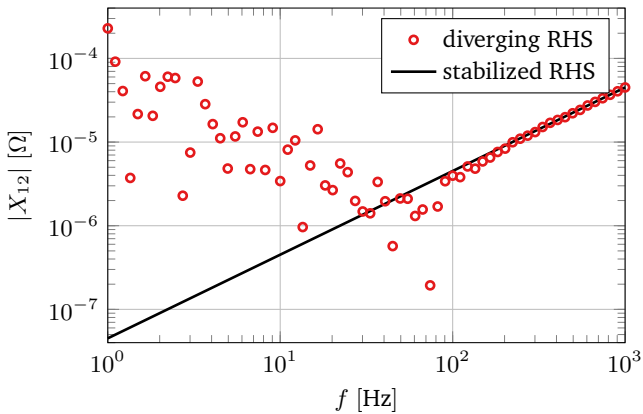


Figure 6.3.: [SKD22c] Modulus of the reactance  $X_{12}$  of the capacitor-coil model in the low-frequency regime. Whereas the values obtained with the stabilized RHS of (6.21) show the expected linear frequency dependency, the values of the system with diverging RHS (6.15) are strongly scattered for lower frequencies. (© 2021 IEEE)

in Fig. 6.2 with  $\partial\Omega = \Gamma_{\text{el}}$  (similar models are used in [Ell+17; HKO08]). A star topology  $\{(T_1, T_2), (T_1, T_3), (T_1, T_4)\}$  with reference terminal  $T_1$  is used to compute a  $3 \times 3$  nodal impedance matrix  $\mathbf{Z}_N$ . Whereas the main diagonal elements of  $\mathbf{Z}_N$  are stable also for the system with diverging RHS (6.15) (for frequencies  $f > 1$  Hz), this is not the case for some off-diagonal elements. Fig. 6.3 displays the modulus of the reactance  $X_{12} = \text{Im}([\mathbf{Z}_N]_{12})$ . The values obtained with the diverging RHS of (6.15) are strongly scattered for lower frequencies while the values produced with stabilized RHS (6.21) show the expected inductive (i.e., approximately linear) frequency dependence in the whole frequency interval.

### 6.3. Stable Computation of the Compensated Scalar Potential

By testing the Coulomb-gauged PDE (5.22a) with the functions of (6.3), a weak form of the BVP (5.22) determining the compensated ESP  $\phi_c$  is derived. Using (6.9) and the MBC (5.22c) and ABC (5.22d), the divergence term on the LHS of the equation becomes

$$-\langle \text{div}(\varepsilon_r \text{grad } \phi_c, \psi) \rangle = \langle \varepsilon_r \text{grad } \phi_c, \text{grad } \psi \rangle + \frac{1}{r} \langle \phi_c, \psi \rangle_{\Gamma_a}. \quad (6.23)$$

The  $\text{div } \mathbf{E}$  term on the RHS of (5.22a) is transformed analogously using (6.9) and the MBC (2.23),

$$\langle \text{div } \varepsilon_r \mathbf{E}, \psi \rangle = -\langle \varepsilon_r \mathbf{E}, \text{grad } \psi \rangle. \quad (6.24)$$

The boundary term that would occur on  $\Gamma_a$  is disregarded in this equation as it has a detrimental effect on the quality of the ABC results in numerical experiments. A possible explanation for this behavior is the prerequisite of the ABC discussed in Section A.1 that no sources of the field (i.e., here,  $\phi_c$ ) are allowed near the boundary  $\partial\Omega$ . A boundary term occurring on the RHS of the PDE can be understood as such a source. With (6.23) and (6.24) the weak form of the BVP (5.22) reads:

Find  $\phi_c \in H^1(\Omega)'$  such that

$$\langle \varepsilon_r \text{grad } \phi_c, \text{grad } \psi \rangle + \frac{2}{r} \langle \phi_c, \psi \rangle_{\Gamma_a} = -\langle \varepsilon_r \mathbf{E}, \text{grad } \psi \rangle + j\mu_0 ck \langle g, \psi \rangle \quad \forall \psi \in H^1(\Omega)'. \quad (6.25)$$

Using the Lorenz-gauged PDE (5.23) and the scalar absorbing BC (A.11) instead of the Coulomb-gauged PDE (5.22a) and the asymptotic BC (5.22d), the weak form BVP reads instead:

Find  $\phi_c \in H^1(\Omega)'$  such that

$$\langle \varepsilon_r \text{grad } \phi_c, \text{grad } \psi \rangle + \beta \langle \phi_c, \psi \rangle_{\Gamma_a} - k^2 \langle \phi_c, \psi \rangle = -\langle \varepsilon_r \mathbf{E}, \text{grad } \psi \rangle + j\mu_0 ck \langle g, \psi \rangle \quad \forall \psi \in H^1(\Omega)', \quad (6.26)$$

with  $\beta = jk + 2/r$ .

The weak-form BVP (6.25) does not possess a general LF breakdown. If the boundary is not purely magnetic,  $\partial\Omega \neq \Gamma_{\text{mag}}$ , the resulting system matrix always has full rank. If  $\partial\Omega = \Gamma_{\text{mag}}$ , the spatially constant component of  $\phi_c$  is undetermined as constant functions lie in the kernel of the gradient operator. However, a full-rank matrix is obtained by simply setting the potential to zero at an arbitrary position. Nevertheless, there are two cases that require a LF stabilization treatment: First, in the standard case that the electrostatic field  $\mathbf{F}_U$  is not zero when using the stabilized RHS discussed in Subsection 6.2.2 to compute  $\mathbf{E}$ . And second, in the non-standard case that the Lorenz-gauged BVP (6.26) is used to compute  $\phi_c$  for a purely magnetic boundary,  $\partial\Omega = \Gamma_{\text{mag}}$ . This case is relevant mainly for the Darwin system, whose LF stabilization is the topic of Subsection 6.4.2

### 6.3.1. Stabilizing the Right-Hand Side

If the system with stabilized RHS of section 6.2.2 is used for the computation of  $\mathbf{E}$ , a stabilization of the RHS of the BVP determining  $\phi$  becomes necessary to harness the stabilized values of  $\mathbf{E}$  in the impedance computation. The electrostatic field  $\mathbf{F}_U$  in the stable expression of  $\mathbf{E}$  (6.17) yields a term diverging for  $k \rightarrow 0$  on the RHS of (6.25). This diverging term is easily eliminated by considering the scalar potential  $f_U$ , that produces the electrostatic gradient field  $\mathbf{F}_U = \text{grad } f_U$ , in a split of the compensated ESP  $\phi_c$ ,

$$\phi_c = j\mu_0 c \left( \phi'_c + \frac{1}{k} f_U \right). \quad (6.27)$$

The condition of (6.11c) demanding that  $\hat{\mathbf{n}} \times \mathbf{F}_U$  vanishes on the ABC boundary  $\Gamma_a$  is realized by setting  $f_U = 0$  on  $\Gamma_a$  in order to simplify the following stabilization. Inserting the split (6.27) and the stable  $\mathbf{E}$  expression (6.17) into (6.25) yields an BVP without diverging RHS for the non-static compensated ESP  $\phi'_c$ :

Find  $\phi'_c \in H^1(\Omega)'$  such that

$$\begin{aligned} \langle \varepsilon_r \text{grad } \phi'_c, \text{grad } \psi \rangle + \frac{2}{r} \langle \phi_c, \psi \rangle_{\Gamma_a} = & - \langle \varepsilon_r (k\mathbf{E}_V + \sqrt{k}\mathbf{E}_W + \mathbf{E}_U - j\mathbf{F}_W), \text{grad } \psi \rangle \\ & + k \langle g + f_U, \psi \rangle \quad \forall \psi \in H^1(\Omega)'. \end{aligned} \quad (6.28)$$

### 6.3.2. Stabilizing the Lorenz-gauged system matrix for magnetic boundaries

Both the Coulomb-gauged BVP (6.25) and Lorenz-gauged BVP (6.26) yield system matrices with full rank at all frequencies if the boundary is not purely magnetic, i.e., if  $\partial\Omega \neq \Gamma_{\text{mag}}$ . For the Coulomb-gauged BVP, the rank deficiency of 1 that occurs if  $\partial\Omega = \Gamma_{\text{mag}}$  can be eliminated by simply setting  $\phi_c$  to zero somewhere in  $\Omega$ , thereby fixing the previously undetermined spatially constant component of  $\phi_c$ . This is realized by limiting the Sobolev

space of  $\phi_c$  and the test functions  $\psi$  in (6.25) to the space  $H_f^1(\Omega) \subset H^1(\Omega)$  of functions fixed to zero at one point  $\mathbf{x}_f \in \Omega$ ,

$$H_f^1(\Omega) := \{\psi \in H^1(\Omega) : \psi(\mathbf{x}_f) = 0\}. \quad (6.29)$$

The zero point  $\mathbf{x}_f$  is typically chosen to lie on the boundary  $\partial\Omega$ .

For the Lorenz-gauge BVP (6.26) the spatially constant component of  $\phi_c$  is not arbitrary if  $\partial\Omega = \Gamma_{\text{mag}}$  due to the “mass term”  $\propto k^2$  in the equation. The vanishing of this term for  $k \rightarrow 0$ , however, causes a minor LF breakdown: The system matrix still exhibits a rank deficiency of 1 at low frequencies. Whereas this poses no difficulty for iterative solvers, this problem still has to be treated to enable the use of a direct solver.

The stabilization follows an analogous approach as for the E-field formulation in Section 6.2, albeit much less complex. The Sobolev space  $H^1(\Omega)$  is decomposed into the space  $H_f^1(\Omega)$  of functions fixed to zero at  $\mathbf{x}_f$  and the space of functions constant in  $\Omega$  (i.e., simply the set of complex numbers  $\mathbb{C}$ ):

$$H^1(\Omega) = H_f^1(\Omega) \oplus \mathbb{C}. \quad (6.30)$$

Expressing the compensated ESP  $\phi_c$  as

$$\phi_c = j\mu_0 c (\phi_v + \frac{1}{k} \phi_0) \quad (6.31)$$

with the spatially variable part  $\phi_v \in H_f^1(\Omega)$  and the constant part  $\phi_0 \in \mathbb{C}$ , a stabilized version of the weak formulation (6.25) is gained by testing with all functions  $\psi \in H_f^1(\Omega)$  and a single constant function  $1 \in \mathbb{C}$ :

Find  $\phi_v \in H_f^1(\Omega)$  and  $\phi_0 \in \mathbb{C}$  such that

$$\begin{aligned} \langle \varepsilon_r \text{grad } \phi_v, \text{grad } \psi \rangle - k \langle \phi_0, \psi \rangle - k^2 \langle \phi_v, \psi \rangle \\ = -\frac{1}{j\mu_0 c} \langle \varepsilon_r \mathbf{E}, \text{grad } \psi \rangle + k \langle g, \psi \rangle \quad \forall \psi \in H_f^1(\Omega), \end{aligned} \quad (6.32a)$$

$$- \langle \phi_0, 1 \rangle - k \langle \phi_v, 1 \rangle = \langle g, 1 \rangle. \quad (6.32b)$$

The resulting system matrix is still symmetric but less sparse than that of (6.25) due to the dense contributions of the terms  $\langle \phi_0, \psi \rangle$  and  $\langle \phi_v, 1 \rangle$ .

In the case of  $\mathbf{F}_U \neq 0$  discussed in the previous subsection, the split of (6.31) has to be combined with the split of (6.27), which yields the expression

$$\phi_c = j\mu_0 c \left( \phi_v + \frac{1}{k} \phi_0 + \frac{1}{k} f_U \right). \quad (6.33)$$

The weak-form BVP resulting from the combined split (6.33) reads simply:

Find  $\phi_v \in H_f^1(\Omega)$  and  $\phi_0 \in \mathbb{C}$  such that

$$\begin{aligned} \langle \varepsilon_r \text{grad } \phi_v, \text{grad } \psi \rangle - k \langle \phi_0, \psi \rangle - k^2 \langle \phi_v, \psi \rangle &= k \langle g + f_U, \psi \rangle \\ - \langle \varepsilon_r (k \mathbf{E}_V + \sqrt{k} \mathbf{E}_W + \mathbf{E}_U - j \mathbf{F}_W), \text{grad } \psi \rangle &\quad \forall \psi \in H_f^1(\Omega), \end{aligned} \quad (6.34a)$$

$$- \langle \phi_0, 1 \rangle - k \langle \phi_v, 1 \rangle = \langle g + f_U, 1 \rangle. \quad (6.34b)$$

## 6.4. Quasistatic Approximations

One of the advantages of Eller et al.'s LF stabilization approach already listed in Section 6.1 is that its fundamental splitting of the Sobolev space  $H(\text{curl})$  makes it directly applicable also to quasistatic approximations and the PEC case. Moreover, the splitting enables to exclude those parts of  $H(\text{curl})$  that are not needed in the considered case, thereby minimizing the number of DoFs, and revealing that some formulations used by other authors can be understood as special cases in the general approach of [Ell+17].

### 6.4.1. MQS system

In weak form the MQS BVP (5.24) reads (analogously to the full-wave weak form (6.8)):

Find  $\mathbf{E} \in H(\text{curl}, \Omega)'$  such that

$$\langle \nu_r \text{curl } \mathbf{E}, \text{curl } \mathbf{f} \rangle + \frac{1}{r} \langle \mathbf{E}_t, \mathbf{f} \rangle_{\Gamma_a} + jk \langle \hat{\sigma} \mathbf{E}, \mathbf{f} \rangle = -j\mu_0 c k \langle \mathbf{J}_s, \mathbf{f} \rangle \quad \forall \mathbf{f} \in H(\text{curl}, \Omega)'. \quad (6.35)$$

As the displacement current is neglected entirely in the MQS approximation, only the curl term remains in the non-conducting domain  $\Omega_0$  in (6.35). Therefore, no functions of the space  $U$  (6.12c) of gradient fields with support in  $\Omega_0$  must be considered in the LF stabilized form of the BVP. The electric field  $\mathbf{E}$  can be expressed with only the non-static fields  $\mathbf{E}_V \in V$  and  $\mathbf{E}_W \in W$ , and the static current field  $\mathbf{F}_W \in W$  (determined by (6.20) for  $F_U = 0$ ) as

$$\mathbf{E} = j\mu_0 c (k \mathbf{E}_V + \sqrt{k} \mathbf{E}_W - j \mathbf{F}_W). \quad (6.36)$$

The LF stabilized form of (6.35) thus reads:

Find  $\mathbf{E}_V \in V$  and  $\mathbf{E}_W \in W$  such that

$$\langle \nu_r \text{curl } \mathbf{E}_V, \text{curl } \mathbf{v} \rangle + \frac{1}{r} \langle \mathbf{E}_V^t, \mathbf{v} \rangle_{\Gamma_a} + j \langle \hat{\sigma} (\sqrt{k} \mathbf{E}_W + k \mathbf{E}_V), \mathbf{v} \rangle \quad (6.37a)$$

$$= - \langle \mathbf{J}_s + \hat{\sigma} \mathbf{F}_W, \mathbf{v} \rangle \quad \forall \mathbf{v} \in V,$$

$$j \langle \hat{\sigma} (\mathbf{E}_W + \sqrt{k} \mathbf{E}_V), \mathbf{w} \rangle = 0 \quad \forall \mathbf{w} \in W. \quad (6.37b)$$

The system matrix resulting from a FE discretization of (6.37) is not only symmetric but also significantly smaller than that of the full-wave BVP (6.15), as it only uses functions

from  $V$  and  $W$ . If the considered source current density  $\mathbf{J}_s$  were divergence free (and hence  $\mathbf{F}_W = 0$ ), the weak-form BVP (6.37) would be exactly equivalent to the one formulated in [Kli15], where also the same ABC is considered.

There are two feasible alternatives to the electric field split of (6.36). The expression  $\mathbf{E} = j\mu_0 c(k\mathbf{E}_V + \mathbf{E}_W)$ , closely resembling an  $\mathbf{A}$ - $\phi$  potential formulation, also leads to a stable system, that makes a computation of  $\mathbf{F}_W$  unnecessary. However, its system matrix is non-symmetric. The second alternative expression  $\mathbf{E} = j\mu_0 c(k\mathbf{E}_V + \sqrt{k}\mathbf{E}_W)$  stabilizes only the system matrix. It yields analogously to (6.15) a symmetric system with a term  $\propto k^{-\frac{1}{2}}$  on its RHS, which reads:

Find  $\mathbf{E}_V \in V$  and  $\mathbf{E}_W \in W$  such that

$$\langle \nu_r \operatorname{curl} \mathbf{E}_V, \operatorname{curl} \mathbf{v} \rangle + \frac{1}{r} \langle \mathbf{E}_V^t, \mathbf{v} \rangle_{\Gamma_a} + j \langle \hat{\sigma}(\sqrt{k}\mathbf{E}_W + k\mathbf{E}_V), \mathbf{v} \rangle = - \langle \mathbf{J}_s, \mathbf{v} \rangle \quad \forall \mathbf{v} \in V, \quad (6.38a)$$

$$j \langle \hat{\sigma}(\mathbf{E}_W + \sqrt{k}\mathbf{E}_V), \mathbf{w} \rangle = \frac{1}{\sqrt{k}} \langle \operatorname{div} \mathbf{J}_s, \psi_W \rangle \quad \forall \mathbf{w} \equiv \operatorname{grad} \psi_W \in W. \quad (6.38b)$$

While this system cannot be evaluated at the DC point  $k = 0$ , for most models it still produces stable results for frequencies as low as  $f = 1$  Hz. This weak form is used in the sensitivity analysis of Chapter 8 in order not to complicate the sensitivity computation with terms that would result from the static current field  $\mathbf{F}_W$  if the first formulation (6.37) were used.

#### 6.4.2. Darwin system

A symmetric but not LF stable weak form of the Darwin BVP (5.25) valid for  $\Gamma_a = \emptyset$  can be formulated using a frequency-scaled electric field  $\mathbf{E}' := k\mathbf{E}$ :

Find  $\mathbf{E}' \in H(\operatorname{curl})$  and  $\phi_c \in H^1(\Omega)'$  such that

$$\langle \nu_r \operatorname{curl} \mathbf{E}', \operatorname{curl} \mathbf{f} \rangle + j \langle \hat{\sigma} \mathbf{E}', \mathbf{f} \rangle + k \langle \varepsilon_r \operatorname{grad} \phi_c, \mathbf{f} \rangle = -j\mu_0 c \langle \mathbf{J}_s, \mathbf{f} \rangle, \quad (6.39a)$$

$$\langle \varepsilon_r \operatorname{grad} \phi_c, \operatorname{grad} \psi \rangle - k^2 \langle \phi_c, \psi \rangle + k \langle \varepsilon_r \mathbf{E}', \operatorname{grad} \psi \rangle = j\mu_0 c k \langle g, \psi \rangle, \quad (6.39b)$$

for all  $\mathbf{f} \in H(\operatorname{curl}, \Omega)'$  and  $\psi \in H^1(\Omega)'$ .

An LF stabilized version of (6.39) is found by inserting the LF stable expressions of the electric field  $\mathbf{E}$  (6.17) and the compensated ESP  $\phi_c$  (6.27) into (5.25) and testing with the functions of the respective Sobolev spaces. This yields the variational problem:

Find  $\mathbf{E}_V \in V$ ,  $\mathbf{E}_W \in W$ ,  $\mathbf{E}_U \in U$ , and  $\phi'_c \in H^1(\Omega)'$  such that

$$\begin{aligned} \langle \nu_r \operatorname{curl} \mathbf{E}_V, \operatorname{curl} \mathbf{v} \rangle + j \langle \hat{\sigma}(\sqrt{k} \mathbf{E}_W + k \mathbf{E}_V), \mathbf{v} \rangle + k \langle \varepsilon_r \operatorname{grad} \phi'_c, \mathbf{v} \rangle \\ = - \langle \mathbf{J}_s + \hat{\sigma} \mathbf{F}_W + \varepsilon_r \operatorname{grad} f_U, \mathbf{v} \rangle \quad \forall \mathbf{v} \in V, \end{aligned} \quad (6.40a)$$

$$j \langle \hat{\sigma}(\mathbf{E}_W + \sqrt{k} \mathbf{E}_V) + \sqrt{k} \varepsilon_r \operatorname{grad} \phi'_c, \mathbf{w} \rangle = 0 \quad \forall \mathbf{w} \in W, \quad (6.40b)$$

$$\langle \varepsilon_r \operatorname{grad} \phi'_c, \mathbf{u} \rangle = 0 \quad \forall \mathbf{u} \in U, \quad (6.40c)$$

$$\begin{aligned} \langle \varepsilon_r(\mathbf{E}_U + \sqrt{k} \mathbf{E}_W + k \mathbf{E}_V + \operatorname{grad} \phi'_c), \operatorname{grad} \psi \rangle - k^2 \langle \phi'_c, \psi \rangle \\ = k \langle g + f_U, \psi \rangle + j \langle \mathbf{F}_W, \operatorname{grad} \psi \rangle \quad \forall \psi \in H^1(\Omega)'. \end{aligned} \quad (6.40d)$$

Again, the resulting system matrix is symmetric.

In case of a purely magnetic boundary,  $\partial\Omega = \Gamma_a$ , the compensated ESP  $\phi_c$  must be split with (6.33) instead, yielding a slightly different weak-form BVP:

Find  $\mathbf{E}_V \in V$ ,  $\mathbf{E}_W \in W$ ,  $\mathbf{E}_U \in U$ ,  $\phi_v \in H_f^1(\Omega)$ , and  $\phi_0 \in \mathbb{C}$  such that

$$\begin{aligned} \langle \nu_r \operatorname{curl} \mathbf{E}_V, \operatorname{curl} \mathbf{v} \rangle + j \langle \hat{\sigma}(\sqrt{k} \mathbf{E}_W + k \mathbf{E}_V), \mathbf{v} \rangle + k \langle \varepsilon_r \operatorname{grad} \phi_v, \mathbf{v} \rangle \\ = - \langle \mathbf{J}_s + \hat{\sigma} \mathbf{F}_W + \varepsilon_r \operatorname{grad} f_U, \mathbf{v} \rangle \quad \forall \mathbf{v} \in V, \end{aligned} \quad (6.41a)$$

$$j \langle \hat{\sigma}(\mathbf{E}_W + \sqrt{k} \mathbf{E}_V) + \sqrt{k} \varepsilon_r \operatorname{grad} \phi_v, \mathbf{w} \rangle = 0 \quad \forall \mathbf{w} \in W, \quad (6.41b)$$

$$\langle \varepsilon_r \operatorname{grad} \phi_v, \mathbf{u} \rangle = 0 \quad \forall \mathbf{u} \in U, \quad (6.41c)$$

$$\begin{aligned} \langle \varepsilon_r(\mathbf{E}_U + \sqrt{k} \mathbf{E}_W + k \mathbf{E}_V + \operatorname{grad} \phi_v), \operatorname{grad} \psi \rangle - \langle k \phi_0 + k^2 \phi_v, \psi \rangle \\ = k \langle g + f_U, \psi \rangle + j \langle \mathbf{F}_W, \operatorname{grad} \psi \rangle \quad \forall \psi \in H_f^1(\Omega)', \end{aligned} \quad (6.41d)$$

$$- \langle \phi_0, 1 \rangle - k \langle \phi_v, 1 \rangle = \langle g + f_U, 1 \rangle. \quad (6.41e)$$

## 6.5. Perfect Electric Conductor Case

In the PEC case discussed in Section 5.3 the PDE (5.26a) determining  $\mathbf{E}$  is enforced only in the non-conducting subdomain  $\Omega_0 = \Omega \setminus \Omega_c$ . The conductors are considered in the simulation by enforcing the EBC (5.26b) of the outer electric boundary  $\Gamma_{el}$  also on the boundary  $\partial\Omega_c$  of the conducting domain. Thus, the Sobolev space  $H(\operatorname{curl}, \Omega_0)'$  for  $\mathbf{E}$  in the PEC case is significantly smaller than  $H(\operatorname{curl}, \Omega)'$ ,

$$H(\operatorname{curl}, \Omega_0)' := \{ \mathbf{f} \in H(\operatorname{curl}, \Omega) : \mathbf{f} = 0 \text{ on } \tilde{\Gamma}_{el} \}. \quad (6.42)$$

with  $\tilde{\Gamma}_{el} := \partial\Omega_c \cup \Gamma_{el}$  being the entire electric boundary.

An LF stable splitting of  $H(\operatorname{curl}, \Omega_0)'$  only needs two subspaces,

$$H(\operatorname{curl}, \Omega_0)' = \tilde{V} \oplus U, \quad (6.43a)$$

$$\forall \mathbf{v} \in \tilde{V} \quad \langle \operatorname{curl} \mathbf{v}, \operatorname{curl} \mathbf{v} \rangle \neq 0 \vee \langle \hat{\mathbf{n}} \times \mathbf{v}, \hat{\mathbf{n}} \times \mathbf{v} \rangle_{\Gamma_a} \neq 0 \quad (6.43b)$$

$$U := \{ \mathbf{u} \in H(\operatorname{curl}, \Omega_0)' : \operatorname{curl} \mathbf{u} = 0 \} \quad (6.43c)$$

A subsequent gradient-space splitting is not necessary as the conducting domain  $\Omega_c$  is disregarded. The splitting (6.43) of  $H(\text{curl}, \Omega_0)'$  is therefore equivalent to an  $\mathbf{A}$ - $\phi$  potential approach. Whereas the space  $\tilde{V}$  is smaller than the space  $V$  of (6.11), the space  $U$  of (6.43c) is identical to the space defined in (6.12b).

The electric field is thus expressed analogously to (6.17) with the functions  $\mathbf{E}_V \in \tilde{V}$  and  $\mathbf{E}_U \in U$ , and the electrostatic field  $\mathbf{F}_U = \text{grad } f_U \in U$  of (6.19),

$$\mathbf{E} = j\mu_0 c \left( k\mathbf{E}_V + \mathbf{E}_U - \frac{1}{k}\mathbf{F}_U \right). \quad (6.44)$$

Inserting this expression into the full-wave PEC case BVP (5.26) and testing with the relevant functions yields a much simpler weak form than that of the lossy case (6.22):

Find  $\mathbf{E}_V \in \hat{V}$ , and  $\mathbf{E}_U \in U$  such that

$$\langle \nu_r \text{curl } \mathbf{E}_V, \text{curl } \mathbf{v} \rangle - \langle \varepsilon_r (k\mathbf{E}_U + k^2\mathbf{E}_V), \mathbf{v} \rangle = - \langle \mathbf{J}_s + \varepsilon_r \mathbf{F}_U, \mathbf{v} \rangle \quad \forall \mathbf{v} \in \hat{V}, \quad (6.45a)$$

$$- \langle \varepsilon_r (\mathbf{E}_U + \sqrt{k}\mathbf{E}_W + k\mathbf{E}_V), \mathbf{u} \rangle = 0 \quad \forall \mathbf{u} \in U. \quad (6.45b)$$

If the source current density  $\mathbf{J}_s$  were divergence-free (and hence  $\mathbf{F}_U = 0$ ), the formulation (6.45) would be equivalent to the one used in [JFD15] in the non-conducting domain. The weak-form BVP (6.28) to stably compute  $\phi_c$  from  $\mathbf{E}$  remains unchanged (in the PEC case,  $\mathbf{E}_W = \mathbf{F}_W = 0$  on the RHS of (6.28)).

As discussed in Subsection 5.3.1, considering the PEC case in the MQS approximation yields the frequency-independent MS system (5.28). Disregarding the displacement current while only considering the conducting domain, the electric field of (5.28) lies fully in the space  $\tilde{V}$

$$\mathbf{E} = j\mu_0 \omega \mathbf{E}_V \in \tilde{V}. \quad (6.46)$$

Inserting this expression into (5.28) and testing with  $\mathbf{v} \in \tilde{V}$  yields the weak formulation:

Find  $\mathbf{E}_V \in \tilde{V}$  such that

$$\langle \nu_r \text{curl } \mathbf{E}_V, \text{curl } \mathbf{v} \rangle = - \langle \mathbf{J}_s, \mathbf{v} \rangle \quad \forall \mathbf{v} \in \tilde{V}. \quad (6.47)$$

A weak form of the BVP (5.29) for the frequency-scaled ESP  $\vartheta$  is obtained by merely scaling the weak-form BVP (6.25) for  $\phi_c$  with the factor  $(j\mu_0 \omega)^{-1}$ .

For the PEC case Darwin BVP (5.31) a stabilized weak form is obtained by using (6.44) to split  $\mathbf{E}$  as for the full wave system, and either (6.33) or (6.28) to split  $\phi_c$ , depending on whether the boundary is fully magnetic,  $\partial\Omega = \Gamma_{\text{mag}}$ , or not. For the simpler case  $\partial\Omega \neq \Gamma_{\text{mag}}$ , the resulting weak-form BVP is analogous to (6.40):

Find  $\mathbf{E}_V \in \widehat{V}$ ,  $\mathbf{E}_U \in U$ , and  $\phi'_c \in H^1(\Omega)'$  such that

$$\langle \nu_r \operatorname{curl} \mathbf{E}_V, \operatorname{curl} \mathbf{v} \rangle + k \langle \varepsilon_r \operatorname{grad} \phi'_c, \mathbf{v} \rangle = - \langle \mathbf{J}_s + \varepsilon_r \operatorname{grad} f_U, \mathbf{v} \rangle \quad \forall \mathbf{v} \in \widehat{V}, \quad (6.48a)$$

$$\langle \varepsilon_r \operatorname{grad} \phi'_c, \mathbf{u} \rangle = 0 \quad \forall \mathbf{u} \in U, \quad (6.48b)$$

$$\langle \varepsilon_r (\mathbf{E}_U + k \mathbf{E}_V + \operatorname{grad} \phi'_c), \operatorname{grad} \psi \rangle - k^2 \langle \phi'_c, \psi \rangle = k \langle g + f_U, \psi \rangle \quad \forall \psi \in H^1(\Omega)'. \quad (6.48c)$$

The PEC case BVP for purely magnetic boundaries  $\partial\Omega = \Gamma_{\text{mag}}$  follows from (6.41) in the same way and is not stated explicitly.

## 6.6. Constructing the Finite-Dimensional Sobolev Spaces

As discussed in Chapter 3, the FEM discretizes variational problems by replacing the relevant Sobolev space  $X$  of trial and test functions with a finite-dimensional subspace  $X_h \subset X$ , that is constructed with  $X$ -conforming finite elements. The FE subspaces  $P'_h \subset H^1(\Omega)'$  and  $Q'_h \subset H(\operatorname{curl}, \Omega)'$  can readily be constructed using the  $H^1$ -conforming and  $H(\operatorname{curl})$ -conforming elements provided in [Ing06]. The construction of the FE subspaces of the Sobolev spaces  $V$ ,  $W$ , and  $U$  of the LF stabilization, however, requires discussion.

### 6.6.1. Tree-cotree splitting

In the context of the Helmholtz-type decomposition (6.11) of  $H(\operatorname{curl}, \Omega)'$  into a space  $V$  of functions with non-vanishing curl and a space of gradient fields  $Y$ , the construction of the FE subspace  $Y_h \subset Y$  is trivial. It is realized by simply applying the gradient operator to the functions of  $P'_h$

$$Y_h = \operatorname{grad} P'_h. \quad (6.49)$$

The construction of a FE space  $V_h \subset V$ , however, requires a tree-cotree splitting, originally proposed in a seminal paper by Albanese and Rubinacci [AR88]. The idea of this method is to eliminate specific basis functions of  $Q_h \subset H(\operatorname{curl}, \Omega)$  such that the remaining functions cannot express any pure gradient fields while at the same time still constituting a basis for all vector fields with closed field lines. An appropriate elimination scheme is only required for the lowest order  $p = 1$  basis functions of  $Q_h$ , as the higher order basis functions of [Ing06] are already naturally divided into gradient fields and functions with non-vanishing curl. As discussed in Subsection 3.2.2 each of the  $p = 1$  basis functions is associated with one edge of the FE mesh of the domain  $\Omega$ . This fact gives rise to the tree-cotree approach.

Considering the nodes and edges of the mesh as constituting a graph, a spanning tree and corresponding cotree can be constructed from the mesh, e.g., using Kruskal's algorithm [Kru56] (basic concepts of graph theory are discussed in Subsection 4.2.1). The basis functions associated with the spanning tree's edges form a basis for the pure gradient fields because they connect all mesh nodes. Conversely, adding a cotree edge to the tree closes

one of the fundamental loops of the graph. The tree basis functions, however, describing gradient fields, lie in the kernel of the curl operator; any line integral along the loop is thus, due to Stokes theorem (2.3), equal to the line integral along the cotree edge. Hence, exactly those  $p = 1$  basis functions associated with the cotree contribute to the basis of  $V_h \in V$ .

The construction of a spanning tree for the purpose of a Helmholtz-type decomposition must respect the BCs imposed on the boundary  $\partial\Omega$  of the computational domain. An appropriate treatment for the boundary of (5.1), that is split into a magnetic, electric and ABC part, is provided in [Kli15]. Whereas magnetic boundaries  $\Gamma_{\text{mag}}$  do not require any special consideration in the construction of the tree, the EBC (2.19) demands that the DoFs associated with the edges on  $\Gamma_{\text{el}}$  are set to zero. Moreover, the basis functions associated with the edges on the ABC boundary  $\Gamma_a$  must be part of  $V_h$  due to (6.11b). Because of these requirements, the edges of  $\Gamma_{\text{el}}$  and  $\Gamma_a$  must be associated with the tree. For each disconnected part  $\Gamma_i \subseteq \Gamma_{\text{el}} \cup \Gamma_a$  of the affected boundary, compatibility with the rest of the tree must be ensured by mapping all mesh nodes  $\in \Gamma_i$  onto one single vertex  $v_i$  in the graph.

In the PEC case of section 6.5, where the domain of the  $\mathbf{E}$  computation is the non-conducting domain  $\Omega_0$ , the surface of each individual conductor of the model constitutes such a disconnected boundary. For a total number of  $n_\gamma$  disconnected parts, i.e.,

$$\partial\Omega_c \cup \Gamma_{\text{el}} \cup \Gamma_a = \bigcup_{i=0}^{n_\gamma} \Gamma_i \quad \text{with } \Gamma_i \cap \Gamma_j = \emptyset \text{ for } i \neq j. \quad (6.50)$$

In the general lossy case, when the extraction is to be executed at high frequencies where the skin effect leads to a vanishing of  $\mathbf{E}$  in the conductor interiors, numerical artifacts can arise if in the non-conducting domain  $\Omega_0$  the tree would not be equivalent to a PEC case tree that contains only one vertex  $v_i$  per disconnected boundary  $\Gamma_i$  of (6.50). The problem is avoided by first constructing a tree in  $\Omega_0$  respecting the boundaries of (6.50) and subsequently adding the edges of trees constructed in the individual conductors.

## 6.6.2. Gradient-space splitting

Equally trivial as the construction of  $Y_h = \text{grad } P'_h$  is the task of finding a basis for the finite-dimensional subspace  $W_h \subset W$  of gradient fields that do not vanish in the conducting domain  $\Omega_c$ , which is required to implement the gradient-space decomposition (6.12). It suffices to just select those basis functions of  $Y_h$  that are associated with mesh nodes and edges (and in orders  $p > 2$  also faces and cells) that lie in  $\Omega_c$  (including the boundary  $\partial\Omega_c$ ). Constructing the FE subspace  $U_h \subset U$  of gradient fields that vanish in  $\Omega_c$  with the scalar basis function of  $P'_h$  is slightly more involved. The definition of  $U$  (6.12c) requires  $\forall \mathbf{u} \in U \mathbf{u} = 0$  in  $\Omega_c$ . Hence, any potential  $\psi_u \in P'_h$  producing a gradient field  $\mathbf{u} = \text{grad } \psi_u \in U_h$  must take a constant value  $c_i$  on each of the  $n_c \geq 1$  disconnected conducting subdomains  $\Omega_{c,i}$  (with  $\cup_i \Omega_{c,i} = \Omega_c$ ), as well as the on any disconnected parts

of the electric and ABC boundaries  $\Gamma_{\text{el}}$  and  $\Gamma_{\text{a}}$ . The total number of these constants is thus equivalent to  $n_\gamma$  of (6.50). The first constant can be chosen zero, and all  $n_\gamma - 1$  others must become DoFs in the linear system resulting from a FE discretization of (6.22).

This can be achieved by first discretizing (6.22) with the basis functions of  $Y_h = \text{grad } P'_h$ , thereby setting all DoFs of the first disconnected entity (conductor or outer boundary) to zero. All higher-order DoFs of the  $n_\gamma - 1$  other entities are set to zero as well, since first order elements are already sufficient to describe the constant values required on these entities. Subsequently, the first-order DoFs of each of the remaining entities are mapped onto a single DoF using a linear transformation. Discretizing (6.22) with the relevant basis functions of  $Y_h$  yields the system matrix  $\hat{\mathbf{A}}$  and the RHS vector  $\hat{\mathbf{b}}$ , which do not yet enforce the condition that the elements of  $U_h$  must vanish on the conductors. The correct linear system respecting the condition is then given by

$$\mathbf{A}\mathbf{x} = \mathbf{b} \quad \text{with } \mathbf{A} = \mathbf{P}\hat{\mathbf{A}}\mathbf{P}^\top, \mathbf{b} = \mathbf{P}\hat{\mathbf{b}}. \quad (6.51)$$

Here,  $\mathbf{x}$  is the vector of DoFs, and  $\mathbf{A}$  and  $\mathbf{b}$  are the transformed system matrix and RHS vector, respectively. The matrix  $\mathbf{P}$  maps every element of  $\hat{\mathbf{A}}$  and  $\hat{\mathbf{b}}$  associated with one of the relevant first order DoFs onto one of  $n_\gamma - 1$  elements in the transformed quantities  $\mathbf{A}$  and  $\mathbf{b}$ . The solution can be expressed with basis functions of  $\text{grad } P'_h$  by calculating the DoF vector  $\hat{\mathbf{x}}$  of this space with the reverse transformation  $\hat{\mathbf{x}} = \mathbf{P}^\top \mathbf{x}$ . For a system in which the second to fourth elements of  $\hat{\mathbf{x}}$  are DoFs associated with mesh nodes of the first conductor, the mapping would be

$$\mathbf{P} = \begin{pmatrix} 1 & 0 & 0 & 0 & 0 & \dots \\ 0 & 1 & 1 & 1 & 0 & \dots \\ 0 & 0 & 0 & 0 & 1 & \dots \\ & & \vdots & & & \ddots \end{pmatrix}. \quad (6.52)$$

## 6.7. Numerical Results

The efficacy of the proposed LF stable discretization scheme is demonstrated in a numerical experiment by comparison to values obtained with conventional discretizations. The Intel MKL PARDISO direct sparse solver used to solve the FE linear systems is configured such that it still produces a result even if the system matrix is singular, in order to obtain LF results also for the unstable systems. This is achieved by replacing any zero pivot elements encountered in the factorization of the matrix by small deltas and subsequently using an iterative refinement during the solution process. All results discussed in this section are obtained with the capacitor-coil model of Fig. 6.2, except for the performance comparison of Table 6.1.

Fig. 6.4 displays the LF behavior of the impedance  $Z$  between the terminals  $T_1$  and  $T_4$  as magnitude and phase for the LF stabilized full-wave BVP (6.22) and Darwin BVP (6.40) of

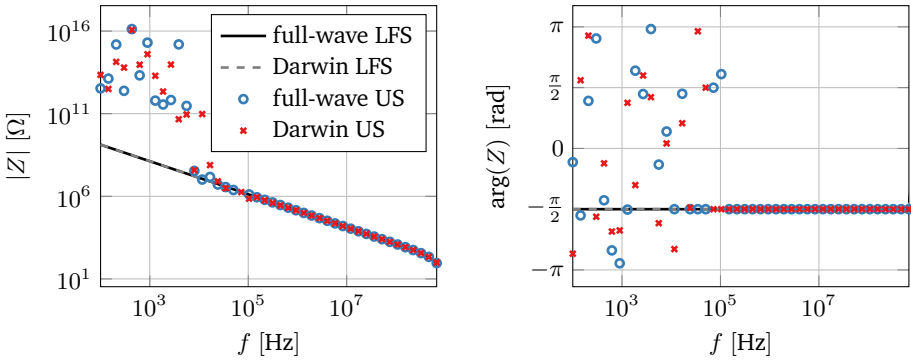


Figure 6.4.: Magnitude and phase of the impedance  $Z$  between terminals  $T_1$  and  $T_4$  of the model of Fig. 6.2 in a LF regime with  $\partial\Omega = \Gamma_{el}$ , obtained both with the LF stable (LFS) full-wave BVP (6.22) and Darwin BVP (6.40) and with the unstable (US) BVPs (6.8) and (6.39). The values of the unstable systems are strongly scattered for frequencies below 300 kHz.

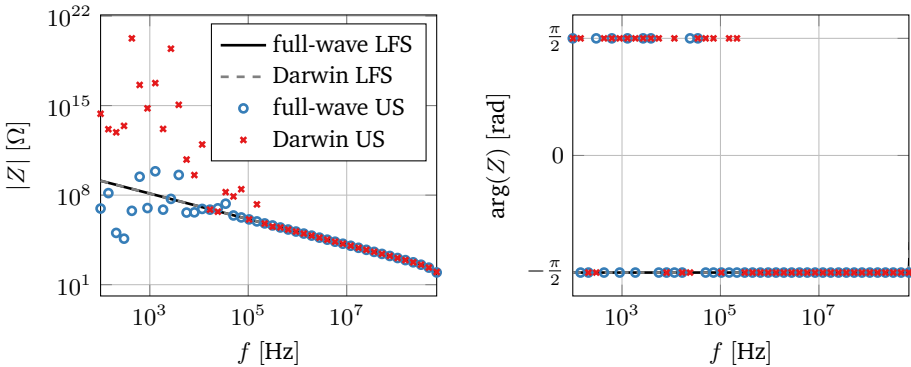


Figure 6.5.: Same plot as Fig. 6.4 but using the PEC case BVPs (6.45) and (6.48).

the general lossy case, compared to values obtained with the unstable full-wave BVP (6.8) and Darwin BVP (6.39) (MQS values are not provided as the MQS approximation cannot be used to compute the impedance between terminals on separate conductors). The unstable systems exhibit a strong instability for frequencies below 100 kHz whereas the stabilized systems remain stable in the whole frequency interval. Fig. 6.5 shows a similar behavior for the stabilized PEC case BVPs (6.45) and (6.48), and unstable versions of (5.26) and (5.31).

Fig. 6.6 provides an example for the difference in the electric field  $\mathbf{E}$  obtained with the stable full-wave BVP (6.22) and the unstable BVP (6.8) at  $f = 5$  kHz, using an electric boundary  $\partial\Omega = \Gamma_{el}$ . The figure exemplifies that, in contrast to the stabilized BVP, the unstable BVP yields implausible field distributions at low frequencies.

Fig. 6.7 displays the high-frequency impedance behavior of the same port  $(T_1, T_4)$ , obtained with the LF stabilized full-wave BVP (6.22) and the non-stabilized BVP (6.8) for an ABC boundary  $\partial\Omega = \Gamma_a$ . The values of both BVPs are virtually identical, which shows that the LF stabilized system yields accurate values also at high frequencies, and hence no switching of systems is necessary.

The MQS approximation can be used to compute the impedance between terminals that lie on the same conductor. Fig. 6.8 shows the frequency dependence of the resistance  $R = \text{Re}(Z)$  and inductance  $L = \text{Im}(Z)/\omega$  between the terminals  $T_3$  and  $T_4$  for  $\partial\Omega = \Gamma_a$  in a LF regime, computed with both the stabilized MQS and full-wave BVPs (6.37) and (6.22), and the non-stabilized BVPs (6.35) and (6.8). Again, the full-wave system without

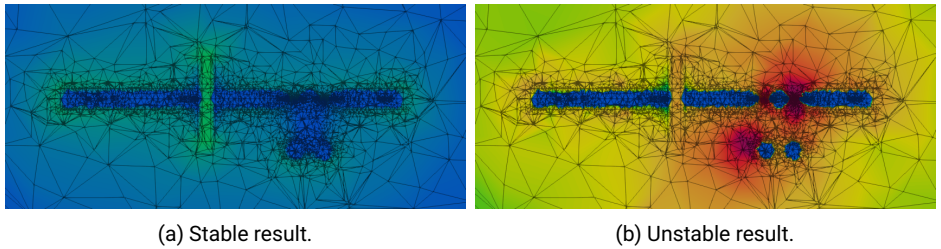


Figure 6.6.: [SKD22c] Magnitude  $|\mathbf{E}|$  of the electric field in the  $xy$  plane at  $f = 5$  kHz obtained with the unstable BVP (6.8) and BVP (6.15) for the model of Fig. 6.2 excited at terminals  $T_1$  and  $T_4$ , displayed with a logarithmic color map from  $10^8$  V/m (blue) to  $10^{15}$  V/m (violet). The unusually high values are due to the frequency-independent current excitation of (5.10). The boundaries of the tetrahedra of the mesh are indicated by lines (the field values between the mesh nodes are linearly interpolated). Whereas the stable result correctly shows a maximum of  $|\mathbf{E}|$  between the plates of the capacitor, the unstable result exhibits values of implausible strength and distribution. (© 2021 IEEE)

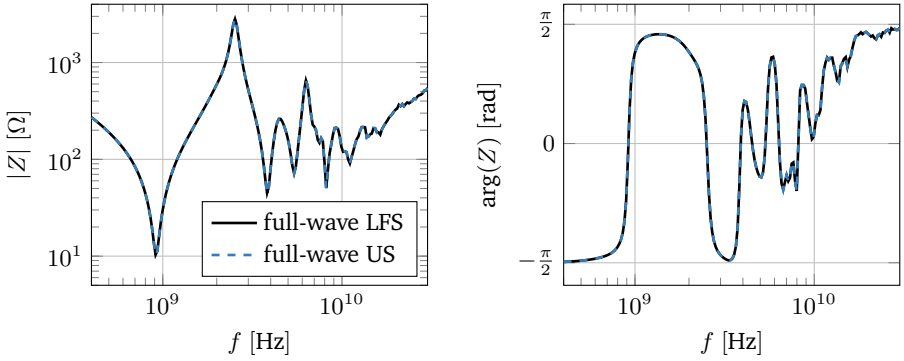


Figure 6.7.: Magnitude and phase of the impedance  $Z$  between terminals  $T_1$  and  $T_4$  of the model of Fig. 6.2 with  $\partial\Omega = \Gamma_a$  in a HF regime. The values of LFS BVP (6.22) and the conventional US BVP (6.8) are identical, demonstrating that the LFS BVP can be used at both low and high frequencies.

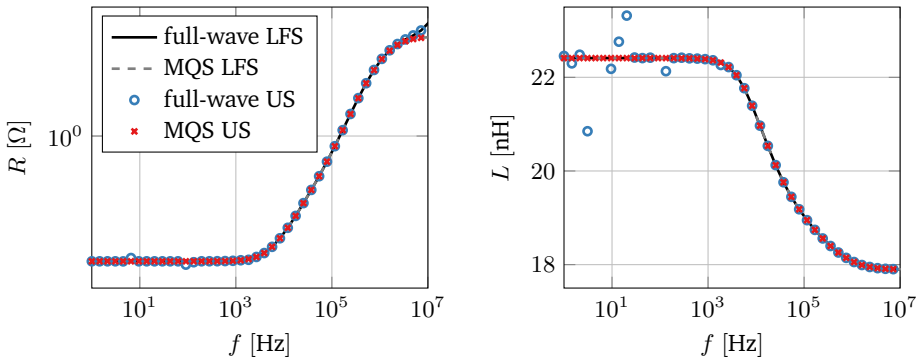


Figure 6.8.: Resistance  $R$  and inductance  $L$  between terminals  $T_3$  and  $T_4$  of the model of Fig 6.2 with  $\partial\Omega = \Gamma_a$  in a LF regime. Whereas the non-stabilized (US) full-wave result again exhibits a slightly unstable LF behavior, the MQS results are stable at all frequencies both with and without LF stabilization.

stabilization exhibits an unstable LF behavior, albeit at lower frequencies and much less pronounced than in the case displayed in Fig. 6.4, where the two terminals lie on different conductors. The MQS approximation, however, yields for the displayed frequencies  $f \geq 1$  Hz the same stable behavior with and without LF stabilization. Despite the good LF performance of the unstable MQS system, an extraction directly at the DC point  $f = k = 0$  is only possible with the stable BVP (6.37).

Moreover, the LF-stabilized MQS system has a performance advantage over the unstable system. Table 6.1 expands on the performance comparison of Table 5.1 for the 20 mm wire model of Section 5.4.1. Whereas in Table 5.1 only stable systems were considered, Table 6.1 compares the dimensions  $N$  and numbers of non-zero entries  $N^{\text{NZ}}$  of the full-wave, MQS and MS system matrices of both stable and unstable systems. The full-wave and MQS computation times listed are the average extraction times per frequency point after the system setup, and the times of the MS systems in the table are the average total times to obtain a solution, including the system setup time. The unstable MS BVP is simply (6.47) with  $\mathbf{v} \in H(\text{curl}, \Omega)$  instead of  $\mathbf{v} \in V$ .

The system matrix resulting from the LF-stabilized full-wave BVP (6.22) has a 20 % higher number  $N_{\text{lfs}}^{\text{NZ}}$  of non-zeros than the matrix of the unstable BVP (6.8) leading to a 27 % higher average computation time  $\bar{t}_{\text{lfs}}$ . These additional non-zero entries are a consequence of the construction of the finite-dimensional subspace  $U_h$  of gradient fields that vanish on the conductors as discussed in Subsection 6.6.2. The stable MQS and MS systems, however, do not require the space  $U_h$  and yield a significantly lower matrix dimension  $N_{\text{lfs}}$  and slightly lower number of non-zeros  $N_{\text{lfs}}^{\text{NZ}}$  than their unstable counterparts. This results in a 16 % faster average computation time for the MQS system and a 14 % faster time for the MS system.

Table 6.1: Comparison of the computational cost of extractions with the full-wave system, the MQS system, and the MS PEC case system both with LF stabilization (LFS) and without (US), as an expansion of the comparison presented in Table 5.1. Both the dimensions  $N$  and numbers  $N^{\text{NZ}}$  of non-zero entries of the matrices resulting from a FE discretization of the listed BVPs are provided. For the full-wave and MQS systems the stated computation times correspond to  $\bar{t}_f$  in Table 5.1 and for the MS systems to  $\bar{t}_0$ .

	BVP LFS	BVP US	$N_{\text{lfs}}$	$N_{\text{us}}$	$N_{\text{lfs}}^{\text{NZ}}$	$N_{\text{us}}^{\text{NZ}}$	$\bar{t}_{\text{lfs}}$ [s]	$\bar{t}_{\text{us}}$ [s]	$\bar{t}_{\text{lfs}}/\bar{t}_{\text{us}}$
full wave	(6.22)	(6.8)	520 k	520 k	27.3 M	22.7 M	86.5	67.9	1.27
MQS	(6.37)	(6.35)	435 k	520 k	13.7 M	13.9 M	36.1	43.0	0.84
MS PEC	(6.47)	-	336 k	520 k	8.71 M	9.54 M	38.2	44.7	0.86



---

## 7. Frequency-Dependent Parasitics for Transient Network Simulations

---

The parasitics extracted with the method of Chapter 5 are in general frequency dependent. While they can be utilized directly in AC (i.e., frequency domain) network simulations, their use in transient network simulations is not as straight-forward. Whereas in frequency domain, e.g., the impedance  $Z$  relates current  $I$  and voltage  $V$  by a mere multiplication in (4.4), in time-domain this operation becomes a convolution due to the convolution theorem (2.13).

The simplest way to avoid the high computational cost associated with computing a convolution integral at every time step is to only consider  $f$ -independent parasitics. For many EMC problems in a quasistatic frequency regime (i.e., at frequencies for which wave effects can be neglected) and in the absence of strongly dispersive material parameters, the inductive and capacitive parasitics of a DUT can be described frequency independently. The electrostatic capacitances computed as described in Subsection 4.1.3 are  $f$ -independent for non-dispersive permittivities  $\epsilon$ , and the same holds for the external inductance  $L_{\text{ext}}$  as computed in Subsection 5.2.1 for non-dispersive permeabilities  $\mu$ . As the contribution of the strongly  $f$ -dependent internal inductance  $L_{\text{int}}$  to the total inductance  $L$  is small for most models and even vanishes at higher frequencies, it is often justified to represent the inductive parasitics of the model in transient simulations with  $L_{\text{ext}}$ . Although the frequency dependence of the resistance  $R$  is strong for frequencies at which the skin effect cannot be neglected, the analysis of many EMC problems does not require an accurate resistance model, such that  $R$  can be approximated by its value at one frequency (e.g., at the DC point  $f = 0$ ).

However, in cases where the skin effect must be considered or significantly dispersive materials are present, or at frequencies beyond the quasistatic regime, an  $f$ -dependent description of the parasitic effects is mandatory. An example for a model with a strongly dispersive permeability is the common-mode choke considered in Chapter 9. A standard way to consider transmission lines with  $f$ -dependent parameters in transient simulations is the use of recursive convolutions [SD75], which minimize the computational cost by using the structure of the governing differential equations and a constant time step size  $h$  to compute the necessary convolutions recursively. For general frequency responses in the form of a transfer function like the impedance matrix  $\mathbf{Z}$ , an inclusion in transient circuit simulations using either recursive convolutions or an equivalent circuit can be facilitated by

the computation of a rational approximation of the transfer function through *vector fitting* [GS99]. While the recursive convolution approach of [GD13] is capable of considering impedance matrices  $\mathbf{Z}$  directly, its efficient implementation requires a relatively low-level control over the network simulation, which is generally not possible using the commercial network simulation tools prevalent in industry.

An alternative to the recursive convolution approach, that can facilitate the use of the extracted  $f$ -dependent parasitics in the network simulation workflows of development engineers, is the creation of an equivalent circuit consisting of  $f$ -independent lumped elements  $R$ ,  $L$ , and  $C$  from the rational approximation of a nodal admittance matrix  $\mathbf{Y}_N$  [Gus02]. The following section summarizes both the vector fitting method itself and the creation of an equivalent circuit from a nodal admittance matrix. Thereafter, Section 7.2 discusses the stability issues encountered with the equivalent circuit approach when using a nodal impedance matrix  $\mathbf{Z}_N$  as the original transfer function in an LF regime, and develops a strategy to avoid these issues. The proposed approach is also contained in [SKD22b] in a condensed form. Finally, Section 7.3 provides numerical results comparing the stability of the different approaches of Section 7.2.

## 7.1. Vector Fitting and Equivalent Circuit Creation

The vector fitting method [GS99] to compute rational approximations of a transfer functions was developed to extend the recursive convolution approach of [SD75] to arbitrary frequency responses, as recursive convolutions are readily applicable for rational functions. The merit of vector fitting lies in the method's capability to linearize the initially non-linear problem of fitting an arbitrary rational function to data in a way that does not lead to a badly conditioned linear system. To this end, the transfer function  $\mathbf{H}(\omega) : \mathbb{R} \rightarrow \mathbb{C}^{N \times N}$  (other forms of  $\mathbf{H}$  are also possible) is approximated with a pole-residue form (PRF),

$$\mathbf{H}(\omega) = \sum_{i=1}^{n_p} \frac{\mathbf{R}_i}{j\omega - p_i} + \mathbf{D} + j\omega\mathbf{E}. \quad (7.1)$$

that features in addition to a number of  $n_p$  poles  $p_i$  with the matrix-valued residues  $\mathbf{R}_i$  also an optional constant term  $\mathbf{D}$  and an optional linear term  $j\omega\mathbf{E}$ . While the matrices  $\mathbf{D}$  and  $\mathbf{E}$  are real, the poles and residues can either be real or part of a complex conjugate pair.

The vector fitting algorithm consists of two main steps, pole identification and residue identification. After choosing a set of initial poles  $p_{i,0}$  an iterative procedure identifies the optimal pole values  $p_i$  (see [GS99] for details). Using these poles, the optimal residues  $\mathbf{R}_i$  and parameters  $\mathbf{D}$  and  $\mathbf{E}$  are identified in a linear least-squares fit. The stability of the pole identification step can be improved especially for noisy data by using the “relaxed” approach of [Gus06] that relaxes an asymptotic requirement during the pole relocation. An even more substantial improvement is provided by the technique presented in [Des+08]

that restricts the unknowns in the pole relocation procedure to only the poles  $p_i$  (which the original method does not). This improvement is especially relevant for transfer functions of large dimension  $N$ . For data sets that have a high variation in the magnitude of their elements, weighting the data points in the least-squares fits of the procedure with an appropriate weighting scheme ensures a high quality of the rational approximation in the whole frequency interval [Gus02].

Any PRF of a scalar admittance

$$y(\omega) = \sum_{i=1}^{n_p} \frac{r_i}{j\omega - p_i} + d + j\omega e \quad (7.2)$$

corresponds directly to an equivalent circuit consisting only of  $f$ -independent resistors, inductors, and capacitors [Gus02]. As illustrated in Fig. 7.1, the circuit contains in a parallel arrangement one element or subnetwork for each term in the PRF. The linear and constant terms of (7.2) result in a capacitance and resistance, respectively,

$$C_0 = e, \quad R_0 = \frac{1}{d}. \quad (7.3)$$

Each real pole-residue term  $r_i/(j\omega - p_i)$  with  $r_i, p_i \in \mathbb{R}$  corresponds to a resistor and inductor in series,

$$R_{ri} = -p/r, \quad L_{ri} = 1/r. \quad (7.4)$$

Each complex conjugate pole-residue pair

$$\frac{r'_i + jr''_i}{j\omega(p'_i + jp''_i)} + \frac{r'_i - jr''_i}{j\omega(p'_i - jp''_i)} \quad (7.5)$$

with  $r'_i, r''_i, p'_i, p''_i \in \mathbb{R}$  is represented in the equivalent circuit as series connection of a resistor, an inductor, and a capacitor-resistor parallel connection,

$$L_{ci} = \frac{1}{2r'_i}, \quad (7.6)$$

$$R_{ci} = L_{ci}(-2p'_i + 2L_{ci}(r'_i p'_i + r''_i p''_i)), \quad (7.7)$$

$$C_{ci} = \frac{1}{L_{ci}(p_i'^2 + p_i''^2 + 2R_{ci}(r'_i p'_i + r''_i p''_i))}, \quad (7.8)$$

$$G_{ci} = -2C_{ci}L_{ci}(r'_i p'_i + r''_i p''_i). \quad (7.9)$$

Due to (4.52) any symmetric nodal admittance matrix  $\mathbf{Y}_N$  of dimension  $N \times N$  can be expressed with  $N(N+1)/2$  scalar branch admittances  $y$  and hence be exported as an equivalent circuit (for any  $y = 0$  no subnetwork is created). The passivity of the resulting equivalent circuit, which is critical for transient simulations, can be ensured as described in

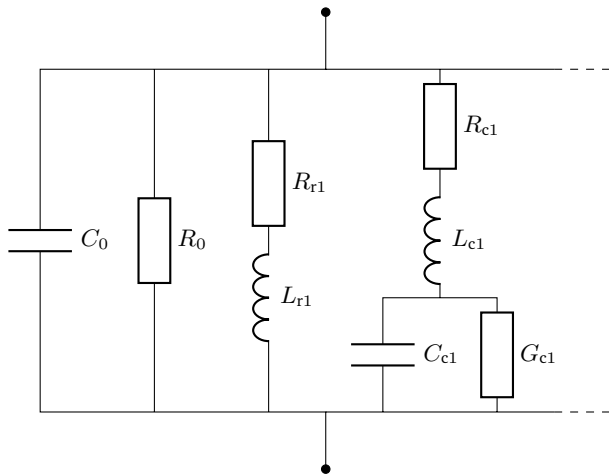


Figure 7.1.: Equivalent circuit of admittance PRF considering one real pole and one complex conjugate pole pair, adopted from [Gus02].

[GS01]. Although the passivity of the circuit can be guaranteed, it must be noted that some of the circuit's resistances, inductances, and capacitances typically take negative values. While negative elements do not pose a general problem for transient network simulations if they describe a passive network, some commercial simulation tools are still incompatible with negative elements and hence also with the equivalent circuits of [Gus02].

## 7.2. Stable Impedance-Based Equivalent Circuit Creation

Descriptions of the parasitics of a DUT with the impedance matrix  $\mathbf{Z}$ , admittance matrix  $\mathbf{Y}$ , and scattering matrix  $\mathbf{S}$  are, in principle, equivalent because the matrices can be converted into each other (e.g.,  $\mathbf{Y} = \mathbf{Z}^{-1}$ ). Admittance matrix descriptions are advantageous as they permit with (4.47) a direct conversion between nodal and branch matrices, which facilitates the expression of nodal admittance matrix PRFs as equivalent circuits discussed in the previous section. The impedance matrix  $\mathbf{Z}$ , however, is a quantity better suited for the actual parasitic extraction through a simulation of Maxwell's equations as described in Chapter 5: Whereas the computation of  $\mathbf{Y}$  requires the ports to be short-circuited and the computation of  $\mathbf{S}$  requires ports connected by a reference impedance  $Z_0$ , for the computation of  $\mathbf{Z}$  the ports are considered open-circuited, i.e., without requiring an additional connection. This property of  $\mathbf{Z}$  computations allows for any pair of terminals to be considered as a port

independently of their relative locations in the device, and it enables the extraction of parasitics that are de-embedded from the excitation provided at the port with respect to inductive coupling, as described in Subsection 5.1.4.

Utilizing a nodal impedance matrix  $\mathbf{Z}_N$  extracted with the method of Chapter 5 in a transient simulation as an equivalent circuit via vector fitting requires the inversion of  $\mathbf{Z}_N$  into a nodal admittance matrix  $\mathbf{Y}_N$ . However, in the standard case that not all terminals lie on the same conductor, both  $\mathbf{Z}_N$  and its condition number diverge for  $f \rightarrow 0$ , with  $\mathbf{Z}_N$  being singular at the DC point  $f = 0$ . Due to the finite precision of computers, the inversion becomes unstable already at a finite (but low) frequency  $f > 0$ . For applications that do not require an equivalent circuit that correctly models the parasitic behavior at low frequencies, the bad conditioning of  $\mathbf{Z}_N$  is inconsequential. If the LF behavior in general and particularly the DC behavior are relevant, the instability can be avoided by separately considering resistive and inductive effects on the one hand and capacitive effects on the other. Instead of computing the complete nodal impedance matrix  $\mathbf{Z}_N$  incorporating resistive, inductive, and capacitive effects with either the full-wave BVP (5.3) or Darwin BVP (5.25), the resistive and inductive effects can be considered in isolation by extracting a branch impedance matrix  $\mathbf{Z}_{RL}$  with the MQS BVP (5.24). Because the MQS approximation requires a conductive extraction topology (cf. Fig. 5.1) in which the two terminals of each port lie on the same conductor,  $\mathbf{Z}_{RL}$  is well-conditioned at all frequencies and can be inverted stably even at  $f = 0$ . As the ES capacitance extraction of Subsection 4.1.3 considers only branches not described with  $\mathbf{Z}_{RL}$ , the extracted capacitances can simply be added to the MQS result either in the creation of a nodal admittance matrix with (4.50) or directly to an equivalent circuit obtained from a MQS result only.

In the case that permittivity  $\varepsilon$  and hence also the ES capacitances are  $f$ -independent, the full procedure to stably generate an equivalent circuit for the parasitics contains, after the MQS extraction of  $\mathbf{Z}_{RL}$  and the ES capacitance extraction, three main steps:

1. A PRF  $\mathbf{Y}_{RL}^{\text{PR}}$  of the branch admittance matrix  $\mathbf{Y}_{RL} = \mathbf{Z}_{RL}^{-1}$  is computed with the vector fitting method.
2. The PRF  $\mathbf{Y}_{RL}^{\text{PR}}$  is transformed into the PRF  $\mathbf{Y}_N^{\text{PR}}$  of a nodal admittance matrix using the reduced incidence matrix  $\mathbf{A}_{RL}$  of the conductive topology,

$$\mathbf{Y}_N^{\text{PR}} = \mathbf{A}_{RL} \mathbf{Y}_{RL}^{\text{PR}} \mathbf{A}_{RL}^{\text{T}}. \quad (7.10)$$

This is realized by applying  $\mathbf{A}_{RL}$  individually to the matrices  $\mathbf{R}_i$ ,  $\mathbf{D}$ , and  $\mathbf{E}$  of the PRF (7.1).

3. An equivalent circuit is generated from  $\mathbf{Y}_N^{\text{PR}}$  as described in the previous section. If the reference node of  $\mathbf{A}_{RL}$  is not contained in any of the branches of the conductive topology, the resulting scalar branch admittances (4.52a) to the reference node are zero, and thus not considered in the equivalent circuit.

---

4. The ES capacitances (4.29) are added to the existing network.

If the permittivity  $\varepsilon$  and thus also the ES capacitances are  $f$ -dependent, the capacitances must be considered in a PRF of the nodal admittance matrix calculated with (4.50) from  $\mathbf{Y}_{RL}$  and the capacitive admittance matrix  $\mathbf{Y}_C$  of (4.51).

For applications that require a correct modeling of the parasitics from the DC point to high frequencies beyond the quasistatic regime, the nodal admittance matrix constructed from MQS and ES results can be used as LF data in the computation of a PRF, while the inverse of the full-wave nodal impedance matrix can provide the HF data.

### 7.3. Numerical Results

The capacitor-coil model of Fig. 6.2 is employed to exemplify the limits of a direct inversion of  $\mathbf{Z}_N$  as well as the stability and accuracy of the approach combining MQS and ES results. For an electric boundary  $\partial\Gamma = \Gamma_{el}$ , the full-wave BVP (5.3) is used to compute a nodal impedance matrix  $\mathbf{Z}_N$  in a star extraction topology  $\{(T_1, T_2), (T_1, T_3), (T_1, T_4)\}$ , and a branch admittance matrix  $\mathbf{Z}_{RL}$  containing the resistive and inductive response of the model is obtained with the MQS BVP (5.24) in the conductive topology  $\{(T_1, T_2), (T_3, T_4)\}$ . Additionally, the ES capacitances (4.29) are extracted described in Subsection 4.1.3.

Fig. 7.2 displays the condition numbers of  $\mathbf{Z}_N$  and  $\mathbf{Z}_{RL}$ . While the MQS branch admittance matrix is well conditioned at all frequencies, the condition number of  $\mathbf{Z}_N$  is relatively high in the entire frequency interval and diverges for  $f \rightarrow 0$ .

The effects of the diverging condition number of  $\mathbf{Z}_N$  can be seen in Fig. 7.3, which shows the real and imaginary parts of two elements  $Y_{N,ij} \equiv [\mathbf{Y}_N]_{ij}$  of the nodal admittance matrix  $\mathbf{Y}_N = \mathbf{Z}_N^{-1}$ , both for the original full-wave data and for three different PRFs obtained through vector fitting. The full-wave PRF uses  $n_p = 20$  poles resulting in an equivalent circuit of 168 elements, whereas the MQS PRF contains  $n_p = 15$  poles and omits the linear term  $\mathbf{E}$ , which results in an equivalent circuit of 100 elements including 4 added ES capacitances. Although the inversion of the FEM result  $\mathbf{Z}_N$  is executed using the multi-precision Python library *mpmath* with a decimal precision of 100, the full-wave data is still noisy in the plot for frequencies  $f < 100$  Hz. This is due to the fact that the FEM result can only be obtained with the standard double precision (corresponding to a decimal precision of about 16) in order to guarantee acceptable computation times. The very high condition numbers encountered below  $f = 100$  Hz cause the noisy inverse by amplifying the round-off errors contained in the  $\mathbf{Z}_N$  data. Fitting a PRF to all data points of the frequency interval yields an approximation that tries to capture the high dynamic of the erroneous LF values. This does not only lead to a reproduction of the data's inaccuracies in the PRF at low frequencies but also negatively impacts the approximation's quality at high frequencies  $f > 1$  MHz, as a large subset of the DoFs of the rational approximation are concerned with the LF dynamics.

One strategy to avoid these issues is to fit the PRF only to the stable data points above

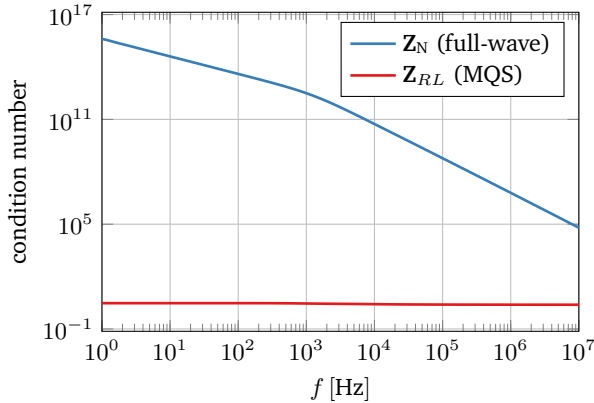


Figure 7.2.: Condition numbers of the full-wave nodal impedance matrix  $Z_N$  and the MQS branch impedance matrix  $Z_{RL}$ . Whereas the condition number of  $Z_N$  is relatively high in the whole frequency interval and diverges for  $f \rightarrow 0$ , the condition number of  $Z_{RL}$  stays low at all frequencies.

$f \approx 160$  Hz. In addition to correctly capturing the HF behavior, the resulting approximation gives plausible results also below  $f = 100$  Hz (with a minor exception for the real part of  $Y_{N,12}$ ). The disadvantage of this approach is that a cut-off frequency separating the unstable and stable admittance values must be identified, complicating the automation of the equivalent circuit generation desired in industrial workflows. Moreover, the application example of a common mode choke considered in Chapter 9 demonstrates that for some models it is entirely impossible to find an appropriate cut-off frequency. The PRF created by combining the equivalent circuit generated from the MQS impedance matrix  $Z_{RL}$  with the ES capacitances, as detailed in Section 7.2, exhibits a perfect behavior at all frequencies in Fig. 7.3.

The difficulties to obtain the correct low-frequency behavior from a full-wave nodal impedance matrix  $Z_N$  are further illustrated with Fig. 7.4, which compares the impedance  $Z$  between the terminals  $T_3$  and  $T_4$  of the model of Fig. 6.2 obtained directly with the FEM to the values computed in AC network simulations using two different equivalent circuits generated from  $Z_N$ . Both equivalent circuits are constructed from PRFs fitted to only the stable data points of  $Y_N = Z_N^{-1}$  above  $f \approx 160$  Hz. The circuits only differ in the machine precision used for the inversion of  $Z_N$ : Whereas the values of the circuit obtained with a non-standard multi-precision inversion agree perfectly with the FEM data, the circuit that relies on a standard double-precision inversion produces a strongly deviating behavior for

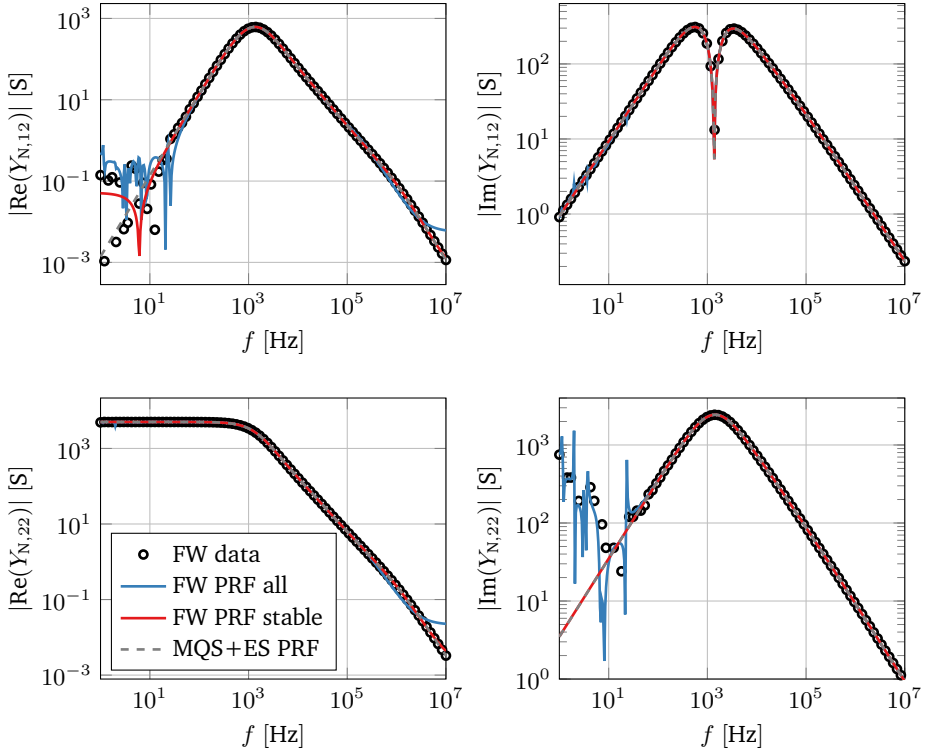


Figure 7.3.: Modulus of the real and imaginary parts of two elements of the nodal admittance matrix  $\mathbf{Y}_N = \mathbf{Z}_N^{-1}$ . The original full-wave (FW) data are compared to the values of three PRFs. Due to the finite precision of the FEM data  $\mathbf{Z}_N$  and the high condition number of  $\mathbf{Z}_N$ , the LF values of its inverse are noisy. Fitting a PRF to all data points yields a problematic behavior at both low and high frequencies. Restricting the fit to the stable data points above  $f \approx 160$  Hz eliminates the issue almost completely. The alternative approach of combining an MQS result with ES capacitances developed in Section 7.2 yields a perfectly behaved PRF.

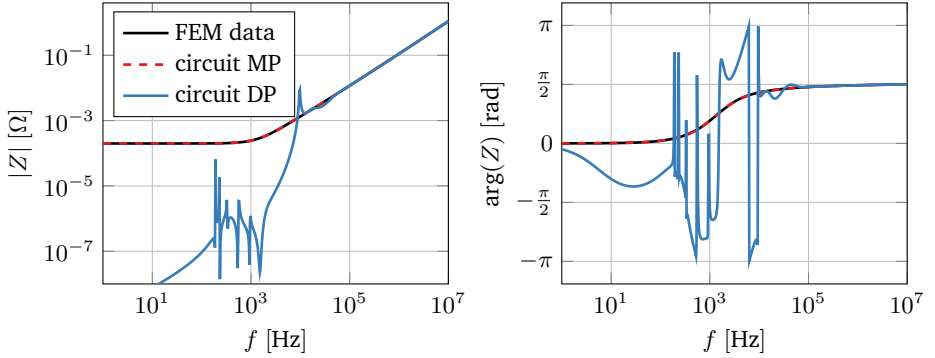


Figure 7.4.: Magnitude and phase of the impedance  $Z$  between terminals  $T_3$  and  $T_4$  of the model of Fig. 6.2, computed directly with the FEM and in AC network simulations from two different equivalent circuits. The circuits only differ in the machine precision used for the inversion of the nodal impedance matrix necessary in the circuit generation. Whereas the multi-precision (MP) result agrees perfectly with the FEM data, the double-precision (DP) result indicates that its circuit cannot be used for frequencies  $f \leq 10$  kHz.

frequencies  $f \leq 10$  kHz. While the  $\mathbf{Y}_N$  data points of Fig. 7.3 and its resulting stable PRF were obtained with the multi-precision inversion, admittance data and a PRF obtained with a double-precision inversion do not exhibit a qualitatively different behavior. Most notably, the different inversions yield virtually the same data points for frequencies  $f > 100$  Hz, suggesting that  $f = 160$  Hz is a reasonable cut-off frequency separating unstable  $\mathbf{Y}_N$  data points from stable ones. However, the fact that the multi- and double-precision circuits exhibit extreme differences in Fig. 7.4 in their LF impedance behavior demonstrates that the selection of an appropriate cut-off frequency is not a trivial task. This further motivates the use of the stable equivalent circuit generation from MQS and ES results developed in the previous section.



---

## 8. Sensitivity Analysis

---

### 8.1. Introduction

The primary purpose of the parasitic extraction of Chapter 5 is the assessment of the design of a DUT with regards to EMC or other design criteria. An equally important task, however, is how to find an optimized or optimal design. The optimization of an initial design can be mandated because the design violates certain requirements demanded by, e.g., the customer. In other cases finding the optimal design with respect to a specific QoI can reduce costs or simply improve the performance of the device. For these reasons, topology and shape optimizations are already well established in state-of-the-art design workflows in mechanical engineering [BC11]. The sensitivities of a QoI  $Q$  with respect to a set of parameters  $\{p_i\}$  expressed as the derivatives  $dy/dp_i$  can provide the foundation of gradient-based optimization algorithms.

A sensitivity analysis method built upon the parasitic extraction method of Traub et al. [Tra+12; Tra+13a] was developed by Schuhmacher et al. in [Sch+18b; Sch+18a] and in Schuhmacher's dissertation [Sch18]. The method uses the extracted frequency-independent parasitic resistances  $\mathbf{R}$ , partial inductances  $\mathbf{L}$ , and capacitances  $\mathbf{C}$  to express a QoI  $Q = Q(\mathbf{R}, \mathbf{L}, \mathbf{C})$ . By computing the sensitivities  $d\mathbf{R}/dp_i$ ,  $d\mathbf{L}/dp_i$ , and  $d\mathbf{C}/dp_i$  with respect to a number of parameters  $p_i$  of the finite element mesh (usually translations of either surface nodes or faces of the mesh), the sensitivities  $dQ/dp_i$  of the QoI are given with the chain rule,

$$\frac{dQ}{dp_i} = \frac{\partial Q}{\partial \mathbf{R}} \cdot \frac{d\mathbf{R}}{dp_i} + \frac{\partial Q}{\partial \mathbf{L}} \cdot \frac{d\mathbf{L}}{dp_i} + \frac{\partial Q}{\partial \mathbf{C}} \cdot \frac{d\mathbf{C}}{dp_i}. \quad (8.1)$$

An application of the method in the optimization of a pressure sensor [Ben+19; BHF20] attests to its merit.

To facilitate the efficient computation of the tens or hundreds of thousands of sensitivities required in industrial applications, Schuhmacher et al. employ the adjoint method [NBB04]. Their approach, however, still suffers from performance issues as its computation of the inductive sensitivities  $d\mathbf{L}/dp_i$  is based on the very indirect inductance computation of [Tra+13a], that is outlined in Subsection 5.3.2. Furthermore, it lacks a LF stabilization and exhibits minor accuracy issues (discussed in the context of Fig. 8.3).

To resolve these drawbacks, this chapter develops an MQS computation method for resistive and inductive sensitivities based on the MQS parasitic extraction of Subsection 5.2.1,

as well as an MS computation method for inductive sensitivities based on the MS inductance extraction of Subsection 5.2.1. In addition to resolving the performance, stability, and accuracy problems of the Darwin approximation approach of [Sch+18a], the MQS sensitivity analysis enables a frequency-dependent computation of resistive and inductive sensitivities and allows the consideration of complex-valued and dispersive magnetic permeabilities.

The following section executes the FE discretization of the MQS and MS weak-form BVPs of Chapter 6 and the ES BVP (4.23), transforming the BVPs into systems of linear equations, which is a prerequisite for the development of the sensitivity computation. Subsection 8.2.2 describes a comparatively simple computation of capacitive sensitivities, which is generalized from [Sch+18b] to efficiently treat the case of more than two conductors. Thereafter, Section 8.3 employs the adjoint method to derive efficient expressions for the computation of both the inductive and resistive sensitivities. Section 8.4 provides numerical results: The MQS sensitivity computation is exemplified with the model of a coil that features a magnetic core with a complex-valued, dispersive permeability  $\mu$ . The performance and accuracy advantages of the MS inductive sensitivity computation over the Darwin-approximation method of [Sch+18a] are demonstrated. This chapter is to a large extend part of a submitted article [Sty+22].

## 8.2. Finite Element Discretization

### 8.2.1. Magnetostatic and magnetoquasistatic systems

The BVP (6.10) for the scalar field  $g$ , the MQS BVP (6.38) for the electric field components  $\mathbf{E}_V$  and  $\mathbf{E}_W$ , and the BVP (6.25) for the compensated scalar potential  $\phi_c$  are discretized by expressing their fields with the functions of the finite-dimensional Sobolev spaces  $P_h'' \subset H^1(\Omega)''$ ,  $V_h \subset V$ ,  $W_h \equiv \text{grad } P_h^w \subset W$ , and  $P_h' \subset H^1(\Omega)'$  as

$$g = \sum_{\psi_i \in P_h''} g_i \psi_i, \quad \mathbf{E}_V = \sum_{\mathbf{v}_i \in V_h} e_i^v \mathbf{v}_i, \quad \mathbf{E}_W = \sum_{\psi \in P_h^w} e_i^w \text{grad } \psi_i, \quad \phi_c = j\mu_0 c \sum_{\psi_i \in P_h'} \phi_i^c \psi_i, \quad (8.2)$$

with the DoFs  $g_i$ ,  $e_i^v$ ,  $e_i^w$ , and  $\phi_i^c$ . This transforms the three continuous BVPs into algebraic linear systems of equations,

$$\mathbf{L}'_e \mathbf{g} = \mathbf{b}_g, \quad (8.3)$$

$$\underbrace{\begin{bmatrix} \mathbf{K}_v + jk\mathbf{V}_\sigma + \frac{1}{r_b}\mathbf{V}_a & j\sqrt{k}\mathbf{G}_\sigma \\ j\sqrt{k}\mathbf{G}_\sigma^\top & j\mathbf{L}_\sigma \end{bmatrix}}_{:=\mathbf{A}_e} \underbrace{\begin{pmatrix} e_v \\ e_w \end{pmatrix}}_{:=\mathbf{e}_e} = \mathbf{b}_e := \begin{pmatrix} -\mathbf{G}'_e \mathbf{g} \\ \frac{1}{\sqrt{k}} \mathbf{b}_w \end{pmatrix}, \quad (8.4)$$

$$\left[ \mathbf{L}_\varepsilon + \frac{2}{r_b} \mathbf{M}_a \right] \phi_c = \mathbf{b}_c := -k\mathbf{G}_\varepsilon^\top e_v - \sqrt{k}\mathbf{L}_\varepsilon^w e_w + k\mathbf{M}g. \quad (8.5)$$

Here,  $\mathbf{g}$ ,  $\mathbf{e}_v$ ,  $\mathbf{e}_w$ , and  $\phi_c$  are the DoF vectors (e.g.,  $\mathbf{g} = (g_1, g_2, \dots)^\top$ ) and  $r_b$  is the radial coordinate of the spherical ABC boundary  $\Gamma_a$  (if such a boundary is used). The elements of the various operator matrices are given by

$$[\mathbf{K}_\nu]_{ij} = \langle \nu_r \text{curl } \mathbf{v}_i, \text{curl } \mathbf{v}_j \rangle \quad \forall \mathbf{v}_i, \mathbf{v}_j \in V_h, \quad (8.6a)$$

$$[\mathbf{V}_\sigma]_{ij} = \langle \sigma \mathbf{v}_i, \mathbf{v}_j \rangle \quad \forall \mathbf{v}_i, \mathbf{v}_j \in V_h, \quad (8.6b)$$

$$[\mathbf{V}_a]_{ij} = \langle \hat{\mathbf{n}} \times \mathbf{v}_i, \hat{\mathbf{n}} \times \mathbf{v}_j \rangle_{\Gamma_a} \quad \forall \mathbf{v}_i, \mathbf{v}_j \in V_h, \quad (8.6c)$$

$$[\mathbf{G}_\varepsilon]_{ij} = \langle \varepsilon \mathbf{v}_i, \text{grad } \psi_j \rangle \quad \forall \mathbf{v}_i \in V_h, \forall \psi_j \in P'_h, \quad (8.6d)$$

$$[\mathbf{G}'_\varepsilon]_{ij} = \langle \varepsilon \mathbf{v}_i, \text{grad } \psi_j \rangle \quad \forall \mathbf{v}_i \in V_h, \forall \psi_j \in P''_h, \quad (8.6e)$$

$$[\mathbf{G}_\sigma]_{ij} = \langle \sigma \mathbf{v}_i, \text{grad } \psi_j \rangle \quad \forall \mathbf{v}_i \in V_h, \forall \psi_j \in P_h^w, \quad (8.6f)$$

$$[\mathbf{L}_\varepsilon]_{ij} = \langle \varepsilon \text{grad } \psi_i, \text{grad } \psi_j \rangle \quad \forall \psi_i, \psi_j \in P'_h, \quad (8.6g)$$

$$[\mathbf{L}_\varepsilon^w]_{ij} = \langle \varepsilon \text{grad } \psi_i, \text{grad } \psi_j \rangle \quad \forall \psi_i \in P'_h, \psi_j \in P_h^w, \quad (8.6h)$$

$$[\mathbf{L}'_\varepsilon]_{ij} = \langle \varepsilon \text{grad } \psi_i, \text{grad } \psi_j \rangle \quad \forall \psi_i, \psi_j \in P''_h, \quad (8.6i)$$

$$[\mathbf{L}_\sigma]_{ij} = \langle \sigma \text{grad } \psi_i, \text{grad } \psi_j \rangle \quad \forall \psi_i, \psi_j \in P_h^w, \quad (8.6j)$$

$$[\mathbf{M}]_{ij} = \langle \psi_i, \psi_j \rangle \quad \forall \psi_i \in P'_h, \psi_j \in P''_h, \quad (8.6k)$$

$$[\mathbf{M}_a]_{ij} = \langle \psi_i, \psi_j \rangle_{\Gamma_a} \quad \forall \psi_i, \psi_j \in P'_h. \quad (8.6l)$$

If the ABC boundary  $\Gamma_a$  is empty,  $\mathbf{G}_\varepsilon = \mathbf{G}'_\varepsilon$ ,  $\mathbf{L}_\varepsilon = \mathbf{L}'_\varepsilon$ , and  $\mathbf{V}_a = \mathbf{M}_a = 0$ . The RHS vectors  $\mathbf{b}_g$  of (8.3) and  $\mathbf{b}_w$  of (8.4) are constructed by selecting those elements of the full RHS vector  $\mathbf{b}_f$  that correspond to test functions  $\psi_i \in P''_h$  and  $\psi_i \in P_h^w$ , respectively. The elements of the full vector  $\mathbf{b}_f$  are given with the expression  $\text{div } \mathbf{J}_s$  of (5.10) as

$$[\mathbf{b}_f]_i = - \int_{\Omega} \psi_i \text{div } \mathbf{J}_s \, dV = \frac{I_0}{A(T_b)} \int_{T_b} \psi_i \, dS - \frac{I_0}{A(T_a)} \int_{T_a} \psi_i \, dS \quad \forall \psi_i \in P'_h. \quad (8.7)$$

If  $\Gamma_a$  is empty,  $\mathbf{b}_g = \mathbf{b}_f$ .

The discretized equivalent of (4.36) calculating the element  $Z_{ij}$  of the impedance matrix is hence

$$Z_{ij} = \frac{j\mu_0 c}{I_0^2} \mathbf{b}_f^{(i)} \cdot \phi_c^{(j)} =: \mathbf{f}_c^{(i)} \cdot \phi_c^{(j)}, \quad (8.8)$$

with the measurement vector  $\mathbf{f}_c^{(i)}$ . Using a direct solver to solve the linear systems (8.3)-(8.5) allows to calculate the full impedance matrix  $\mathbf{Z}$  at once by using the matrix-valued RHS  $\mathbf{B}_f = [\mathbf{b}_f^{(1)} \ \mathbf{b}_f^{(2)} \ \dots]$  to calculate the solution matrix  $\Phi_c = [\phi_c^{(1)} \ \phi_c^{(2)} \ \dots]$ ,

$$\mathbf{Z} = \frac{j\mu_0 c}{I_0^2} \mathbf{B}_f^\top \Phi_c. \quad (8.9)$$

The discretization of the MS PEC case BVPs (6.47) and (5.29) is analogous to the lossy case. However, the finite-dimensional subspace of the vectorial trial and test functions  $\mathbf{v}_i$  is

$\tilde{V}_h \subset \tilde{V}$  instead of  $V_h$ , for the  $\tilde{V}$  of (6.43). This yields the real-valued linear systems

$$\left[ \mathbf{K}_\nu + \frac{1}{r_b} \mathbf{V}_a \right] \mathbf{e}_v = \mathbf{b}_v := -\mathbf{G}_\varepsilon \mathbf{g}, \quad (8.10)$$

$$\mathbf{L}_\varepsilon \boldsymbol{\vartheta} = \mathbf{b}_\vartheta := -\mathbf{G}_\varepsilon^\top \mathbf{e}_v + \mathbf{M} \mathbf{g}. \quad (8.11)$$

The external inductance matrix  $\mathbf{L}_{\text{ext}}$  can be computed analogously to (8.9) with a matrix-valued RHS  $\mathbf{B}_f$  and solution  $\boldsymbol{\Theta} = [\boldsymbol{\vartheta}^{(1)} \ \boldsymbol{\vartheta}^{(2)} \ \dots]$ ,

$$\mathbf{L}_{\text{ext}} = \frac{\mu_0}{I_0^2} \mathbf{B}_f^\top \boldsymbol{\Theta}. \quad (8.12)$$

## 8.2.2. Electrostatic system and capacitive sensitivities

The computation of capacitive sensitivities developed in [Sch+18b; Sch18] is adopted in this work. However, one important modification greatly increases the computational efficiency of the method. As stated in [Sch18, Section 2.2], for a system of  $N$  terminals the original method requires  $M = N(N-1)/2$  solutions of the ES BVP (4.23) and a least-squares fit to compute the capacitance matrix. This requirement translates to the computation of the capacitive sensitivities  $d\mathbf{C}/dp_i$ . In contrast, the capacitance extraction approach of Subsection 4.1.3 only requires  $N$  fundamental solutions and no fit.

Solving the ES BVP (4.23) with the functions of  $P_h$  yields the solution vector  $\phi$  such that  $\phi = \sum_{\psi_i \in P_h} [\phi]_i \psi_i$ . The discrete form of (4.21) computing the electric energy of the system is

$$W_E = \phi^\top \mathbf{L}_\varepsilon \phi, \quad (8.13)$$

using the discrete Laplace operator  $\mathbf{L}_\varepsilon$  of (8.6g). The discrete versions of the equations (4.27) and (4.28) determining the main-diagonal and off-diagonal entries of the nodal capacitance matrix are

$$[\mathbf{C}_N]_{ii} = \frac{1}{\varphi_0^2} \phi_i^\top \mathbf{L}_\varepsilon \phi_i, \quad (8.14a)$$

$$[\mathbf{C}_N]_{ij} = \frac{1}{2\varphi_0^2} \phi_{ij}^\top \mathbf{L}_\varepsilon \phi_{ij} - \frac{1}{2} ([\mathbf{C}_N]_{ii} + [\mathbf{C}_N]_{jj}), \quad (8.14b)$$

where  $\phi_i$  denotes solution vector obtained by setting the potential to  $\varphi_0$  on conductor  $i$  and zero on all other conductors, and  $\phi_{ij} = \phi_i - \phi_j$ .

For the computation of the capacitive sensitivities  $d\mathbf{C}/dp_i$  Schuhmacher et al. [Sch+18b] show that only the derivative of the linear operator has to be considered as the sensitivities do not depend on the derivatives of the DoF vector  $\phi$ . Therefore, the sensitivities of the mutual capacitance  $C_{jk}$  of (4.29) between terminal  $j$  and  $k$  are simply

$$\frac{dC_{jk}}{dp_i} = -\frac{1}{2\varphi_0^2} \phi_{jk}^\top \frac{d\mathbf{L}_\varepsilon}{dp_i} \phi_{jk} + \frac{1}{2} \left( \frac{d[\mathbf{C}_N]_{jj}}{dp_i} + \frac{d[\mathbf{C}_N]_{kk}}{dp_i} \right) \quad (8.15)$$

with

$$\frac{d[\mathbf{C}_N]_{jj}}{dp_i} = \frac{1}{\varphi_0^2} \phi_j^\top \frac{d\mathbf{L}_\varepsilon}{dp_i} \phi_j. \quad (8.16)$$

The FE matrix derivative  $d\mathbf{L}_\varepsilon/dp_i$  is very sparse and can be assembled cheaply using a finite difference scheme as described in [Sch18].

### 8.3. Computation of Resistive and Inductive Sensitivities

Both resistive sensitivities  $d\mathbf{R}/dp_i$  and inductive sensitivities  $d\mathbf{L}/dp_i$  are given through the sensitivities of the MQS impedance matrix

$$\frac{d\mathbf{Z}}{dp_i} = \frac{d\mathbf{R}}{dp_i} + j\omega \frac{d\mathbf{L}}{dp_i}. \quad (8.17)$$

To enable an efficient calculation of a large number of these geometric sensitivities, it must be avoided to solve the three BVPs (6.10), (6.38), and (6.25) multiple times. This can be achieved by using the adjoint method [NBB04], with which an expression for  $d\mathbf{Z}/dp_i$  can be derived that needs the solution vectors  $\mathbf{g}$ ,  $\mathbf{e}_v$ ,  $\mathbf{e}_w$ , and  $\phi_c$  only for the original choice of geometric parameters  $p_i$ . It introduces the derivatives with respect to  $p_i$  solely through the geometric derivatives of the operator matrices (8.6), which are cheap to compute.

The concept of the adjoint method is introduced in the following subsection. Subsection 8.3.2 applies the method to the MQS systems of linear equations introduced in Subsection 8.2.1, and Subsection 8.3.3 provides an expression for the direct computation of inductive sensitivities enabled by the MS linear systems of equations.

#### 8.3.1. Adjoint sensitivity computation

A scalar QoI  $Q$  is given as a product of the measurement vector  $\mathbf{f}$  and solution vector  $\mathbf{x}$  of a linear system of equations (as in the calculation of an element  $[\mathbf{Z}]_{ij}$  of the inductance matrix with (8.8)),

$$Q = \mathbf{f}^H \mathbf{x} \quad (8.18)$$

with  $\mathbf{x}$  being subject to

$$\mathbf{A}\mathbf{x} = \mathbf{b}. \quad (8.19)$$

The superscript H denotes the adjoint (i.e., conjugate transpose) of a vector or matrix,  $\mathbf{A}$  is a linear operator and  $\mathbf{b}$  is the RHS vector. If many QoIs have to be calculated with the same vector  $\mathbf{f}$  (but different RHS vectors  $\mathbf{b}$ ), the adjoint method can be used to compute  $Q$  directly as the scalar product of an adjoint solution  $\boldsymbol{\lambda}$  with any RHS  $\mathbf{b}$  of (8.19). The adjoint solution  $\boldsymbol{\lambda}$  is calculated solving the adjoint linear system

$$\mathbf{A}^H \boldsymbol{\lambda} = \mathbf{f}. \quad (8.20)$$

The QoI  $Q$  can be expressed with the adjoint solution  $\lambda$  as

$$Q = \mathbf{f}^H \mathbf{x} = \lambda^H \mathbf{A} \mathbf{x} = \lambda^H \mathbf{b}. \quad (8.21)$$

The relevance of the adjoint method for sensitivity computations becomes clear when considering the geometric sensitivities of the QoI  $Q$ ,

$$\frac{dQ}{dp_i} = \left( \frac{\partial Q}{\partial \mathbf{x}} \right)^H \frac{d\mathbf{x}}{dp_i} = \mathbf{f}^H \frac{d\mathbf{x}}{dp_i} = \lambda^H \mathbf{A} \frac{d\mathbf{x}}{dp_i}. \quad (8.22)$$

Differentiating (8.19) with respect to the geometric parameter  $p_i$  gives

$$\frac{d\mathbf{A}}{dp_i} \mathbf{x} + \mathbf{A} \frac{d\mathbf{x}}{dp_i} = \frac{d\mathbf{b}}{dp_i}. \quad (8.23)$$

Subtracting the first LHS term and inserting the result into (8.22) yields

$$\frac{dQ}{dp_i} = \lambda^H \left( \frac{d\mathbf{b}}{dp_i} - \frac{d\mathbf{A}}{dp_i} \mathbf{x} \right). \quad (8.24)$$

Hence, if both the primal solution  $\mathbf{x}$  and the adjoint solution  $\lambda$  are known, only the geometric derivatives of the operator and RHS of (8.19),  $d\mathbf{A}/dp_i$  and  $d\mathbf{b}/dp_i$ , respectively, have to be computed to calculate the sensitivity  $dQ/dp_i$ .

The derivative  $d\mathbf{A}/dp_i$  of the already sparse FE operator  $\mathbf{A}$  can be efficiently assembled with a finite difference scheme, which yields an extremely sparse result. Furthermore, if  $\mathbf{A}$  is real and symmetric (which the operators  $\mathbf{L}_\varepsilon$  and  $\mathbf{K}_\nu$  of the discretized BVPs (8.3) and (8.10) are) then  $\mathbf{A}$  is also self-adjoint,  $\mathbf{A}^H = \mathbf{A}$ . In this case  $\mathbf{A}$  has to be factorized only once to compute both the primal solution  $\mathbf{x}$  and the adjoint solution  $\lambda$  with a direct solver.

### 8.3.2. Magnetoquasistatic sensitivity computation

The considerations of the previous subsection are now applied in the computation of the geometric sensitivities of the scalar impedance  $Z$  of a one-port system. Multi-port systems can be treated analogously by using the matrix-valued RHS and solution vectors of (8.9).

Applying the adjoint sensitivity calculation of (8.24) to the impedance expression (8.8) using the BVP for  $\phi_c$  (8.5) yields the following result for the sensitivity of the impedance,

$$\frac{dZ}{dp_i} = \left( \frac{\partial Z}{\partial \phi_c} \right)^T \frac{d\phi_c}{dp_i} = \mathbf{f}_c^T \frac{d\phi_c}{dp_i} = \lambda_c^T \left( \frac{d\mathbf{b}_c}{dp_i} - \frac{d\mathbf{L}_\varepsilon}{dp_i} \phi_c \right). \quad (8.25)$$

The derivative  $d\mathbf{M}_a/dp_i$  does not appear in the equation since the non-zero entries of  $\mathbf{M}_a$  are all associated with the ABC boundary  $\Gamma_a$  and only geometric variations  $dp_i$  of the actual

device are considered in the sensitivity analysis. The adjoint solution  $\lambda_c$  is determined by the real-valued linear system

$$\left[ \mathbf{I}_\varepsilon + \frac{2}{r_b} \mathbf{M}_a \right] \lambda_c = \mathbf{f}_c, \quad (8.26)$$

as both  $\mathbf{L}_\varepsilon$  and  $\mathbf{M}_a$  symmetric real and hence self-adjoint.

The term  $\lambda_c^\top (d\mathbf{b}_c/dp_i)$  in (8.25) must be broken down further using the RHS of (8.5) and the definition  $\mathbf{B}_\varepsilon := [k\mathbf{G}_\varepsilon^\top \sqrt{k}\mathbf{L}_\varepsilon^w]$ ,

$$\begin{aligned} \lambda_c^\top \frac{d\mathbf{b}_c}{dp_i} &= -\lambda_c^\top \frac{d\mathbf{B}_\varepsilon \mathbf{x}_e}{dp_i} + k\lambda_c^\top \frac{d(\mathbf{M}\mathbf{g})}{dp_i} \\ &= -k\lambda_c^\top \frac{d\mathbf{G}_\varepsilon^\top}{dp_i} \mathbf{e}_v - \sqrt{k}\lambda_c^\top \frac{d\mathbf{L}_\varepsilon^w}{dp_i} \mathbf{e}_w + k\lambda_c^\top \frac{d\mathbf{M}}{dp_i} \mathbf{g} - \lambda_c^\top \mathbf{B}_\varepsilon \frac{d\mathbf{x}_e}{dp_i} + k\lambda_c^\top \mathbf{M} \frac{d\mathbf{g}}{dp_i}. \end{aligned} \quad (8.27)$$

The last two terms in (8.27) can again be treated with the adjoint method. Using the linear systems for  $\mathbf{x}_e$  and  $\mathbf{g}$ , (8.4) and (8.3), two additional adjoint solutions can be calculated by solving

$$\mathbf{A}_\varepsilon^H \lambda_e = \mathbf{f}_e \quad \text{with } \mathbf{f}_e := \mathbf{B}_\varepsilon^\top \lambda_c, \quad (8.28)$$

$$\mathbf{L}'_\varepsilon \lambda_{gc} = \mathbf{f}_{gc} \quad \text{with } \mathbf{f}_{gc} := \mathbf{M} \lambda_c. \quad (8.29)$$

With these adjoint solutions the terms in question can be expressed as

$$\lambda_c^\top \mathbf{B}_\varepsilon \frac{d\mathbf{x}_e}{dp_i} = \mathbf{f}_e^\top \frac{d\mathbf{x}_e}{dp_i} = -\lambda_e^H \frac{d\mathbf{A}_\varepsilon}{dp_i} \mathbf{x}_e + \lambda_e^H \frac{d\mathbf{b}_e}{dp_i}, \quad (8.30)$$

$$\lambda_c^\top \mathbf{M} \frac{d\mathbf{g}}{dp_i} = \mathbf{f}_{gc}^\top \frac{d\mathbf{g}}{dp_i} = -\lambda_{gc}^\top \frac{d\mathbf{L}'_\varepsilon}{dp_i} \mathbf{g} + \underbrace{\lambda_{gc}^\top \frac{d\mathbf{b}_g}{dp_i}}_{=0}. \quad (8.31)$$

The derivative  $d\mathbf{b}_g/dp_i$  is zero since geometrical variations of the terminal surfaces are not considered by the method and all elements of  $\mathbf{b}_g$  are zero except those associated with the terminal surfaces. Thus, only the last term in (8.30) remains to be treated. Dividing  $\lambda_e$  into two parts of the lengths of  $\mathbf{e}_v$  and  $\mathbf{e}_w$ ,  $\lambda_e =: (\lambda_v, \lambda_w)^\top$ , yields

$$\lambda_e^H \frac{d\mathbf{b}_e}{dp_i} = -\lambda_v^H \frac{d\mathbf{G}'_\varepsilon}{dp_i} \mathbf{g} - \lambda_w^H \mathbf{G}'_\varepsilon \frac{d\mathbf{g}}{dp_i} + \frac{1}{\sqrt{k}} \lambda_w^H \underbrace{\frac{d\mathbf{b}_w}{dp_i}}_{=0}. \quad (8.32)$$

The second term on the RHS demands again an adjoint solution  $\lambda_{gv}$ , which is calculated analogously to (8.29),

$$\mathbf{L}'_\varepsilon \lambda_{gv} = \mathbf{f}_{gv} \quad \text{with } \mathbf{f}_{gv} := \mathbf{G}'_\varepsilon{}^\top \lambda_v. \quad (8.33)$$

This leads to an equation analogous to (8.31):

$$\lambda_v^H \mathbf{G}'_\varepsilon \frac{d\mathbf{g}}{dp_i} = \mathbf{f}_{gv}^H \frac{d\mathbf{g}}{dp_i} = -\lambda_{gv}^H \frac{d\mathbf{L}'_\varepsilon}{dp_i} \mathbf{g} + \lambda_{gv}^H \underbrace{\frac{d\mathbf{b}_g}{dp_i}}_{=0}. \quad (8.34)$$

With this, all individual terms are treated and the result can be assembled. Firstly inserting (8.34) into (8.32) and the resulting equation into (8.30) gives

$$\lambda_c^T \mathbf{B}_e \frac{d\mathbf{x}_e}{dp_i} = -\lambda_e^H \frac{d\mathbf{A}_e}{dp_i} \mathbf{x}_e - \lambda_v^H \frac{d\mathbf{G}'_\varepsilon}{dp_i} \mathbf{g} + \lambda_{gv}^H \frac{d\mathbf{L}'_\varepsilon}{dp_i} \mathbf{g}. \quad (8.35)$$

The final result for  $dZ/dp_i$  is then produced by inserting (8.31) and (8.35) into (8.27) and the resulting equation into (8.25), which yields

$$\begin{aligned} \frac{dZ}{dp_i} = & -\lambda_c^T \left( \frac{d\mathbf{L}_\varepsilon}{dp_i} \phi_c + k \frac{d\mathbf{G}_\varepsilon^T}{dp_i} \mathbf{e}_v + \sqrt{k} \frac{d\mathbf{L}_\varepsilon^w}{dp_i} \mathbf{e}_w - k \frac{d\mathbf{M}}{dp_i} \mathbf{g} \right) \\ & + \lambda_e^H \frac{d\mathbf{A}_e}{dp_i} \mathbf{x}_e + \lambda_v^H \frac{d\mathbf{G}'_\varepsilon}{dp_i} \mathbf{g} - \lambda_g^H \frac{d\mathbf{L}'_\varepsilon}{dp_i} \mathbf{g} \end{aligned} \quad (8.36)$$

with  $\lambda_g := k\lambda_{gc} + \lambda_{gv}$ . The associated resistive and inductive sensitivities are given through (8.17) as

$$\frac{dR}{dp_i} = \text{Re} \left( \frac{dZ}{dp_i} \right), \quad \frac{dL}{dp_i} = \frac{1}{j\omega} \text{Im} \left( \frac{dZ}{dp_i} \right). \quad (8.37)$$

### 8.3.3. Magnetostatic computation of inductive sensitivities

For models that do not feature any materials with a strongly dispersive magnetic permeability  $\mu$ , the frequency-independent sensitivities  $dL_{\text{ext}}/dp_i$  of the external inductance  $L_{\text{ext}}$  can be sufficient to answer many EMC-driven questions. In this case the PEC approach of Section 5.3.1 provides a computationally very efficient basis to calculate the inductive sensitivities. It involves only real-valued BVPs, and also needs significantly fewer DoFs, since its central BVP (5.28) determines only  $E_V$  in the non-conducting subdomain  $\Omega_0$ .

The derivation of an expression for the inductive sensitivities is analogous to that of the sensitivities of the impedance matrix. Using the BVPs determining  $\vartheta$  and  $\mathbf{e}_v$ , (8.11) and (8.10), respectively, instead of (8.5) and (8.4), the result of the derivation reads

$$\frac{dL_{\text{ext}}}{dp_i} = -\lambda_\vartheta^T \left( \frac{d\mathbf{L}_\varepsilon}{dp_i} \vartheta + \frac{d\mathbf{G}_\varepsilon^T}{dp_i} \mathbf{e}_v - \frac{d\mathbf{M}}{dp_i} \mathbf{g} \right) + \lambda_v^T \left( \frac{d\mathbf{K}_v}{dp_i} \mathbf{e}_v + \frac{d\mathbf{G}'_\varepsilon}{dp_i} \mathbf{g} \right) - \lambda_g^T \frac{d\mathbf{L}'_\varepsilon}{dp_i} \mathbf{g} \quad (8.38)$$

with  $\lambda_g := \lambda_{g\vartheta} + \lambda_{gv}$ . The linear systems determining the adjoint solutions are

$$\left[ \mathbf{L}_\varepsilon + \frac{2}{r_b} \mathbf{M}_a \right] \lambda_{\vartheta} = \mathbf{f}_{\vartheta} := (\mu_0/I_0^2) \mathbf{b}_g, \quad (8.39)$$

$$\left[ \mathbf{K}_\nu + \frac{1}{r_b} \mathbf{V}_a \right] \lambda_v = \mathbf{f}_v := \mathbf{G}_\varepsilon \lambda_{\vartheta}, \quad (8.40)$$

$$\mathbf{L}'_\varepsilon \lambda_{g\vartheta} = \mathbf{f}_{g\vartheta} := \mathbf{M} \lambda_{\vartheta}, \quad (8.41)$$

$$\mathbf{L}'_\varepsilon \lambda_{gv} = \mathbf{f}_{gv} := \mathbf{G}'_\varepsilon \lambda_v. \quad (8.42)$$

## 8.4. Numerical Results

The following discussion of numerical results focuses on the differences between the MQS/MS sensitivity computation methods developed in this chapter and the original method of [Sch+18a]. Subsection 8.4.1 showcases the  $f$ -dependent MQS sensitivity computation method of Subsection 8.3.2, and Subsection 8.4.2 presents a direct performance comparison between the method of [Sch+18a] and the MS method of Subsection 8.3.3. An application of the sensitivity analysis in the optimization of a noise filter (which would also have been possible with the original method of [Sch+18a]) is documented in [Sty+22].

### 8.4.1. Choke with magnetic core

The ability to consider the resistive and inductive sensitivities frequency-dependently with the expression of (8.36) is demonstrated with the model of a choke with a cylindrical magnetic core, as shown in Figure 8.1. The small-signal relative magnetic permeability  $\mu_r$  of the core material is modeled using a first-order Debye model,

$$\mu_r(f) = \mu_\infty + \frac{\mu_s - \mu_\infty}{1 + jf\tau}, \quad (8.43)$$

with  $\mu_\infty = 1$ ,  $\mu_s = 2500$ , and  $\tau = 100$  ns.

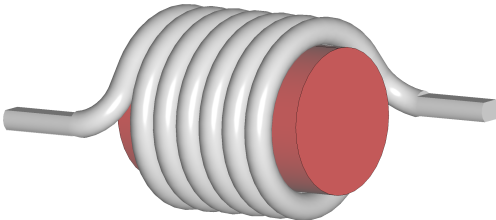
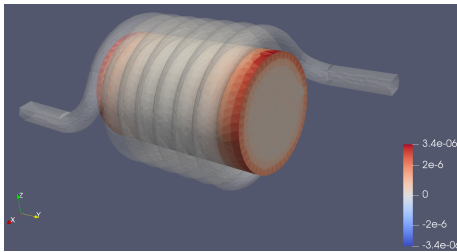


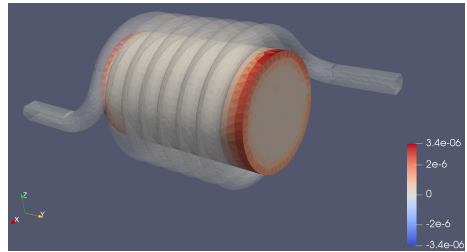
Figure 8.1.: [Sty+22] Choke consisting of a coil around a magnetic core (total length 34 mm).

An optimal choke possesses a maximal inductance  $L$  and a minimal resistance  $R$ . To investigate how the choke can be optimized by changing the core's shape, the sensitivities of the choke's inductance and resistance with respect to shifts of mesh faces on the core's surface are computed at both ends of the relevant frequency interval  $100 \text{ Hz} \leq f \leq 1 \text{ GHz}$ . The results are displayed in Fig. 8.2. Shades of blue and red on the core's surface indicate that a shift of the colored face in the direction of its normal would decrease and increase the QoI ( $R$  or  $L$ ), respectively. Whereas the inductive sensitivities remain largely constant in the frequency interval, the resistive sensitivities at 100 Hz are much smaller than those at 1 GHz, both absolutely and relatively to the values of  $R$  at these frequencies,  $R(100 \text{ Hz}) = 1.4 \text{ m}\Omega$  and  $R(1 \text{ GHz}) = 1.2 \text{ k}\Omega$ .

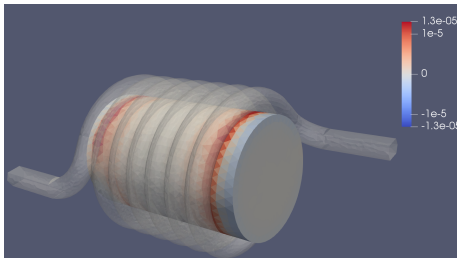
For  $f = 1 \text{ GHz}$  the optimal shape of the core maximizing the inductance while minimizing the resistance cannot be inferred from Fig. 8.2 directly, as a bone-like shape would maximize both quantities. A sensitivity analysis with respect to Cartesian shifts of the core's mesh



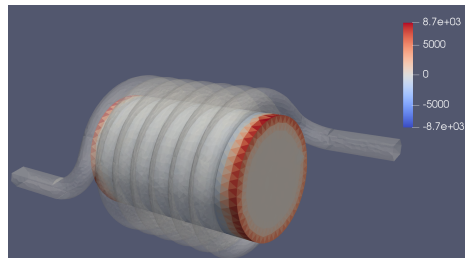
(a)  $dL/dp_i$  in H/m at  $f = 100 \text{ Hz}$ .



(b)  $dL/dp_i$  in H/m at  $f = 1 \text{ GHz}$ .



(c)  $dR/dp_i$  in  $\Omega/\text{m}$  at  $f = 100 \text{ Hz}$ .



(d)  $dR/dp_i$  in  $\Omega/\text{m}$  at  $f = 1 \text{ GHz}$ .

Figure 8.2.: [Sty+22] Inductive and resistive sensitivities of the choke model with respect to shifts of the magnetic core's faces at frequencies  $f = 100 \text{ Hz}$  and  $f = 1 \text{ GHz}$ . Whereas the inductive sensitivities are almost identical at the two frequencies, the LF and HF resistive sensitivities differ drastically.

nodes can be utilized for a multi-objective gradient-based shape optimization. This is, however, beyond the scope of this thesis and may be the objective of a future investigation.

## 8.4.2. Performance comparison

The performance of the direct inductive sensitivity computation method derived in Subsection 8.3.3 can be compared to that of the method of Schuhmacher et al. [Sch+18a], as both methods use PECs to compute frequency-independent sensitivities  $d\mathbf{L}_{\text{ext}}/dp_i$  of the external inductance matrix  $\mathbf{L}_{\text{ext}}$ .

As discussed in Subsection 5.3.2 the inductance computation method of [Sch+18a] obtains  $\mathbf{L}_{\text{ext}}$  in an indirect fashion by computing the nodal reactance matrix  $\mathbf{X}_N$  in Darwin's approximation at a number  $n \geq 2$  of frequency points, using a least-squares fit to separate the inductive contribution from the capacitive one. Subsequently,  $\mathbf{L}_{\text{ext}}$  is retrieved from the result of the fit with the Moor-Penrose pseudoinverse  $\mathbf{A}_L^+$  of the incidence matrix  $\mathbf{A}_L$  of the inductive branches in the network. The computation of inductive sensitivities proposed in [Sch+18a] hence contains the following steps:

1. Compute the sensitivities  $\frac{d\mathbf{X}_N}{dp_i}(f)$  of the nodal reactance matrix at  $n \geq 2$  frequency points  $f$  using the PEC case Darwin BVP (5.31).
2. Invert the sensitivities,  $\frac{d\mathbf{X}_N^{-1}}{dp_i} = \mathbf{X}_N^{-1} \frac{d\mathbf{X}_N}{dp_i} \mathbf{X}_N^{-1}$ , and extract the inverse nodal inductive sensitivities with a fit to  $\frac{d\mathbf{X}_N^{-1}}{dp_i} = \omega \frac{d\mathbf{C}_N}{dp_i} - \frac{1}{\omega} \frac{d\mathbf{L}_N^{-1}}{dp_i}$ .
3. Use the pseudo-inverse  $\mathbf{A}_L^+$  to compute the sensitivities of the inverse branch inductance matrix,  $\frac{d\mathbf{L}_{\text{ext}}^{-1}}{dp_i} = \mathbf{A}_L^+ \frac{d\mathbf{L}_N^{-1}}{dp_i} (\mathbf{A}_L^+)^T$ , and invert again,  $\frac{d\mathbf{L}_{\text{ext}}}{dp_i} = -\mathbf{L}_{\text{ext}} \frac{d\mathbf{L}_{\text{ext}}^{-1}}{dp_i} \mathbf{L}_{\text{ext}}$ .

The two main drawbacks of this method are the large dimension and hence computation times of the Darwin approximation system (compared to the more efficient MS system), and the sometimes difficult choice of the frequencies in its first step. The fit requires the frequencies to be below the first resonance of the impedance but also above the LF regime, where the Darwin system used by Schuhmacher et al. exhibits the LF breakdown discussed in Chapter 6.

## Computation times

The model of a pressure sensor also used by Benz et al. [Ben+19] is considered to exemplify the increased performance of the MS approach of Subsection 8.3.3. There are 37 terminals defined on its conductors, leading to an inductance matrix  $\mathbf{L}_{\text{ext}}$  of dimension  $26 \times 26$ . The model is meshed with 250,000 tetrahedra, and 39,000 face sensitivities  $d\mathbf{L}_{\text{ext}}/dp_i$  are computed on a 2.8 GHz Intel Xeon CPU. In a compromise between performance and stability,

Table 8.1.: [Sty+22] Computation times for 39, 000 face sensitivities  $dL_{\text{ext}}/dp_i$  of a pressure sensor model meshed with meshed with 250, 000 tetrahedra.

	original approach	new approach
operator assembly	4.79 h (38 %)	1.17 h (61 %)
matrix vector products	7.2 h (57 %)	0.75 h (39 %)
post-processing	0.6 h (5 %)	-
total time	12.6 h	2.34 h

$n = 3$  frequency points are considered for the least-squares fit required by Schuhmacher et al.'s original method. The computation times listed in Table 8.1 indicate that the MS-based approach is 6.5 times faster than the original approach.

### Treatment of g-field derivatives

In the derivation of the inductive sensitivities  $dL_{\text{ext}}/dp_i$  of (8.38), not only the geometric derivatives of the fields  $\vartheta$  and  $\mathbf{E}_V$  are treated with the adjoint method but also the derivatives  $dg/dp_i$  of the auxiliary field  $g$ , which appears on the right-hand sides of (5.28a) and (5.29a). Schuhmacher et al. [Sch+18a] did not apply the adjoint method to the  $g$  derivatives but rather listed the linear system to be solved in order to compute  $dg/dp_i$  directly. A direct computation of  $dg/dp_i$ , however, becomes prohibitively expensive for larger models with a high number of geometric parameters  $p_i$ . The authors note that the  $dg/dp_i$  terms are significant only for sensitivities associated with mesh nodes or faces near the terminals, and thus can be neglected if necessary. However, treating the terms in the approach of Subsection 8.3.3 with the adjoint method allows to consider them also for large models without significant penalty. Fig. 8.3 shows the influence of these terms for inductive sensitivities  $dL_{\text{ext}}/dp_i$  of a wire with square cross section with respect to Cartesian shifts  $p_i$  of the mesh nodes on the wire's surface. Especially if the sensitivities are to be used in a gradient-based shape optimization, a correct computation of the gradients in all areas is paramount.

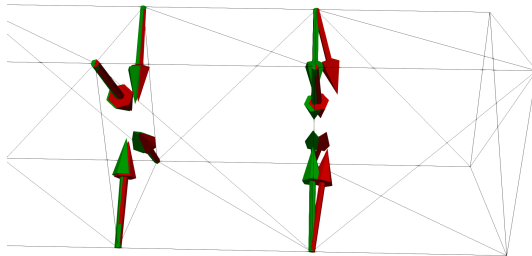


Figure 8.3.: [Sty+22] Inductive sensitivities  $dL_{ext}/dp_i$  of a wire with square cross section with respect to Cartesian shifts  $p_i$  of the wire's surface nodes, both excluding terms with derivatives  $dg/dp_i$  of the auxiliary field  $g$  (red) and including these terms via the adjoint method (green). Near the end of the wire (i.e., a terminal surface) the former result features a spurious longitudinal component, which should be avoided especially if the result is to be used for an automated shape optimization.



---

## 9. Industrial Application: Common Mode Choke

---

The models used to produce numerical results during the development of the parasitic extraction method in Chapter 5, the LF stabilization in Chapter 6, and the vector fitting approach of Chapter 7 are largely academic in nature. Therefore, this chapter applies the techniques of Chapters 5, 6, and 7 to a common-mode choke (CMC), which is a device type directly relevant in EMC engineering. A comparison of simulation and measurement results in the following section provides a further verification of the developed parasitic extraction method. The ability of the method to effortlessly include inhomogeneous, dispersive, and complex-valued material parameters is showcased due to the magnetic core contained in the CMC. In addition, the application of the vector fitting method to simulation results in Section 9.2 showcases the superior stability of the combined MQS and ES approach developed in Section 7.2. The discussion of this Chapter is contained in a highly condensed form in [SKD22b].

### 9.1. Verification with Measurement Results

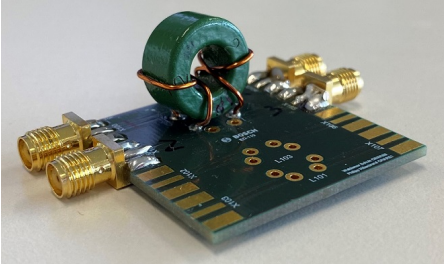
The considered CMC is displayed in Fig. 9.1. It consists of two wires around a magnetic core that are connected to a printed circuit board (PCB). Four SMA connectors are soldered to the PCB, whose barrels are connected to the PCB's ground plane. Terminals are assigned to the pins of the connectors as depicted in Fig. 9.1b. The terminals  $T_1$  and  $T_2$  are thereby galvanically connected, and the same holds true for the pair  $T_3$  and  $T_4$ .

The function of a CMC is to attenuate the common-mode (CM) current  $I_{\text{CM}}$  passing through the choke while being much more permissive for the differential-mode (DM) current  $I_{\text{DM}}$ . If  $I_1$  describes the current flowing through the left wire of the CMC from  $T_1$  to  $T_2$  and  $I_2$  the current through the right wire from  $T_3$  to  $T_4$ , the CM and DM currents are simply [BE95]

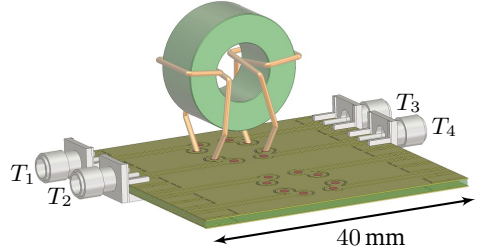
$$I_{\text{CM}} = I_1 + I_2, \quad (9.1)$$

$$I_{\text{DM}} = \frac{1}{2} (I_1 - I_2). \quad (9.2)$$

Important characteristics of a CMC are its CM impedance  $Z_{\text{CM}}$  and DM impedance  $Z_{\text{DM}}$ ,



(a) Photography.



(b) CAD model.

Figure 9.1.: [SKD22b] Common mode choke consisting of two wires wound around a magnetic core on a PCB. (© 2022 IEEE)

which are defined as the ratios of the mixed-mode voltages

$$V_{\text{CM}} = \frac{1}{2} (V_1 + V_2), \quad (9.3)$$

$$V_{\text{DM}} = V_1 - V_2. \quad (9.4)$$

with their respective mixed-mode currents  $I_{\text{CM}}$  and  $I_{\text{DM}}$ . The mixed-mode impedances  $Z_{\text{CM}}$  can be  $Z_{\text{DM}}$  computed from the  $2 \times 2$  branch impedance matrix  $\mathbf{Z}$  of the conductive topology  $\mathcal{T}_{\text{c}} = \{(T_1, T_2), (T_3, T_4)\}$  by assuming a pure CM current, i.e.,  $I_1 = I_2$ , for the computation of  $Z_{\text{CM}}$  and a pure DM current, i.e.,  $I_1 = -I_2$ , for the computation of  $Z_{\text{DM}}$ . Relating the currents and voltages with

$$\begin{pmatrix} V_1 \\ V_2 \end{pmatrix} = \mathbf{Z} \begin{pmatrix} I_1 \\ I_2 \end{pmatrix} \quad (9.5)$$

the mixed-mode impedances can be derived as

$$Z_{\text{CM}} := \frac{U_{\text{CM}}}{I_{\text{CM}}} = \frac{1}{4} ([\mathbf{Z}]_{11} + [\mathbf{Z}]_{12} + [\mathbf{Z}]_{21} + [\mathbf{Z}]_{22}), \quad (9.6)$$

$$Z_{\text{DM}} := \frac{U_{\text{DM}}}{I_{\text{DM}}} = [\mathbf{Z}]_{11} + [\mathbf{Z}]_{22} - [\mathbf{Z}]_{12} - [\mathbf{Z}]_{21}. \quad (9.7)$$

All measurements were performed by Martin Boettcher and Dr. Andreas Klaedtke with a vector network analyzer (VNA) that measures the scattering matrix  $\mathbf{S}$  in a frequency sweep, with the characteristic impedance  $Z_0 = 50 \Omega$  applied at all ports. The inductance matrix can be recovered from  $\mathbf{S}$  with [Rus06, Section 10.2]

$$\mathbf{Z} = Z_0 (\mathbf{I} - \mathbf{S})^{-1} (\mathbf{I} + \mathbf{S}). \quad (9.8)$$

Here,  $\mathbf{I}$  is the identity matrix (of the same dimensions as  $\mathbf{S}$ ). As the barrels of the four SMA connectors, which constitute one of the terminals of each port, are all connected to the ground layer, the VNA measurement determines  $\mathbf{S}$  in a star topology (cf. Fig. 5.1) in which the reference terminal  $T_0$  is the ground plane. The impedance computed from the measured  $\mathbf{S}$  of the CMC with (9.8) is therefore a nodal impedance matrix  $\mathbf{Z}_N$  with respect to the reference  $T_0$ . The branch impedance matrix  $\mathbf{Z}$  of the conductive topology  $\mathcal{T}_c$  needed for the computation of  $Z_{CM}$  and  $Z_{DM}$  can be calculated from  $\mathbf{Z}_N$  with (4.48).

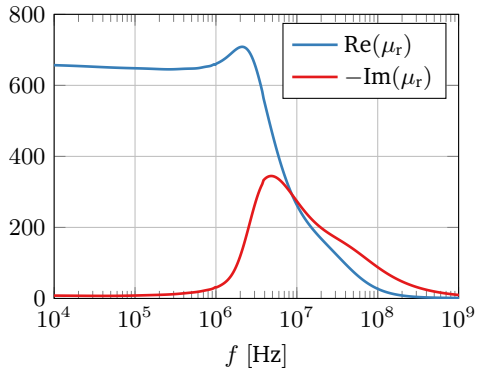
To facilitate a FEM simulation of the CMC model of Fig. 9.1b, the relative permeability  $\mu_r$  of the magnetic core must be known in the considered frequency interval. To this end a measurement is carried out according to the method of [GB87]. A one-port scattering parameter  $S$  is measured both with a single winding around the magnetic core as depicted in Fig. 9.2a, and with the same winding without the core. Converting the scattering parameters into impedances with (9.8), the relative permittivity of the core material is given as

$$\mu_r(f) = 1 + \frac{Z_s(f) - Z_e(f)}{j f \mu_0 h \ln\left(\frac{b}{a}\right)}. \quad (9.9)$$

Here,  $Z_s$  is the impedance measured with the sample in the winding,  $Z_e$  is the impedance of the empty winding,  $h = 8$  mm is the height of the toroid core, and  $a = 4$  mm and  $b = 8$  mm are its inner and outer radii, respectively. The measurement result is displayed in Fig. 9.2b. A noise reduction algorithm has been applied to smoothen the LF values. Below  $f = 10$  kHz the signal-to-noise ratio of the VNA is too low to obtain reliable results. However, as  $\mu_r$  is



(a)



(b)

Figure 9.2.: (a) Setup for permeability measurement of the magnetic core.  
(b) Measured relative permeability  $\mu_r$  after noise reduction.

virtually static in the low frequency regime, its value at 10 kHz can also be used to compute the impedance matrix of the CMC at frequencies  $f < 10$  kHz.

Fig. 9.3 compares measurement and simulation results of the modulus of the CM impedance  $Z_{CM}$  and the DM impedance  $Z_{DM}$ . Both full-wave simulation results and values obtained by combining MQS and ES results with (4.50) are shown. The full-wave numerical results agree closely with the measurement results for frequencies  $f > 200$  kHz. At lower frequencies the VNA measurement becomes unstable. In contrast to the simulation results, the measurement results are therefore unsuitable to create an equivalent circuit of parasitics that stays valid below  $f = 200$  kHz. The combined MQS and ES numerical results deviate from the full-wave values only slightly at very high frequencies  $f > 200$  MHz. In this HF regime the CM impedance is no longer larger than the DM impedance, indicating that it is beyond the relevant operating frequency interval of the CMC.

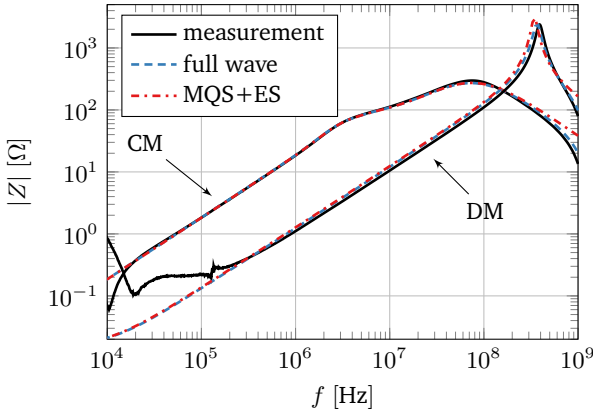


Figure 9.3.: [SKD22b] Modulus of the CM and DM impedance obtained from a VNA measurement, from a full-wave simulation and by combining MQS and ES simulation results. Below  $f = 200$  kHz the VNA measurement is unstable. At all higher frequencies, full-wave numerical results and measurement results agree closely. Combined MQS and ES results deviate from the full-wave values only slightly at frequencies  $f > 200$  MHz. (© 2022 IEEE)

---

## 9.2. Vector Fitting Results

Utilizing the extracted parasitic impedances in transient network simulations with the strategy described in Chapter 7 requires the calculation of a PRF approximating the nodal admittance matrix  $\mathbf{Y}_N$ . The numerical results presented in Section 7.3 already demonstrate that the straightforward approach of obtaining  $\mathbf{Y}_N$  as the inverse of a full-wave impedance matrix  $\mathbf{Z}_N$  can be problematic in the LF regime due to the high condition number of the matrix rendering the inversion unstable. The condition number of the CMC model's nodal impedance matrix  $\mathbf{Z}_N$  stays below  $10^{13}$  for  $f < 1$  Hz and is therefore lower than that of the capacitor-coil model displayed in Fig. 7.2; the instability of the CMC's  $\mathbf{Y}_N$  is hence much less pronounced than the one shown in Fig. 7.3. Nevertheless, the consequences of this instability are more consequential for the CMC model: In contrast to the capacitor-coil model, it is not possible for the CMC model to generate an equivalent circuit with the correct LF behavior by disregarding the unstable values during vector fitting. Fig. 9.4 compares the full-wave FEM data to both a PRF fitted to all data points and a PRF fitted only to the fully stable data above  $f = 30$  Hz. As the asymptotic behavior for  $f \rightarrow 0$  is not yet reached at this cut-off frequency, the PRF considering only the stable data is unable to produce the correct behavior for  $f \rightarrow 0$ . Choosing a lower cut-off frequency does not resolve the issue.

While the deviations of the PRF values from the FEM data seem to be relatively minor in Fig. 9.4, a comparison with the original  $\mathbf{Z}_N$  data demonstrates the issue more drastically. Fig. 9.5 compares the values of two elements  $Z_{N,11} \equiv [\mathbf{Z}_N]_{11}$  and  $Z_{N,13} \equiv [\mathbf{Z}_N]_{13}$  of the nodal impedance matrix obtained with the full-wave PRF and MQS ES PRF to both the original full-wave data points and VNA measurement results in a much higher frequency interval than used in Fig. 9.4. Here, the full-wave PRF using both stable and unstable data points is displayed (the PRF obtained with only stable data shows a similar result). Whereas the values of the approach of Section 7.2 combining an MQS PRF with ES capacitances are identical at low frequencies to the original full-wave data, the full-wave PRF deviates from the data at the same frequencies at which the VNA measurement result exhibits an unstable behavior. This discrepancy is observable for frequencies as high as  $f = 1$  MHz, demonstrating that small inaccuracies in the asymptotic behavior for  $f \rightarrow 0$  can pollute the nodal impedance of the PRF also at much higher frequencies. These results further attest to the merit of the stable vector fitting approach of Section 7.2.

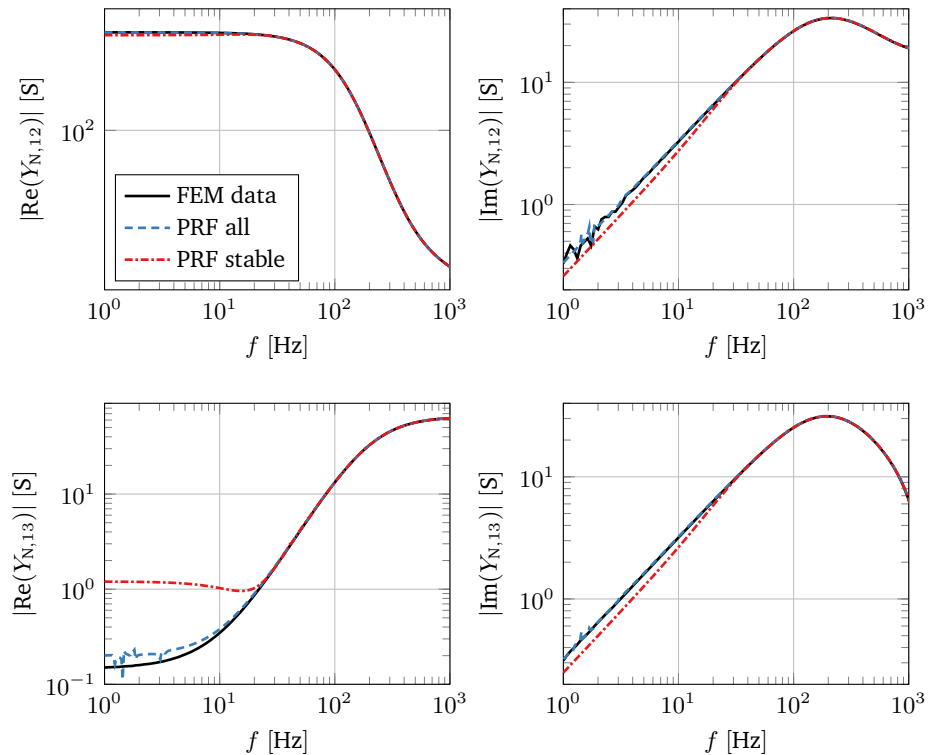


Figure 9.4.: [SKD22b] Modulus of the real and imaginary parts of two elements of nodal admittance matrix of the CMC model. The full-wave FEM data are compared to the values of both a PRF fitted to all data points and a PRF fitted only to the stable data points above  $f = 30$  Hz. Unlike for the capacitor-coil model in Fig. 7.3 the stable PRF values do not exhibit the correct asymptotic behavior for  $f \rightarrow 0$ . (© 2022 IEEE)

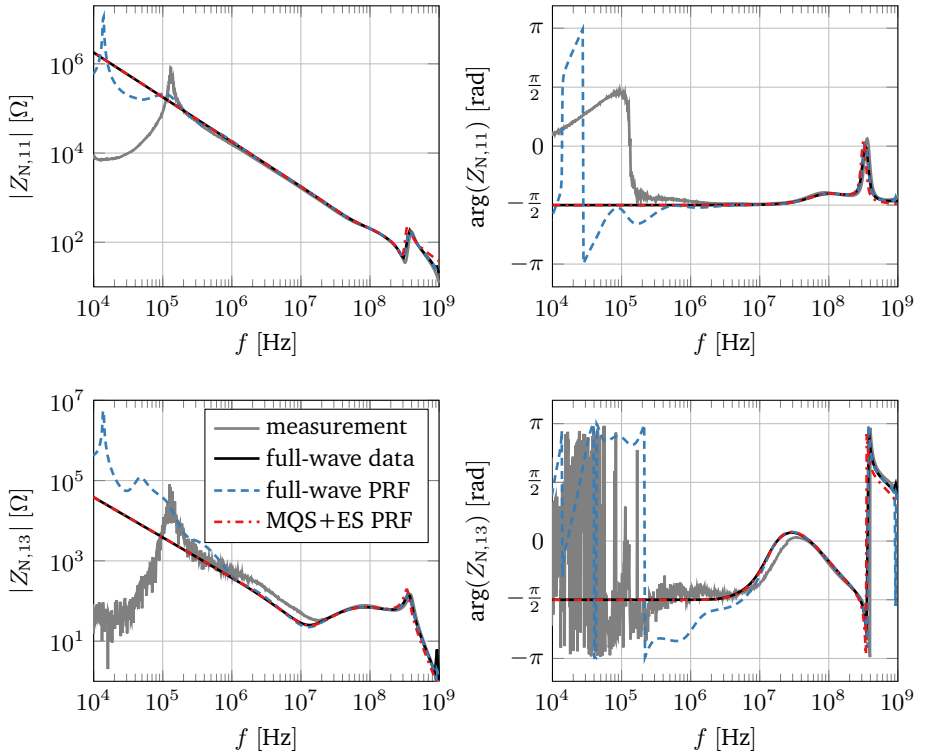


Figure 9.5.: [SKD22b] Modulus and phase of two elements of the nodal impedance matrix  $Z_N$ . Measurement and full-wave FEM data are compared to the values of the full-wave PRF and the MQS ES approach of Section 7.2. At the same low frequencies where the VNA measurement becomes unstable, the values of the full-wave PRF deviate from the full-wave data. The combined MQS ES approach yields the expected LF values. (© 2022 IEEE)



---

## 10. Conclusions

---

### 10.1. Summary

This thesis developed a broadband finite element parasitic extraction method. It is capable of the automated computation of both the complete parasitic response in the form of a nodal impedance matrix, and individual resistances, inductances, and capacitances. Additionally, a stable sensitivity analysis method was built on the basis provided by the parasitic extraction.

Chapter 4 established the connections between electric network parameters and electromagnetic field quantities, most notably by presenting a broadband impedance computation method that utilizes the electric scalar potential.

The parasitic extraction method central to this thesis was developed in Chapter 5. It generalizes the current excitation and its inductive compensation term originally proposed by Traub et al. [Tra+12], which enables the correct and automated computation of partial inductances for arbitrary device models. A general full-wave system is used to compute the complete parasitic response of a device. The magnetostatic and magnetoquasistatic approximations facilitate efficient extractions of resistances and inductances, which can be supplemented by the capacitances of an electrostatic extraction. Asymptotic and absorbing boundary conditions were used to approximate open boundaries. Additionally, the Darwin approximation was considered with perfect electric conductors, enabling the computation of eigenmodes in a generalized eigenvalue problem and the extraction of additional capacitances beyond the result of the electrostatic extraction. Comparisons of simulation results with both analytical and numerical references verified the method.

Chapter 6 derived an unconditionally low-frequency stable finite element discretization scheme for the parasitic extraction method, that is based on Eller et al.'s approach [Ell+17]. The used decomposition of the Sobolev space of curl-conforming functions facilitates an application of the method not only to the full-wave system but also to the quasistatic approximations. Numerical results verified that the discretization scheme enables a stable impedance computation from the DC point to the high-frequency regime.

Chapter 7 demonstrated how frequency-dependent parasitics can be included in transient circuit simulations by synthesizing an equivalent circuit via the vector fitting method. A stability issue that can arise if low-frequency data is provided in the form of a nodal impedance matrix was discussed. An alternative stable approach that combines magnetoquasistatic and electrostatic results was developed and verified with numerical results.

---

A sensitivity analysis method improving upon the approach of Schumacher et al. [Sch+18a] with respect to efficiency, robustness, and applicability was derived in Chapter 8. Both a numerically cheap magnetostatic computation method for inductive sensitivities, and a magnetoquasistatic method to compute resistive and inductive parasitics frequency-dependently were provided. Numerical results demonstrated the efficacy and efficiency of the methods.

Chapter 9 applied the developed parasitic extraction method to an off-the-shelf common mode choke with a magnetic core. A comparison of measurement and simulation results provided an additional verification of the method. An application of the circuit synthesis approaches of Chapter 7 to the extracted parasitics further demonstrated the merit of the low-frequency stable approach combining magnetoquasistatic and electrostatic results.

## 10.2. Outlook

An inclusion of the derived sensitivity analysis method in an automated shape optimization algorithm would be of substantial value to harness the full potential of the method.

The number of parameters in the equivalent circuits synthesized with the technique discussed in Chapter 7 scales quadratically with the number of ports in the system. Models with several dozens of ports, that are not uncommon in industrial applications, can thus have equivalent circuits with tens of thousands of elements. The computation times of transient simulations incorporating such large equivalent circuits can become unfeasibly high in some cases. Therefore, a scheme to reduce the number of parameters used while at the same time maintaining a high accuracy would be of great value.

The absorbing boundary condition derived in Section A.1 is an efficient and straightforward way to approximate an open boundary in the full-wave case, and its efficacy was verified in numerical experiments. However, in order to also provide accurate results in the low-frequency regime, it relies on a simplification that causes the approximation to be less accurate for very large radii of the boundary sphere. This behavior complicates the choice of the boundary sphere radius, and generally limits the accuracy of the approach. More research is needed to determine where an alternative boundary condition can be derived that does not require this simplification without compromising on accuracy at low frequencies.

To enable an adaptive  $hp$ -refinement of the mesh and polynomial order for the impedance computation method, an efficient and reliable error indicator is needed that can estimate how the error is distributed among the mesh cells. However, the impedance is not computed directly from the solution of a single boundary value problem. The fact that the impedance computation involves a series of three consecutive finite element solutions severely complicates the derivation of an error indicator as the error propagates through the successive systems.

The numerical resistance results presented demonstrate that the finite element method is only incapable of correctly modeling the skin effect at very high frequencies when and

---

where the mesh size is much smaller than the skin depth. One approach to avoid excessive mesh refinement needed for correctly modeling thin skin depths is to switch to a surface impedance model. This is a difficult task in the context of a fully automated broadband method.



---

## A. Appendix

---

### A.1. Asymptotic and Absorbing Boundary Conditions

As discussed in Section 5.1, simulating an electrical device in free space with the FEM requires an open boundary technique which ensures that the fields inside the finite computational domain behave as if the domain were infinite. A very powerful open boundary technique is to couple the FEM used for the fields inside the computational domain  $\Omega$  to a boundary element method (BEM) treating the free space exterior to  $\Omega$  [BTW84, Chapter 13]. While this approach has the advantages that it does not rely on approximations and is applicable at all frequencies, it is computationally very expensive: The matrices resulting from a boundary element discretization are, although small compared to FEM matrices, densely populated. Coupling FEM and BEM yields linear systems whose matrices are neither small nor sparse enough for an efficient solution with solvers optimized for sparse matrices.

Methods in which all DoFs of the boundary are coupled with each other, like the FEM-BEM coupling, are referred to as *global*. The large 3D models common in industrial applications warrant the use of a *local* method that does not have this property in order to obtain simulation results within acceptable computation times. Which local open boundary techniques are available to solve a specific electromagnetic PDE depends on whether the equation supports wave propagation, like the E-field formulation (5.2), or not, like the MQS equation (5.24a).

In the more difficult case that wave solutions have to be considered, a standard approach is to use the perfectly matched layer (PML) technique. In this approach, originally introduced in [Bér94] in the “split field” form that requires a modification of the PDEs, an absorbing layer that is able to dampen all entering waves without any significant reflections is attached to the domain’s boundary. First introduced for the finite-difference time-domain method, PML is also readily available for FEM solutions of the the E-field formulation (5.2) in a form that, instead of requiring a change of the PDEs, introduces the layer into the equations by using uniaxially anisotropic material parameters [PM95]. Still, the PML technique is not employed in this work for a number of reasons:

1. Standard forms of PML do not dampen evanescent waves [DS95]. The fact that the MQS inductance computation discussed in Chapter 5 still requires an open boundary technique to obtain accurate results even though only evanescent fields are supported by the equation demonstrates that this is an issue for parasitic extraction.

2. At low frequencies, a relatively thick PML might be required [DS95] and the technique breaks down at the DC point ( $f = 0$ ). It is, however, the objective of this work to develop a parasitic extraction technique valid for both low and high frequencies.
3. The PML form of [PM95] can only be used for the E-field formulation (5.2), the BVP (5.22) determining  $\phi_c$  requires a different treatment. Hence, the cost of implementation of a PML approach would be relatively high, especially considering that the PML must be realized by adding an actual structure to the model.

A less sophisticated approach that can avoid these issues is to use an absorbing *boundary condition* (ABC) derived by approximating the fields that would occur at the position of the finite boundary if the computational domain were infinite. Whereas the classical ABC approaches of [BGT82; Pet88] are, like the PML technique, not well suited to treat evanescent fields at the boundary [Mit+89], it is possible to combine these approaches with the related asymptotic BC [KKM90; Bra+91] (also abbreviated by ABC), which treats PDEs without wave term. Relying on approximations, this combination of absorbing and asymptotic BCs derived in the following is less accurate than a PML treatment at high frequencies; nevertheless it enables a relatively accurate impedance extraction at both low and high frequencies, without increasing the numerical cost of the extraction method. The derived ABCs already appeared in a Master's thesis [Din21] supervised by the author of this dissertation.

### A.1.1. Asymptotic boundary conditions

Both asymptotic and absorbing BCs require an approximation of the field on the boundary  $\partial\Omega$ . In free space (i.e., where  $\sigma = 0$  and  $\varepsilon_r = \mu_r = 1$ ), in regions where the source current density  $\mathbf{J}_s$  is zero, the MQS PDE (5.24a) simplifies to the (vectorial) Laplace equation

$$\Delta \mathbf{E} = 0. \tag{A.1}$$

Analogously, the Coulomb-gauged PDE (5.22a) to determine  $\phi_c$  simplifies to the scalar Laplace equation wherever its RHS vanishes in free space.

If the sources of the two PDEs are contained within a sphere of radius  $r_s$  around the coordinate origin, the fields outside the sphere can be described in spherical coordinates  $(r, \theta, \varphi)$  with the multipole expansions [Jac99]

$$\mathbf{E}(r, \theta, \varphi) = \sum_{i=0}^{\infty} \mathbf{E}_i(r, \theta, \varphi) \equiv \sum_{i=0}^{\infty} \frac{\boldsymbol{\alpha}_i(\theta, \varphi)}{r^{i+1}}, \tag{A.2a}$$

$$\phi_c(r, \theta, \varphi) = \sum_{i=0}^{\infty} \phi_{c,i}(r, \theta, \varphi) \equiv \sum_{i=0}^{\infty} \frac{\beta_i(\theta, \varphi)}{r^{i+1}}. \tag{A.2b}$$

The lowest order or *monopole* terms  $\mathbf{E}_0$  and  $\phi_{c,0}$  vanish if the volume integral over the fields' sources vanishes [Bra+91; Jac99], which is true for all PDEs considered in this work. At large distances to the sources,  $r \gg r_s$ , the dominant terms in (A.2) are the dipole terms proportional to  $r^{-2}$  (as the higher order terms decay faster with increasing  $r$ ). On the boundary, the lowest-order approximations of the fields of (5.24a) and (5.22a) are thus

$$\mathbf{E}(r, \theta, \varphi) \approx \frac{\boldsymbol{\alpha}_1(\theta, \varphi)}{r^2} \quad \text{on } \partial\Omega, \quad (\text{A.3a})$$

$$\phi_c(r, \theta, \varphi) \approx \frac{\beta_1(\theta, \varphi)}{r^2} \quad \text{on } \partial\Omega. \quad (\text{A.3b})$$

Assuming a spherical boundary  $\partial\Omega$  of radius  $r_b \gg r_s$  such that its unit normal  $\hat{\mathbf{n}}$  coincides with the radial unit vector  $\hat{\mathbf{r}}$  (this is only approximately true when not allowing for curved mesh cells), a vectorial asymptotic BC approximating the boundary term in (6.6) is derived using (A.3a) [Bra+91],

$$\hat{\mathbf{n}} \times \text{curl } \mathbf{E} = \frac{1}{r} \mathbf{E}_t, \quad (\text{A.4})$$

with  $\mathbf{E}_t$  denoting the tangential component of  $\mathbf{E}$ ,

$$\mathbf{E}_t := \mathbf{E} - \hat{\mathbf{n}}(\hat{\mathbf{n}} \cdot \mathbf{E}) = -\hat{\mathbf{n}} \times (\hat{\mathbf{n}} \times \mathbf{E}). \quad (\text{A.5})$$

An analogous scalar ABC for (5.22a) can be found by following [KKM90] but assuming a vanishing monopole term. This yields [Din21]

$$\hat{\mathbf{n}} \cdot \text{grad } \phi_c = -\frac{2}{r} \phi_c. \quad (\text{A.6})$$

To better fulfill the ABC requirement that the fields' sources should be localized in a sphere of minimal radius  $r_s$ , a homogeneous Dirichlet boundary condition is chosen for the field  $g$  in (5.20), as  $g$  appears on the RHS of (5.22a).

### A.1.2. Absorbing boundary conditions

The E-field form (5.2) and Lorenz-gauged equation (5.23) contain wave terms and simplify to the Helmholtz equation in free space, i.e, for  $\mathbf{E}$ ,

$$\Delta \mathbf{E} + k^2 \mathbf{E} = 0. \quad (\text{A.7})$$

For a field subject to the Helmholtz equation the analogon to the multipole expansion (A.2) is the Wilcox expansion theorem [Wil56]

$$\mathbf{E}(r, \theta, \varphi) = e^{j\omega k} \sum_{i=0}^{\infty} \frac{\boldsymbol{\alpha}_i(\theta, \varphi)}{r^{i+1}}, \quad (\text{A.8a})$$

$$\phi_c(r, \theta, \varphi) = e^{j\omega k} \sum_{i=0}^{\infty} \frac{\beta_i(\theta, \varphi)}{r^{i+1}}. \quad (\text{A.8b})$$

Here,  $k := \omega/c$  denotes the vacuum wave number (as in Chapter 6).

For the Laplace equation (A.1), the fact that the monopole term vanishes in the multipole expansion (A.2) if the integral over the sources vanishes can be shown by expressing  $\mathbf{E}$  in the source-free region  $r > r_s$  with Green's function, and employing a Taylor expansion around  $r = 0$  [Bra+91]. Following the same procedure using the Green's function of the Helmholtz equation (A.7) shows that the lowest order terms of (A.8) do not fully vanish in this situation. They do, however, vanish approximately at low frequencies. While the absorbing BCs of [BGT82; Pet88] do not require a vanishing lowest-order term of the expansion (A.8), they are not designed to treat evanescent fields that have not decayed at the position of the boundary [Mit+89]. More precisely, in the limit  $k \rightarrow 0$ , where the Helmholtz equation (A.7) becomes the Laplace equation (A.1), these absorbing BCs do not coincide with the asymptotic BCs of (A.4) and (A.6).

By disregarding the not fully vanishing lowest-order terms, approximate absorbing BCs can be derived that become asymptotic BCs in the static limit. Thus, only the  $1/r^2$  terms are considered on the boundary,

$$\mathbf{E}(r, \theta, \varphi) \approx e^{j\omega k} \frac{\alpha_1(\theta, \varphi)}{r^2} \quad \text{on } \partial\Omega, \quad (\text{A.9a})$$

$$\phi_c(r, \theta, \varphi) \approx e^{j\omega k} \frac{\beta_1(\theta, \varphi)}{r^2} \quad \text{on } \partial\Omega. \quad (\text{A.9b})$$

Employing this approximation, absorbing BCs are derived analogously to the asymptotic BCs of the previous subsection [Din21]. This results in the vectorial absorbing BC

$$\hat{\mathbf{n}} \times \text{curl } \mathbf{E} = \left( jk + \frac{1}{r} \right) \mathbf{E}_t \quad (\text{A.10})$$

and the scalar absorbing BC

$$\hat{\mathbf{n}} \cdot \text{grad } \phi = - \left( jk + \frac{2}{r} \right) \phi. \quad (\text{A.11})$$

The numerical results of Fig. 5.6 and Fig. 5.9 demonstrate that the ABC of (A.10) does not only perform well in the LF regime but also provides sufficiently accurate results at higher frequencies.

In [Din21] it is observed (but not explained) that the performance of the derived absorbing BCs deteriorates for increasingly large radii  $r_b$  of the boundary sphere, while being satisfactory for lower values of  $r_b$ . This behavior can be ascribed to the non-vanishing  $1/r$  term in the expansion (A.8), and indicates that the absorbing BCs (A.10) and (A.11) are useful only for intermediate values of  $r_b$ , where the expansion is still dominated by the  $1/r^2$  terms. More research is needed to determine whether a different absorbing BC can be found that behaves correctly in both limits  $k \rightarrow 0$  and  $r \rightarrow \infty$ .

---

## A.2. Computation of Non-Static Capacitances

It is often desirable for EMC engineers to describe the parasitic effects of a DUT with only a small set of interpretable, frequency-independent resistances, inductances, and capacitances. As discussed in Chapter 4, such an  $f$ -independent approach is only strictly valid in a quasistatic setting, when neglecting the skin effect, and in the absence of dispersive materials. Still, it remains an important question how to extract an optimal set of  $f$ -independent parasitics if the application at hand allows for such a description. The MS approach of Subsection 5.3.1 and ES approach of Subsection 4.1.3 yield sets of interpretable,  $f$ -independent inductances and capacitances, respectively. The ES capacitances, however, only describe interactions between different conductors and cannot model the resonant behavior that is observed for, e.g., a single wire segment.

In [HP15] an approach to compute additional *non-static* capacitances was proposed, that are able to model the capacitive behavior observed on a single conductor. This approach enhances the eigenmode-based extraction method of [Tra+13b; Tra+13a] such that a capacitance computation is also possible if only a small number of eigenmodes is accessible in the quasistatic regime. Nevertheless, the approach is only able to produce non-static capacitances that improve the parasitic network for relatively simple applications. In other cases, adding these non-static capacitances to a network that contains MS inductances and ES capacitances reduces the accuracy of the description of parasitic effects. This is because there is no guarantee that the finite subset of eigenmodes used in the computation captures the capacitive behavior adequately well. An additional drawback of the method is that it requires a relatively expensive eigenmode computation.

A comparatively simple modification to the approach of [HP15] resolves these issues. It utilizes the nodal capacitance matrix  $\mathbf{C}_N$  of (5.32) that is computed as a byproduct in the least-squares fit of the inductance computation method described in Subsection 5.3.2. In contrast to the ES nodal capacitance matrix of Section 4.1.3, denoted  $\mathbf{C}_N^s$  in the following, the capacitance matrix  $\mathbf{C}_N$  obtained in the Darwin approximation (using PECs) also contains the contributions of the non-static capacitances. A complete set of both ES and non-static capacitances can be obtained directly from  $\mathbf{C}_N$  with (4.52).

However, this approach can also yield negative capacitances for some larger models, which are sometimes undesired. To obtain a set of non-static capacitances  $C \geq 0$  supplementing the ES capacitances, the non-linear least squares fit described in [HP15] can be utilized in the following scheme:

1. Calculate a “non-static” nodal capacitance matrix  $\mathbf{C}_N^{\text{ns}} = \mathbf{C}_N - \mathbf{C}_N^s$  as the difference between the full capacitance matrix  $\mathbf{C}_N$  and the ES capacitance matrix  $\mathbf{C}_N^s$ .
2. Define a set of branches for the non-static capacitances. Both nodes of each branch must be associated with the same conductor. The default choice is to use all branches that fulfill this criterion and can be constructed with the nodes of the network.

- 
3. Determine the capacitances associated with these branches from  $\mathbf{C}_N^{\text{ns}}$  by solving the non-linear least-squares problem described in [HP15].

Fig. A.1 compares impedance results computed with the FEM to values of parasitic networks with different capacitances for the capacitor-coil model of Fig. 6.2 in a HF regime. Both full-wave FEM data computed with the ABC ( $\partial\Omega = \Gamma_a$ ) and PEC-case Darwin FEM data computed with the EBC ( $\partial\Omega = \Gamma_{el}$ ) are displayed. The values of a network containing only parasitic inductances and ES capacitances are compared to the values of networks that contain also non-static capacitances. One network uses non-static capacitances extracted with the original approach of [HP15]. Six eigenmodes are used for the extraction. Decreasing or increasing the number of eigenmodes used does not improve the quality of the result. The second network with non-static capacitances uses the novel computation method introduced in this section (the version that supplements the ES capacitances with a set of non-static capacitances  $C \geq 0$ ).

The values of the network obtained with the new method are clearly much closer to the FEM data than the values of the network without non-static capacitances, especially with regards to the position of the first resonance. In contrast, the original method of [HP15] yields a circuit whose first resonance is at a much lower frequency than in the FEM results.

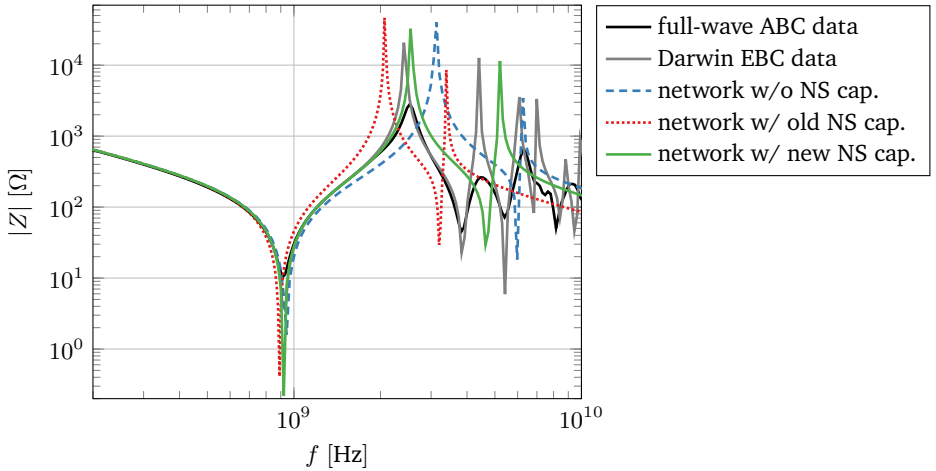


Figure A.1.: Modulus of the impedance between terminals  $T_1$  and  $T_4$  of the capacitor-coil model of Fig. 6.2. Both full-wave FEM data and Darwin FEM data are compared to the values of three different networks of extracted parasitic elements, one containing only inductances and ES capacitances, one containing in addition non-static capacitances (NS cap.) extracted with the original method of [HP15], and one containing non-static capacitances computed with the newly proposed method instead. The new approach yields a result that is closer to the FEM data than the network without non-static capacitances. The non-static capacitances of [HP15] do not unambiguously improve upon the network.



---

## Bibliography

---

- [AR88] Raffaele Albanese and Guglielmo Rubinacci. “Integral formulation for 3D eddy-current computation using edge elements”. In: *IEEE Proceedings A (Physical Science, Measurement and Instrumentation, Management and Education, Reviews)* 135.7 (1988). Number: 7, pp. 457–462. DOI: 10.1049/ip-a-1.1988.0072.
- [AS09] Charles K. Alexander and Matthew N. O. Sadiku. *Fundamentals of electric circuits*. 4th ed. Boston: McGraw-Hill, 2009. 1 p. ISBN: 978-0-07-352955-4.
- [Bat14] Klaus-Jürgen Bathe. *Finite element procedures*. 2nd ed. Englewood Cliffs, N.J: Prentice-Hall, 2014. 1043 pp. ISBN: 978-0-9790049-5-7.
- [BC11] Ashok D. Belegundu and Tirupathi R. Chandrupatla. *Optimization Concepts and Applications in Engineering*. 2nd ed. Cambridge University Press, Mar. 28, 2011. ISBN: 978-0-521-87846-3. DOI: 10.1017/CB09780511975905.
- [BE95] David E. Bockelman and William R. Eisenstadt. “Combined differential and common-mode scattering parameters: theory and simulation”. In: *IEEE Transactions on Microwave Theory and Techniques* 43.7 (July 1995). Number: 7, pp. 1530–1539. DOI: 10.1109/22.392911.
- [Ben+19] Jan Benz et al. “Analysis of Immunity Failures and Optimization Measures in Automotive Sensors”. In: *2019 International Symposium on Electromagnetic Compatibility-EMC EUROPE*. EMC Europe. IEEE, 2019, pp. 1014–1019. DOI: 10.1109/EMCEurope.2019.8871989.
- [Bér94] Jean-Pierre Bérenger. “A perfectly matched layer for the absorption of electromagnetic waves”. In: *Journal of Computational Physics* 114.2 (Oct. 1994). Number: 2, pp. 185–200. DOI: 10.1006/jcph.1994.1159.
- [BGT82] Alvin Bayliss, Max Gunzburger, and Eli Turkel. “Boundary Conditions for the Numerical Solution of Elliptic Equations in Exterior Regions”. In: *SIAM Journal on Applied Mathematics* 42.2 (Apr. 1982). Number: 2, pp. 430–451. DOI: 10.1137/0142032.
- [BHF20] Jan Benz, Jan Hansen, and Stephan Frei. “Eigenmode Based Optimization of Sensors”. In: *IEEE*, Sept. 23, 2020, pp. 1–6. ISBN: 978-1-72815-579-1. DOI: 10.1109/EMCEUROPE48519.2020.9245652.

- 
- [Bos88] Alain Bossavit. "Whitney forms: a class of finite elements for three-dimensional computations in electromagnetism". In: *IEEE Proceedings A Physical Science, Measurement and Instrumentation, Management and Education, Reviews* 135.8 (1988). Number: 8, pp. 493. DOI: 10.1049/ip-a-1.1988.0077.
- [Bos98] Alain Bossavit. *Computational electromagnetism: variational formulations, complementarity, edge elements*. Electromagnetism. San Diego: Academic Press, 1998. 352 pp. ISBN: 978-0-12-118710-1.
- [Bra+91] John R. Brauer et al. "Asymptotic boundary condition for three dimensional magnetostatic finite elements". In: *IEEE Transactions on Magnetics* 27.6 (Nov. 1991). Number: 6, pp. 5013–5015. DOI: 10.1109/20.278724.
- [BS08] Susanne C. Brenner and L. Ridgway Scott. *The Mathematical Theory of Finite Element Methods*. Red. by J. E. Marsden, L. Sirovich, and S. S. Antman. Vol. 15. Texts in Applied Mathematics. Series Editors: :n442. New York, NY: Springer New York, 2008. ISBN: 978-0-387-75934-0. DOI: 10.1007/978-0-387-75934-0.
- [BTW84] Carlos A. Brebbia, Jose C. F. Telles, and Luiz C. Wrobel. *Boundary Element Techniques*. Berlin, Heidelberg: Springer Berlin Heidelberg, 1984. ISBN: 978-3-642-48862-7.
- [CF89] S. Cristina and M. Feliziani. "A finite element technique for multiconductor cable parameters calculation". In: *IEEE Transactions on Magnetics* 25.4 (July 1989). Number: 4, pp. 2986–2988. DOI: 10.1109/20.34346.
- [Cia78] Philippe G. Ciarlet. *The Finite Element Method for Elliptic Problems*. Studies in Mathematics and its Applications v. 4. Amsterdam ; New York : New York: North-Holland Pub. Co., 1978. 530 pp. ISBN: 978-0-444-85028-7.
- [CST21] *CST Studio Suite*. Version 2021.05. 2021. URL: <https://www.3ds.com/products-services/simulia/products/cst-studio-suite/> (visited on 11/19/2021).
- [DB96] Romanus Dyczij-Edlinger and Oszkár Bíró. "A joint vector and scalar potential formulation for driven high frequency problems using hybrid edge and nodal finite elements". In: *IEEE Transactions on Microwave Theory and Techniques* 44.1 (Jan. 1996). Number: 1, pp. 15–23. DOI: 10.1109/22.481380.
- [Deo74] Narsingh Deo. *Graph Theory with Applications to Engineering and Computer Science*. Englewood Cliffs, N.J: Prentice-Hall, 1974. 478 pp. ISBN: 978-0-13-363473-0.

- 
- [Des+08] Dirk Deschrijver et al. “Macromodeling of Multiport Systems Using a Fast Implementation of the Vector Fitting Method”. In: *IEEE Microwave and Wireless Components Letters* 18.6 (June 2008). Number: 6, pp. 383–385. DOI: 10.1109/LMWC.2008.922585.
- [Din21] Nga Thuy Dinh. “Open Boundary Conditions in Electromagnetic Field Simulations for Impedance Computation”. Master’s Thesis. Ruhr Universtiy Bochum, 2021.
- [DR92] Pierre Degond and Pierre-Arnaud Raviart. “An analysis of the Darwin model of approximation to Maxwell’s equations”. In: *Forum Mathematicum* 4.4 (1992). Number: 4. DOI: 10.1515/form.1992.4.13.
- [DS95] Jan De Moerloose and Maria A. Stuchly. “Behavior of Berenger’s ABC for evanescent waves”. In: *IEEE Microwave and Guided Wave Letters* 5.10 (Oct. 1995). Number: 10, pp. 344–346. DOI: 10.1109/75.465042.
- [Ell+17] Martin Eller et al. “A Symmetric Low-Frequency Stable Broadband Maxwell Formulation for Industrial Applications”. In: *SIAM Journal on Scientific Computing* 39.4 (2017). Number: 4, B703–B731. DOI: 10.1137/16M1077817.
- [Ell17] Martin Eller. “A Low-Frequency Stable Maxwell Formulation in Frequency Domain and Industrial Applications”. dissertation. Darmstadt: TU Darmstadt, 2017. URL: <http://tubiblio.ulb.tu-darmstadt.de/92810/>.
- [FLS11] Richard P. Feynman, Robert B. Leighton, and Matthew L. Sands. *The Feynman Lectures on Physics Volume II: Mainly Electromagnetism and Matter*. New millennium edition. OCLC: 838503554. New York: Basic Books, 2011. 1 p. ISBN: 978-0-465-07998-8.
- [GB87] Ronald B. Goldfarb and Howard E. Bussey. “Method for measuring complex permeability at radio frequencies”. In: *Review of Scientific Instruments* 58.4 (Apr. 1987). Number: 4, pp. 624–627. DOI: 10.1063/1.1139227.
- [GD13] Bjørn Gustavsen and H. M. Jeewantha De Silva. “Inclusion of Rational Models in an Electromagnetic Transients Program: Y-Parameters, Z-Parameters, S-Parameters, Transfer Functions”. In: *IEEE Transactions on Power Delivery* 28.2 (Apr. 2013). Number: 2, pp. 1164–1174. DOI: 10.1109/TPWRD.2013.2247067.
- [GS01] Bjørn Gustavsen and Adam Semlyen. “Enforcing passivity for admittance matrices approximated by rational functions”. In: *IEEE Transactions on Power Systems* 16.1 (2001). Number: 1, pp. 97–104. DOI: 10.1109/59.910786.
- [GS99] Bjørn Gustavsen and Adam Semlyen. “Rational approximation of frequency domain responses by vector fitting”. In: *IEEE Transactions on Power Delivery* 14.3 (1999). Number: 3, pp. 1052–1061. DOI: 10.1109/61.772353.

- 
- [Gus02] Bjørn Gustavsen. “Computer code for rational approximation of frequency dependent admittance matrices”. In: *IEEE Transactions on Power Delivery* 17.4 (Oct. 2002). Number: 4, pp. 1093–1098. DOI: 10.1109/TPWRD.2002.803829.
- [Gus06] Bjørn Gustavsen. “Improving the Pole Relocating Properties of Vector Fitting”. In: *IEEE Transactions on Power Delivery* 21.3 (July 2006). Number: 3, pp. 1587–1592. DOI: 10.1109/TPWRD.2005.860281.
- [HKO08] Ralf Hiptmair, Florian Kramer, and Jörg Ostrowski. “A Robust Maxwell Formulation for All Frequencies”. In: *IEEE Transactions on Magnetics* 44.6 (June 2008). Number: 6, pp. 682–685. DOI: 10.1109/TMAG.2007.915991.
- [HP15] Jan Hansen and Carsten Potratz. “Capacity extraction in physical equivalent networks”. In: *IEEE*, Aug. 2015, pp. 491–496. ISBN: 978-1-4799-6616-5. DOI: 10.1109/ISEMC.2015.7256211.
- [HSS03] Christian Harlander, Rainer Sabelka, and Siegfried Selberherr. “Efficient inductance calculation in interconnect structures by applying the Monte Carlo method”. In: *Microelectronics Journal* 34.9 (Sept. 2003). Number: 9, pp. 815–821. DOI: 10.1016/S0026-2692(03)00147-2.
- [Ing06] Pär Ingelström. “A new set of H(curl)-conforming hierarchical basis functions for tetrahedral meshes”. In: *IEEE Transactions on Microwave Theory and Techniques* 54.1 (Jan. 2006). Number: 1, pp. 106–114. DOI: 10.1109/TMTT.2005.860295.
- [Jac99] John David Jackson. *Classical electrodynamics*. 3rd ed. New York: Wiley, 1999. 808 pp. ISBN: 978-0-471-30932-1.
- [JB68] Edward C. Jordan and Keith G. Balmain. *Electromagnetic waves and radiating systems*. 2. ed. Prentice-Hall electrical engineering series. OCLC: 439397. Englewood Cliffs, NJ: Prentice-Hall, 1968. 753 pp. ISBN: 978-0-13-249995-8.
- [JFD15] Martin Jochum, Ortwin Farle, and Romanus Dyczij-Edlinger. “A New Low-Frequency Stable Potential Formulation for the Finite-Element Simulation of Electromagnetic Fields”. In: *IEEE Transactions on Magnetics* 51.3 (Mar. 2015). Number: 3, pp. 1–4. DOI: 10.1109/TMAG.2014.2360080.
- [Joc+16] Martin Jochum et al. “Low-frequency stable model-order reduction of finite-element models featuring lumped ports”. In: *IEEE*, July 2016, pp. 60–65. DOI: 10.1109/MMET.2016.7544092.
- [Kam+98] Mattan Kamon et al. “Automatic generation of accurate circuit models of 3-D interconnect”. In: *IEEE Transactions on Components, Packaging, and Manufacturing Technology: Part B* 21.3 (1998). Number: 3, pp. 225–240. DOI: 10.1109/96.704933.

- 
- [KKM90] Ahmed Khebir, Ammar Kouki, and Raj Mittra. "Asymptotic boundary conditions for finite element analysis of three-dimensional transmission line discontinuities". In: *IEEE Transactions on Microwave Theory and Techniques* 38.10 (Oct. 1990). Number: 10, pp. 1427–1432. DOI: 10.1109/22.58681.
- [Kli15] Daniel Klis. "Schnelle Finite-Elemente-Verfahren für verschiedene Klassen magneto-quasistatischer Probleme". dissertation. Saarbrücken: Saarland Univ., 2015. URL: <https://doi.org/10.22028/D291-23134>.
- [Kru56] Joseph B. Kruskal. "On the shortest spanning subtree of a graph and the traveling salesman problem". In: *Proceedings of the American Mathematical Society* 7.1 (1956). Number: 1, pp. 48–50. DOI: 10.2307/2033241.
- [Lar07] Jonas Larsson. "Electromagnetics from a quasistatic perspective". In: *American Journal of Physics* 75.3 (Mar. 2007). Number: 3, pp. 230–239. DOI: 10.1119/1.2397095.
- [Max65] James Clerk Maxwell. "A dynamical theory of the electromagnetic field". In: *Philosophical Transactions of the Royal Society of London* 155 (Dec. 31, 1865), pp. 459–512. DOI: 10.1098/rstl.1865.0008.
- [Mit+89] Raj Mittra et al. "A review of absorbing boundary conditions for two and three-dimensional electromagnetic scattering problems". In: *IEEE Transactions on Magnetics* 25.4 (July 1989). Number: 4, pp. 3034–3039. DOI: 10.1109/20.34361.
- [Mon03] Peter Monk. *Finite element methods for Maxwell's equations*. Numerical mathematics and scientific computation. Oxford : New York: Clarendon Press ; Oxford University Press, 2003. 450 pp. ISBN: 978-0-19-850888-5.
- [NBB04] Natalia K. Nikolova, John W. Bandler, and Mohamed H. Bakr. "Adjoint techniques for sensitivity analysis in high-frequency structure CAD". In: *IEEE Transactions on Microwave Theory and Techniques* 52.1 (Jan. 2004). Number: 1, pp. 403–419. DOI: 10.1109/TMTT.2003.820905.
- [Néd80] Jean-Claude Nédélec. "Mixed finite elements in R<sup>3</sup>". In: *Numerische Mathematik* 35.3 (Sept. 1980). Number: 3, pp. 315–341. DOI: 10.1007/BF01396415.
- [Nis57] A. Nisbet. "Electromagnetic potentials in a heterogeneous non-conducting medium". In: *Proceedings of the Royal Society of London. Series A. Mathematical and Physical Sciences* 240.1222 (1957). Number: 1222, pp. 375–381. DOI: 10.1098/rspa.1957.0092.
- [Pet88] Andrew F. Peterson. "Absorbing boundary conditions for the vector wave equation". In: *Microwave and Optical Technology Letters* 1.2 (Apr. 1988). Number: 2, pp. 62–64. DOI: 10.1002/mop.4650010206.

- 
- [PM95] Ü. Pekel and Raj Mittra. “A finite-element-method frequency-domain application of the perfectly matched layer (PML) concept”. In: *Microwave and Optical Technology Letters* 9.3 (June 20, 1995). Number: 3, pp. 117–122. doi: 10.1002/mop.4650090303.
- [RAJ16] Albert E. Ruehli, Giulio Antonini, and Lijun Jiang. *Circuit Oriented Electromagnetic Modeling Using the PEEC Techniques*. Hoboken, New Jersey: John Wiley & Sons, 2016. 1 p. ISBN: 978-1-118-43664-6.
- [Rue+03] Albert E. Ruehli et al. “Nonorthogonal PEEC formulation for time- and frequency-domain EM and circuit modeling”. In: *IEEE Transactions on Electromagnetic Compatibility* 45.2 (May 2003). Number: 2, pp. 167–176. doi: 10.1109/TEMC.2003.810804.
- [Rue72] Albert E. Ruehli. “Inductance Calculations in a Complex Integrated Circuit Environment”. In: *IBM Journal of Research and Development* 16.5 (Sept. 1972). Number: 5, pp. 470–481. doi: 10.1147/rd.165.0470.
- [Rue74] Albert E. Ruehli. “Equivalent circuit models for three-dimensional multiconductor systems”. In: *IEEE Transactions on Microwave Theory and Techniques* 22.3 (1974). Number: 3, pp. 216–221. doi: 10.1109/TMTT.1974.1128204.
- [Rus06] Peter Russer. *Electromagnetics, microwave circuit and antenna design for communications engineering*. 2nd ed. Artech House antennas and propagation library. Boston, MA: Artech House, 2006. 729 pp. ISBN: 978-1-58053-907-4.
- [RWV94] Simon Ramo, John R. Whinnery, and Theodore Van Duzer. *Fields and waves in communication electronics*. 3rd ed. New York: Wiley, 1994. 844 pp. ISBN: 978-0-471-58551-0.
- [Sch+18a] Sebastian Schuhmacher et al. “Adjoint Technique for Sensitivity Analysis of Coupling Factors According to Geometric Variations”. In: *IEEE Transactions on Magnetics* 54.3 (Mar. 2018). Number: 3, pp. 1–4. doi: 10.1109/TMAG.2017.2774107.
- [Sch+18b] Sebastian Schuhmacher et al. “Sensitivity of Lumped Parameters to Geometry Changes in Finite Element Models”. In: *Scientific Computing in Electrical Engineering*. Vol. 28. Cham: Springer International Publishing, 2018, pp. 35–42. ISBN: 978-3-319-75537-3. doi: 10.1007/978-3-319-75538-0\_4.
- [Sch18] Sebastian Schuhmacher. “Sensitivitätsanalyse mittels adjungierter Verfahren für äquivalente Ersatzschaltbilder extrahiert aus 3D Feldmodellen”. dissertation. Darmstadt: TU Darmstadt, Mar. 2018. 137 pp. URL: <https://tubiblio.ulb.tu-darmstadt.de/103423/>.

- 
- [SD75] Adam Semlyen and A. Dabuleanu. “Fast and accurate switching transient calculations on transmission lines with ground return using recursive convolutions”. In: *IEEE Transactions on Power Apparatus and Systems* 94.2 (Mar. 1975). Number: 2, pp. 561–571. DOI: 10.1109/T-PAS.1975.31884.
- [SKD22a] Jonathan Stysch, Andreas Klaedtke, and Herbert De Gersem. “Broadband finite-element impedance computation for parasitic extraction”. In: *Electrical Engineering* 104.2 (Apr. 2022), pp. 855–867. DOI: 10.1007/s00202-021-01348-9.
- [SKD22b] Jonathan Stysch, Andreas Klaedtke, and Herbert De Gersem. “Finite Element Extraction of Frequency-Dependent Parasitics”. In: *IEEE Transactions on Magnetics* (2022). DOI: 10.1109/TMAG.2022.3161850.
- [SKD22c] Jonathan Stysch, Andreas Klaedtke, and Herbert De Gersem. “Low-Frequency Stabilization for FEM Impedance Computation”. In: *IEEE Transactions on Electromagnetic Compatibility* 64.3 (June 2022), pp. 750–759. DOI: 10.1109/TEMC.2021.3134323.
- [SS01] Rainer Sabelka and Siegfried Selberherr. “A finite element simulator for three-dimensional analysis of interconnect structures”. In: *Microelectronics Journal* 32.2 (Feb. 2001). Number: 2, pp. 163–171. DOI: 10.1016/S0026-2692(00)00113-0.
- [STH87] Y. Saito, K. Takahashi, and S. Hayano. “Finite element solution of open boundary magnetic field problems”. In: *IEEE Transactions on Magnetics* 23.5 (Sept. 1987). Number: 5, pp. 3569–3571. DOI: 10.1109/TMAG.1987.1065581.
- [Sty+22] Jonathan Stysch et al. “Efficient sensitivity analysis of lumped elements with respect to finite-element geometry changes”. In: *International Journal of Numerical Modelling: Electronic Networks, Devices and Fields* (2022). DOI: 10.1002/jnm.3012.
- [Tra+12] Felix Traub et al. “Generation of physical equivalent circuits using 3D simulations”. In: *2012 International Symposium on Electromagnetic Compatibility*. IEEE, 2012, pp. 486–491. DOI: 10.1109/ISEMC.2012.6351683.
- [Tra+13a] Felix Traub et al. “Automated construction of physical equivalent circuits for inductive components”. In: *2013 International Symposium on Electromagnetic Compatibility*. IEEE, 2013, pp. 67–72. URL: <https://ieeexplore.ieee.org/abstract/document/6653204/>.
- [Tra+13b] Felix Traub et al. “Eigenmodes of electrical components and their relation to equivalent electrical circuits”. In: *IEEE*, Aug. 2013, pp. 287–293. DOI: 10.1109/ISEMC.2013.6670425.

- 
- [Tra14] Felix Traub. “Automated Construction of Equivalent Electrical Circuit Models for Electromagnetic Components and Systems”. dissertation. Darmstadt: TU Darmstadt, Apr. 2014. 196 pp. URL: <https://tuprints.ulb.tu-darmstadt.de/3805/>.
- [Van74] Mac E. Van Valkenburg. *Network analysis*. 3rd edition. Englewood Cliffs, N.J: Prentice-Hall, 1974. 571 pp. ISBN: 978-0-13-611095-8.
- [Wil56] C. H. Wilcox. “An expansion theorem for electromagnetic fields”. In: *Communications on Pure and Applied Mathematics* 9.2 (May 1956). Number: 2, pp. 115–134. DOI: 10.1002/cpa.3160090202.
- [ZJ10] Jianfang Zhu and Dan Jiao. “A Theoretically Rigorous Full-Wave Finite-Element-Based Solution of Maxwell’s Equations From dc to High Frequencies”. In: *IEEE Transactions on Advanced Packaging* 33.4 (Nov. 2010). Number: 4, pp. 1043–1050. DOI: 10.1109/TADVP.2010.2057428.

---

## List of Acronyms and Abbreviations

---

**ABC** asymptotic boundary condition /  
absorbing boundary condition

**AC** alternating current

**BC** boundary condition

**BEM** boundary element method

**BVP** boundary value problem

**CAD** computer-aided design

**CM** common mode

**CMC** common-mode choke

**CST** CST Studio Suite

**DC** direct current

**DM** differential mode

**DUT** device under test

**DoF** degree of freedom

**EBC** electric boundary condition

**EMC** electromagnetic compatibility

**EQS** electroquasistatic

**ES** electrostatic

**ESP** electric scalar potential

**FE** finite element

**FEM** finite element method

**HF** high frequency

**LF** low frequency

**LFS** low frequency stable

**LHS** left-hand side

**MBC** magnetic boundary condition

**MQS** magnetoquasistatic

**MS** magnetostatic

**MVP** magnetic vector potential

**PDE** partial differential equation

**PEC** perfect electric conductor

**PEEC** partial element equivalent circuit

**PRF** pole-residue form

**QoI** quantity of interest

**RHS** right-hand side

**US** unstable

**VNA** vector network analyzer



---

## Acknowledgments

---

I want to thank the Robert Bosch GmbH for funding this thesis and fostering an excellent Ph.D. program, in which the candidates are allowed to pursue their research with great freedom.

On a personal level, I firstly want to express my gratitude to my doctoral advisor Herbert De Gersem and my technical supervisor at Bosch Andreas Klaedtke. They provided me with a very interesting research topic, and supported me on every step of the process with their knowledge and time. Herbert De Gersem fulfilled his role with great kindness and wisdom, and helped me considerably in navigating the difficulties of publication. Andreas Klaedtke always listened with interest to all small and large problems that I encountered, both challenged and encouraged me, and taught my numerous things in different scientific domains.

I also would like to thank Professor Clemens for kindly agreeing to provide the second review of this thesis.

In addition, I want to thank Martin Boettcher, Hermann Aichele, and Andreas Klaedtke for performing the measurements whose results are part of this thesis and several papers.

Wolfgang Ackermann and Daniel Klis deserve my gratitude for their valuable input concerning some finer points in the implementation of the finite element method. Many hours of frustration were avoided because of it.

Futhermore, I am grateful to all the colleagues at TEMF who challenged and advanced my understanding in fruitful discussions.

I want to thank Dinh Thuy Nga for her interest in the research topic I provided and for her hard work.

Finally, I want to thank Zhizhen and my family for their continuous support in all aspects of my life, and in the case of my parents and grandmother also for their financial support during my time as a student.



---

## Curriculum Vitae

---

- 2019 – 2022            Doctoral Research  
Robert Bosch GmbH in cooperation with  
Technical University of Darmstadt
- 2017 – 2019            Project Manager for Measurement Technology  
Philipp Hafner GmbH & Co. KG
- 2014 – 2017            Master of Science in Physics  
University of Stuttgart  
Thesis: *Many-particle dynamics of driven-dissipative  
Bose-Einstein condensates*  
Two exchange semesters at York University, Toronto
- 2011 – 2014            Bachelor of Science in Physics  
University of Stuttgart  
Thesis: *Korrekturoperator für Gauß-Näherungen des  
Boltzmann-Operators*
- 2002 – 2011            Abitur  
Mörrike-Gymnasium Esslingen